

Hydrogen Adsorption on Metal-Organic Frameworks

Von der Fakultät Mathematik und Physik der Universität Stuttgart
zur Erlangung der Würde eines Doktors der
Naturwissenschaften (Dr. rer. nat.) genehmigte Abhandlung

Vorgelegt von

Barbara Streppel, geb. Schmitz

aus Kirchheim unter Teck

Hauptberichterin:	Prof. Dr. G. Schütz
Mitberichter:	Prof. Dr. J. Wrachtrup
Mitberichter:	Prof. Dr. E. Roduner

Tag der mündlichen Prüfung: 16. Mai 2011

Max-Planck-Institut für Metallforschung, Stuttgart

2011

Inhaltsverzeichnis

Zusammenfassung	5
1 Introduction to hydrogen storage	15
2 Fundamentals	17
2.1 Introduction to adsorption	17
2.1.1 Adsorption	17
2.1.2 Excess, absolute, and total adsorption	18
2.1.3 Interpretation and theoretical description of adsorption isotherms	21
2.1.4 Adsorption in microporous materials	23
2.1.5 Enthalpy of adsorption	26
2.2 Metal-organic frameworks	28
2.2.1 Ultramicroporous materials	29
2.2.2 Supermicroporous materials	32
2.2.3 Mesoporous materials	38
Overview	41
3 Experimentals, Results and Discussion	43
3.1 High pressure hydrogen adsorption	43
3.1.1 Volumetric device for high pressure adsorption	43
3.1.2 Calibration	46
3.1.3 Results	50
3.1.4 Discussion	58
3.2 Low pressure hydrogen adsorption	70
3.2.1 Volumetric device for low pressure and low temperature adsorption	70
3.2.2 Calibration	71
3.2.3 Results	74
3.2.4 Discussion	88
3.3 MOFs in hydrogen storage applications	104
4 Summary	109
Addendum	113
Constants	113
Abbreviations	114
Bibliography	115

Zusammenfassung

Einleitung

Wasserstoffspeicherung

Für die Zukunft erfordert der steigende Energiebedarf der Weltbevölkerung und die sehr begrenzten Reserven fossiler Energiequellen ein Umdenken in Bezug auf die Energiegewinnung und -nutzung. Insbesondere die Speicherung der Energie, die beispielsweise aus regenerativen Energien gewonnen wurde, stellt eine große Herausforderung dar. Eine intensiv diskutierte und vielversprechende Lösung könnte Wasserstoff als Energieträger sein [1, 2]. Vor allem in mobilen Anwendungen hat Wasserstoff viele Vorteile [3, 4], da er eine sehr hohe gravimetrische Energiedichte besitzt und bei seiner Nutzung keine klimaschädlichen oder giftigen Substanzen sondern reines Wasser entsteht. Bisher wird Wasserstoff nur in wenigen Testfahrzeugen mit Brennstoffzellenantrieb genutzt. Eines der größten Probleme stellt die effiziente Speicherung des Wasserstoffs dar. Derzeit gibt es hauptsächlich zwei Speichersysteme in denen Wasserstoff in Fahrzeugen gespeichert wird, Hochdrucktanks und Cryotanks für flüssigen Wasserstoff. Hochdrucktanks werden mit bis zu 700 bar Wasserstoff beladen, wobei ihr Vorteil ist, dass die Speicherung bei Raumtemperatur stattfindet. Der Nachteil ist unter anderem, dass bei der Kompression des Gases große Mengen an Wärme frei werden, weshalb das Gas vorgekühlt werden muss. Flüssiger Wasserstoff hingegen wird bei niedrigem Druck getankt, hat aber eine Temperatur von -250°C bei einem Druck von 1 bar. Für die Verflüssigung wird ungefähr ein Drittel des Energiegehalts des Wasserstoffes benötigt. Steigt die Temperatur des Tanks, verdampft Wasserstoff. Beim Übergang aus der flüssigen Phase in die Gasphase vergrößert sich das Volumen des Wasserstoffs stark, so dass in einem geschlossenen Tank ein sehr hoher Druck entsteht. Da die Erwärmung des Tanks nicht vollständig verhindert werden kann, sind Cryotanks für flüssigen Wasserstoff offene Systeme und Wasserstoff dampft permanent in die Umgebung ab.

Aus diesen Gründen wird intensiv nach einer neuen, effizienten Methode zur Speicherung von Wasserstoff geforscht. In den letzten Jahren ist vor allem die Speicherung von Wasserstoff in Festkörpern untersucht worden. Es gibt im Wesentlichen zwei verschiedene Möglichkeiten Wasserstoff in Festkörpern zu speichern, durch chemische Bindungen die Metallhydride oder komplexe Hydride bilden und mittels physikalischer Adsorption (Physisorption) durch die schwache Van-der-Waals-Wechselwirkung von Wasserstoffmolekülen mit Oberflächen. Physisorption bietet viele Vorteile, die bei einem Tank für mobile Anwendungen gefordert werden, wie beispielsweise schnelles Be- und Entladen, kleine freiwerdende Wärmemengen beim Beladen und das Entladen kann durch

Druckänderung erfolgen. In dieser Arbeit wird Physisorption von Wasserstoff für verschiedene Materialien untersucht und die Speichereigenschaften mit den strukturellen Parametern der Materialien korreliert.

Grundlagen

Physisorption

Physisorption beruht auf Van-der-Waals-Wechselwirkungen zwischen Gasmolekülen (Adsorptiv) und Atomen der Oberfläche eines Festkörpers (Adsorbens), wobei die Adsorptionenthalpie typischerweise $1 - 10 \text{ kJ mol}^{-1}$ beträgt [5]. Größere Wasserstoffmengen werden daher hauptsächlich unter kryogenen Bedingungen adsorbiert. Selbst bei 77 K lagert sich nur eine Monolage Wasserstoff auf der Oberfläche an (Adsorbat) und es bilden sich keine sogenannten Multilagen. Bei der aufgenommenen Wasserstoffmenge muss unterschieden werden, ob es sich hierbei nur um die zusätzlich zum Gas vorhandene adsorbierte Menge handelt (excess adsorption), die Menge in der adsorbierten Lage (absolute adsorption) oder um die gesamte Menge im untersuchten Volumen (total adsorption). Bei Messungen wird meist die zusätzlich adsorbierte Wasserstoffmenge bestimmt. Diese wird entweder in die Menge in der adsorbierten Lage umgerechnet, um Modelle zur Beschreibung der Adsorption nutzen zu können, oder in die gesamte im System vorhandene Menge, um Aussagen über die technische Nutzbarkeit zu machen. Die grundlegenden theoretischen Modelle, die zur Beschreibung der Adsorption genutzt werden, sind das Henry-Modell bei sehr geringen Aufnahmen, das Langmuir-Modell [6] für reine Monolagenadsorption und das Brunauer-Emmet-Teller-Modell (BET) [7] zur Beschreibung von Multilagenadsorption bei Temperaturen unterhalb der kritischen Temperatur des Adsorptivs. Die beiden letzteren ermöglichen die Bestimmung der spezifischen Oberfläche des Adsorbens. Die Oberfläche, die für ein Gas zur Verfügung steht, hängt hierbei von der Molekülgröße des Gases ab. Mit Hilfe der Kristallstruktur kann die Oberfläche eines Materials für verschiedene Gase auch aus theoretischen Berechnungen bestimmt werden [8].

Die Bindungsenthalpie eines Gases an der Oberfläche eines Adsorbens hängt von der Oberflächentopographie und der chemischen Zusammensetzung ab, da sich die Potentiale verschiedener Oberflächenmoleküle abhängig von der Porenform und -größe überlappen können und die Van-der-Waals-Wechselwirkung durch die chemischen Elemente bestimmt wird. Die Bindungsenthalpie kann aus der Messung mehrerer Adsorptionsisothermen bei verschiedenen Temperaturen mit Hilfe der erweiterten Clausius-Clapeyron-Gleichung bestimmt werden.

Bei Messungen unterhalb der kritischen Temperatur bilden sich Multilagen aus. Bei einem Druck kurz vor der Verflüssigung ist das gesamte Porenvolumen mit Adsorbat gefüllt. Aus dieser aufgenommenen Menge wird das spezifische Porenvolumen der Materialien nach der Gurvich-Regel [9] bestimmt.

Metall-organische Gerüststoffe (MOFs)

Als Adsorbentien werden in dieser Arbeit zehn verschiedene Materialien aus der neuen Klasse der metall-organischen Gerüststoffe (metal-organic frameworks = MOFs) gewählt. MOFs bestehen aus Metallkomplexen die durch organische Liganden verbunden sind. Hierdurch bilden sich hochporöse Festkörper deren Eigenschaften wie Oberfläche oder Porengröße durch die Synthese gezielt eingestellt werden können. Die untersuchten MOFs besitzen unterschiedliche chemische Zusammensetzungen, Oberflächen von bis zu $5000 \text{ m}^2 \text{ g}^{-1}$ und Poren mit Durchmessern von $3,4 \text{ \AA}$ bis 34 \AA . Die Materialien werden nach ihren Porendurchmessern in ultramikroporös (Durchmesser bis 7 \AA), supermikroporös (Durchmesser $7 - 20 \text{ \AA}$) und mesoporös (Durchmesser $20 - 500 \text{ \AA}$) unterteilt [10]. Als Vertreter der ultramikroporösen MOFs wurden Mg-Formiat und MFU-4 (Metal-organic Framework Ulm) gewählt. Mg-Formiat [11] ist aus Magnesiumkomplexen aufgebaut, die mit Sauerstoff koordiniert und durch Formiatmoleküle verbunden sind. Durch diesen sehr kurzen Liganden entstehen in Mg-Formiat Kanäle mit einem Durchmesser von $3,4 \text{ \AA}$ bis $4,6 \text{ \AA}$ (Bild 2.7). MFU-4 [12] hingegen besteht aus Zink-Chlor-Stickstoff-Komplexen, die mit Benzol(1,2-d:4,5-d')bistriazol verbunden sind (Bild 2.9). Hieraus entsteht ein kubisches Gerüst mit zwei alternierenden Poren, deren Durchmesser $3,9 \text{ \AA}$ und 12 \AA beträgt. Da das Adsorptiv immer die kleinen Poren passieren muss, um in die größeren zu gelangen, werden die Eigenschaften des Materials durch die kleine Pore bestimmt und es wird daher als ultramikroporös eingestuft.

Wird bei MFU-4 ein längerer Ligand verwendet entsteht das supermikroporöse MFU-4L (Bild 2.11) [13] dessen beide Poren einen Durchmesser von 12 \AA und $18,6 \text{ \AA}$ aufweisen. Ein ebenfalls kubischer MOF mit alternierenden Poren ist das supermikroporöse MOF-5 (Bild 2.13) [14] dessen Zinkkomplexe mit Benzoldicarbonsäure verknüpft sind und Poren mit 12 \AA und 15 \AA Durchmesser bilden. Isostrukturell sind die beiden supermikroporösen MOFs, DUT-4 und DUT-5 (Dresden University of Technology) [15], deren Aluminiumkomplexe durch Naphthalindicarbonsäure (DUT-4) und Biphenyldicarbonsäure (DUT-5) verbunden sind (Bild 2.14). Sie haben Kanäle mit einem Durchmesser von 9 \AA und 11 \AA . Das supermikroporöse Cu-BTC (benzotricarboxylat) [16, 17] hat Poren mit einem Durchmesser von 9 \AA und kleine Seitenporen mit einem Durchmesser von 5 \AA (Bild 2.16). Der supermikroporöse MOF-177 [18] weist eine extrem große Oberfläche von $4728 \text{ m}^2 \text{ g}^{-1}$ auf. MOF-177 ist aus den gleichen Zinkkomplexen wie MOF-5 aufgebaut aber durch einen dreiarmligen Liganden (Benzol-1,3,5-tribenzoat) verknüpft und besitzt daher elliptische Poren mit einer kurzen Achse von 11 \AA und einer langen Achse von 19 \AA (Bild 2.18).

Der mesoporöse MIL-101 (Materiaux de l'Institut Lavoisier) [19, 20] ist aus Chrom-Fluor-Komplexen und Benzoldicarbonsäure aufgebaut. Die Chrom-Fluor-Komplexe bilden mit der Benzoldicarbonsäure kleine hohle Tetraeder, deren Porendurchmesser 7 \AA beträgt. Aus diesen kleinen Tetraedern sind die beiden größere Poren in MIL-101 mit Durchmessern von 29 \AA und 34 \AA (Bild 2.20) aufgebaut. Um den Einfluss der Porengröße zu untersuchen wurde in die Poren von MIL-101 Komplexe aus $\text{Mo}_6\text{Br}_8\text{F}_6$ -Molekülen eingebracht [21]. Das freie Volumen in den Poren von MIL-101F (filled) ist daher geringer als bei MIL-101 und die Dichte des Materials ist höher.

Zur Charakterisierung der Materialien wurde die Adsorption von Stickstoff bei 77 K gemessen um die spezifischen Oberflächen und Porenvolumina zu bestimmen. Die Eigenschaften der untersuchten MOFs sind in Tabelle 2.1 zusammengefasst.

Experimente, Ergebnisse und Diskussion

Für die experimentelle Untersuchung der Wasserstoffadsorption wurden zwei verschiedene Anlagen genutzt. In der Hochdruckanlage wurde die Wasserstoffaufnahme bei verschiedenen Temperaturen zwischen 77 K und Raumtemperatur bis ungefähr 20 bar untersucht. In der Niederdruckanlage wurde Wasserstoffadsorption bei einem Druck bis 1 bar und Temperaturen um 20 K gemessen, die unterhalb der kritischen Temperatur von Wasserstoff (33 K) liegt.

Wasserstoffadsorption bei hohen Drücken

Volumetrische Anlage zur Messung der Hochdruckadsorption

Für die Hochdruckmessungen wurde eine kommerzielle volumetrische Anlage (PCT2000 von HyEnergy, Setaram) genutzt, die in Kombination mit einem sogenannten Microdoser speziell für die Messung kleiner Probenmassen ausgelegt ist. Zur Messung bei Temperaturen oberhalb von 87 K wurde ein Kryostat entwickelt, der die Temperatur während der Messung auf ± 1 K konstant hält [16]. Das volumetrische Messprinzip basiert auf der Expansion des Gases aus einem Reservoirvolumen in ein Probenhaltervolumen. Neue Materialien sind oft nur in geringen Mengen verfügbar. Deshalb wurde die Anlage durch kleine Volumina (Reservoir: $0,51 \text{ cm}^3$, Probenhalter: $1,27 \text{ cm}^3$) speziell auf die Messung sehr geringer Adsorptionsmengen ausgelegt. Bei Messungen unterhalb der Raumtemperatur entstehen Temperaturgradienten zwischen dem Probenhalter und der Anlage mit dem Reservoirvolumen, die sich bei Raumtemperatur befindet. Diese Temperaturgradienten werden mit Hilfe von Vergleichsmessungen eines nicht adsorbierenden Materials (Sand) mit gleichem Volumen korrigiert. Der Messfehler der aufgenommenen Menge Wasserstoff m_{ads} beträgt bei Raumtemperatur $\Delta m_{ads} = 3 \frac{\mu\text{g}}{\text{bar}} \cdot P + 3\% \cdot m_{ads}$ und bei 77 K $\Delta m_{ads} = 125 \frac{\mu\text{g}}{\text{MPa}} \cdot P + 2,5\% \cdot m_{ads}$. Daher sind schon bei Probenmassen von 100 mg und 20 bar Wasserstoffaufnahmen oberhalb von $62 \mu\text{g}$ bei Raumtemperatur und $128 \mu\text{g}$ bei 77 K messbar.

Messungen des selben Materials mit verschiedenen Probenmassen, Vergleiche mit Literaturdaten und die Ergebnisse eines in mehreren Laboren durchgeführten Vergleichstests [22] zeigen eine sehr gute Reproduzierbarkeit der Ergebnisse.

Ergebnisse

Die aufgenommene Menge Wasserstoff wird in $[wt\%] = \frac{m_{ads}}{m_S + m_{ads}}$ angegeben, wobei m_S die Probenmasse ist. Die Adsorptionsisothermen der verschiedenen Materialien sind in Bild 3.6-3.15 gezeigt. Bei 77 K zeigen die Materialien ein für Physisorption in mikroporösen Materialien charakteristisches Typ I Verhalten (IUPAC [10]), mit einem anfänglich sehr

starken fast linearen Anstieg der Wasserstoffaufnahme mit zunehmendem Druck, die dann bei höherem Druck in Sättigung übergeht. Mit steigender Temperatur wird die gesamte Isotherme flacher, bis schließlich bei Raumtemperatur ein linearer flacher Anstieg der Wasserstoffaufnahme mit dem Druck beobachtet wird und die Aufnahme bei 20 bar unterhalb von 0,2 wt% liegt. Die Form und Höhe der Isothermen unter kryogenen Bedingungen variiert stark für die verschiedenen Materialien. Die ultramirkoporösen MOFs sind bei 77 K unterhalb von 20 bar gesättigt mit Aufnahmen von 1,2 wt% für Mg-Formiat und 2,5 wt% für MFU-4. Die supermirkoporösen und mesoporösen Materialien erreichen bei einem Druck bis zu 20 bar nicht die Sättigung, zeigen aber trotzdem Aufnahmen von bis zu 6,2 wt%. Die Ergebnisse für alle Materialien sind in Tabelle 3.1 zusammengefasst. Aus den Isothermen bei verschiedenen Temperaturen werden die isosterischen Bindungsenthalpien für einen großen Bedeckungsbereich bestimmt (Bild 3.16).

Diskussion

Die Wasserstoffaufnahmen der MOFs bei 20 bar und 77 K werden zu den BET Oberflächen, die aus Stickstoffadsorptionsisothermen bei 77 K bestimmt wurden, korreliert. Die maximale Wasserstoffaufnahme steigt linear mit der Oberfläche des Materials. Diese Ergebnisse stimmen gut mit Werten aus der Literatur überein, bei denen die Wasserstoffaufnahmen von MOFs und anderen Materialklassen, wie Preußischblau-Analoga, Zeolithen und Kohlenstoffen, linear mit ihrer Oberflächen korreliert [23, 24, 25]. Dies zeigt dass die maximale Wasserstoffaufnahme der MOFs nur von ihrer spezifischen Oberfläche, nicht aber von ihrer chemischen Zusammensetzung abhängt.

Außer der maximalen Aufnahme ist die Bindungsenthalpie für Wasserstoff in den Materialien von zentraler Bedeutung. Die Metallkomplexe bieten zwar teilweise sehr starke Bindungsplätze [26], die aber meist, im Vergleich zur gesamten Wasserstoffaufnahme des MOFs, schon von sehr wenigen Wasserstoffmolekülen gesättigt sind. Daher ist die chemische Zusammensetzung für die Bindungsenthalpie nur bei sehr niedrigen Wasserstoffaufnahmen ausschlaggebend. Bei höheren Aufnahmen wird die Bindungsenthalpie durch die Porengröße und Form beeinflusst, da diese den Großteil der Adsorptionsplätze bereitstellen. Je kleiner die Pore ist, desto stärker überlappen sich die Van-der-Waals-Potentiale der Oberflächenatome. Diese Überlappung führt zu einer erhöhten Bindungsenthalpie für die Wasserstoffmoleküle. Die gemessenen isosterischen Bindungsenthalpien der verschiedenen Materialien wird mit den Porendurchmessern korreliert (Tabelle 3.2 und Bild 3.21). Die Bindungsenthalpie nimmt mit steigendem Porendurchmesser stark ab. Für die ultramirkoporösen Materialien beträgt die Bindungsenthalpie bis zu 7 kJ mol^{-1} , supermirkoporöse Materialien weisen zwischen $5,4 \text{ kJ mol}^{-1}$ und $3,5 \text{ kJ mol}^{-1}$ und das mesoporöse MIL-101 weniger als $4,2 \text{ kJ mol}^{-1}$ auf.

Aus den Stickstoffisothermen bei 77 K werden die spezifischen Porenvolumina der verschiedenen MOFs bestimmt und zu ihrer BET Oberfläche korreliert (Bild 3.23). Das Porenvolumen nimmt mit steigender Oberfläche linear zu. Die Oberfläche wird aus dem Druckbereich der Isothermen bestimmt bei dem die Oberfläche vollständig mit einer Monolage bedeckt ist [7]. Die Porenvolumina werden bei höherem Druck bestimmt bei dem die Multilagenbildung abgeschlossen ist [9]. Da die Poren der untersuchten MOFs alle im

Bereich der Größe von wenigen Stickstoffmolekülen liegen, können sich aus Platzgründen auch bei 77 K keine Stickstoffmultilagen ausbilden. Für reine Monolagenadsorption ergibt sich $0,36 \text{ cm}^3$ pro 1000 m^2 . Die experimentellen Werte für die Porenvolumina weichen nur leicht von dieser Korrelation ab, was wenigen Molekülen in der zweiten adsorbierten Lage entspricht. Dies zeigt außerdem, dass die gemessenen Oberflächen der MOFs nahezu nur aus inneren Oberflächen bestehen.

Wasserstoffadsorption bei niederen Drücken

Volumetrische Anlage zur Messung der Niederdruckadsorption

Die zweite Messmethode beruht ebenfalls auf dem volumetrischen Messprinzip, aber ermöglicht sehr genaue Messungen bis 1 bar. Die hierfür genutzte kommerzielle Anlage (Autosorb1 von Quantachrome) ist auf die Messung von Stickstoffadsorption bei seiner Verflüssigungstemperatur von 77 K ausgelegt. Um diese Messungen mit Wasserstoff durchzuführen, wurde ein Heliumdurchflusskryostat konstruiert, der Messungen bei Temperaturen um die Verflüssigungstemperatur von Wasserstoff (20 K) ermöglicht. Der Kryostat hält die Temperatur während der Messung auf $\pm 0,1 \text{ K}$ konstant. Wird die Probe gekühlt, bilden sich Temperaturgradienten zwischen der Probe und der Anlage, die das Reservoirvolumen beinhaltet. Um diese Temperaturgradienten zu kompensieren, wird für die gemessenen Temperaturen das Gesamtvolumen durch zwei Bereiche angenähert, einer bei der Messtemperatur und der andere bei Raumtemperatur. Messungen des leeren Probenhalters ergaben für Wasserstoffadsorptionsmessungen bei 19,5 K eine Ungenauigkeit von $18 \mu\text{g}$ ($0,4 \text{ cm}^3$ (STP)).

Diese Apparatur ermöglicht erstmals die Messung von Wasserstoffadsorptionsisothermen bei 19,5 K bis zum Verflüssigungsdruck.

Ergebnisse

In Bild 3.28 ist die Wasserstoffaufnahme von MIL-101 bei 19,5 K in Abhängigkeit des relativen Drucks gezeigt. Der relative Druck ist hierbei der gemessene Druck normiert auf den Verflüssigungsdruck bei 19,5 K von 0,76 bar. Die Wasserstoffaufnahme ist in $\text{cm}^3(\text{STP}) \text{ g}^{-1}$ angegeben. Die Wasserstoffadsorptionsisotherme des mesoporösen MIL-101 zeigt ein charakteristisches Typ I-Verhalten (IUPAC [10]), das ausgeprägter ist als bei den mikroporösen Materialien bei 77 K. Die Sättigung ist bei relativen Drücken von 0,5 erreicht und beträgt $1200 \text{ cm}^3 \text{ g}^{-1}$ (10,8 wt%) was deutlich über der maximalen Wasserstoffaufnahme von 4,62 wt% bei 77 K liegt. Die gemessenen Desorptionsisothermen zeigten keine Hysterese zu den Adsorptionsisothermen, was typisch für Physisorption in Mikroporen ist. Um das Adsorptionsverhalten bei niedrigen Drücken besser zu untersuchen, sind die Isothermen der supermikroporösen und mesoporösen MOFs in Bild 3.29-3.35 mit logarithmischer Druckachse dargestellt. Für die beiden ultramikroporösen MOFs liegt die Wasserstoffaufnahme bei 19,5 K unterhalb der Messgenauigkeit. Die anderen Materialien haben bei dieser Temperatur Aufnahmen zwischen 300 cm^3 (2,7 wt%) für DUT-4 und 1550 cm^3 (14 wt%) für MOF-177. In der halblogarithmischen Darstel-

lung sind die Formen der Adsorptionsisothermen der verschiedenen Materialien sehr unterschiedlich wobei bei den meisten Isothermen mehrere Stufen erkennbar sind. Für MOF-5 wurde die Adsorptionsisotherme zusätzlich auch bei 25,5 K und 31,0 K gemessen (Bild 3.2.3). Dies führte zu einer Verschiebung der oberen Stufen zu höheren Relativdrücken. Aus den Wasserstoffisothermen werden erstmals spezifische BET Oberflächen und Porenvolumina von MOFs bestimmt. Die Oberflächen und Porenvolumina sind in Tabelle 3.4 zusammengefasst.

Um den Einfluss der Temperatur auf die adsorbierte Menge zu untersuchen, werden temperaturabhängige Messungen durchgeführt. Der Probenhalter wird bei Raumtemperatur mit 1,1 bar Wasserstoff gefüllt und das Ventil zum Probenhalter geschlossen. Anschließend wird der Probenhalter auf ungefähr 11 K abgekühlt und danach auf verschiedene Temperaturen geheizt die für circa 2 min konstant gehalten werden. Der Druck in Abhängigkeit der Temperatur ist in Bild 3.36 für den leeren Probenhalter und MIL-101 gezeigt. Bei tiefen Temperaturen bleibt der Wasserstoff adsorbiert und es entsteht ein großer Druckunterschied zwischen dem leeren Probenhalter und der gemessenen Probe. Bei steigender Temperatur beginnt die Probe Wasserstoff zu desorbieren und der Druck im Probenhalter nähert sich dem Druck des leeren Probenhalters an. Aus diesen Messungen wird die aufgenommene Menge Wasserstoff in Abhängigkeit der Temperatur und des Drucks berechnet (Bild 3.37-3.41). Hierbei zeigt sich ein sehr unterschiedliches Verhalten für die ultramikroporösen Materialien im Vergleich zu den supermikro- und mesoporösen Materialien. Bei den supermikro- und mesoporösen Materialien ist die aufgenommene Menge Wasserstoff bei niedrigen Temperaturen konstant und nimmt mit steigender Temperatur ab. Der Druck im Probenhalter steigt dabei an. Für die ultramikroporösen Materialien ist bei Temperaturen unterhalb von ungefähr 80 K ein Anstieg der Aufnahme und ein Absinken des Drucks mit steigender Temperatur zu beobachten. Bei höheren Temperaturen sinkt die Aufnahme und der Druck steigt mit zunehmender Temperatur. Bei anschließendem langsamen Abkühlen sind die Aufnahmen höher als die zuvor gemessenen. Kinetische Messungen von MFU-4 (Bild 3.42) zeigen, dass die zeitliche Druckänderung stark von der Temperatur abhängt.

Diskussion

Für die supermikro- und mesoporösen Materialien werden aus den Wasserstoffadsorptionsisothermen die spezifischen Oberflächen und die Porenvolumina bestimmt. Eine Korrelation dieser beiden Größen (Bild 3.43) zeigt, dass das Porenvolumen linear mit der Oberfläche steigt, analog zu den aus Stickstoffadsorptionsisothermen bestimmten Porenvolumina und Oberflächen. Der lineare Zusammenhang zeigt, dass die Porendurchmesser zu klein sind um Wasserstoffmultilagen ausreichend Platz zu bieten.

Die Wasserstoffmenge in der adsorbierten Lage bei 77 K und 20 bar ist in Bild 3.44 in Abhängigkeit der für Wasserstoff zur Verfügung stehenden Oberfläche dargestellt. Hieraus zeigt sich, dass die Dichte der adsorbierten Lage größer ist als die Dichte von flüssigem Wasserstoff am kritischen Punkt, aber kleiner als die Dichte von flüssigem Wasserstoff am Siedepunkt.

Adsorptionsmessungen an Cu-BTC mit Stickstoff bei 77 K von Krawiec et al. [27] und Argon bei 87 K von Vishnyakov et al. [28] zeigten bei einer halb-logarithmischen Darstellung ein klares Stufenverhalten. Die beiden Stufen wurden den verschiedenen Adsorptionspotentialen in der kleinen und großen Pore für das jeweilige Gas zugeordnet. Bisher sind keine Messungen für die Adsorption von Wasserstoff bei der Siedetemperatur gemacht worden, die ein Stufenverhalten zeigen könnten. Die in dieser Arbeit gemessenen Wasserstoffadsorptionsisothermen bei 19,5 K zeigen in der halb-logarithmischen Darstellung für einige Materialien erstmals diese Stufen. Die Stufenbildung ist durch die Überlagerung verschiedener Langmuirisothermen zu verstehen wie in Bild 3.47 gezeigt. Die Langmuirisotherme zeigt bei einer logarithmischen Druckachse eine S-Form die durch eine Änderung der Bindungsenthalpie verschoben wird. Durch eine Überlagerung verschiedener Isothermen mit unterschiedlicher Bindungsenthalpie entsteht daher eine Adsorptionsisotherme mit Stufen in der halb-logarithmischen Darstellung. Die beobachteten Stufen wurden mithilfe von Literaturdaten aus Neutronenbeugungsexperimenten und theoretischen Simulationen den verschiedenen Adsorptionsplätzen in den MOFs zugeordnet. Dies ist das erste Mal, dass Adsorptionsplätze verschiedener Energie direkt in Wasserstoffadsorptionsisothermen identifiziert werden.

In den Messungen der Wasserstoffadsorption von MOF-5 bei drei verschiedenen Temperaturen wird der Einfluss der Temperaturerhöhung auf die Besetzung der verschiedenen Adsorptionsplätze beobachtet. Durch die Zunahme der thermischen Energie verschiebt sich bei einer Temperaturerhöhung von 6 K nur die Besetzung der schwächsten Adsorptionsplätze zu höheren relativen Drücken, wohingegen die Besetzung der beiden stärkeren Plätze unverändert bleibt. Bei einer Erhöhung auf 31 K verschiebt sich auch die Besetzung des mittelstarken Adsorptionsplatzes zu höheren Drücken.

Aus der Kristallstruktur wird die für verschiedene Gase zur Verfügung stehende Oberfläche theoretisch berechnet [8, 12, 13, 29]. Die spezifischen Oberflächen von MOFs die mit Wasserstoff, Stickstoff und Argon gemessen wurden und die theoretisch berechneten Oberflächen für die verschiedenen Gase sind in Bild 3.45 gezeigt. Für einige Materialien zeigen sich große Unterschiede zwischen den experimentell bestimmten Oberflächen und den theoretischen Oberflächen, da die Berechnungen für perfekte Kristalle durchgeführt wurden [8]. Die Änderung der Oberfläche für die verschiedenen Adsorptivmoleküle entspricht für die meisten MOFs der theoretischen Vorhersage, wobei die Oberfläche mit sinkender Größe des Adsorptivmoleküls wächst. MOF-177 ist der einzige MOF bei dem die Oberfläche sowohl experimentell wie auch theoretisch für das kleinere Wasserstoffmolekül kleiner ist als für das größere Stickstoffmolekül. Da die Wasserstoffoberflächen teilweise deutlich von den Stickstoffoberflächen abweichen, ist es empfehlenswert die Oberfläche für Wasserstoffspeichermaterialien mit Wasserstoff und nicht mit Stickstoff oder Argon zu bestimmen. Die Messung der Oberfläche mit Stickstoff oder Argon ist experimentell jedoch wesentlich einfacher realisierbar und kann als Abschätzung herangezogen werden.

Für die beiden ultramikroporösen Materialien, MFU-4 und Mg-Formiat, wird bei 77 K eine deutliche Wasserstoffadsorption gemessen wohingegen bei 19,5 K keine signifikanten Wasserstoffmengen adsorbiert werden. Die temperaturabhängige Messung der Wasserstoffaufnahme zeigt bei ungefähr 70 K für beide Materialien einen Anstieg der Wasser-

stoffaufnahmen mit steigender Temperatur. Die kinetischen Messungen zeigen, dass die Diffusionsgeschwindigkeit von Wasserstoff in MFU-4 temperaturabhängig ist. Bis 50 K kann Wasserstoff innerhalb der Beobachtungszeit nicht in MFU-4 hinein diffundieren und daher wird bei 19,5 K keine Wasserstoffaufnahme gemessen. Bei höheren Temperaturen wird die Diffusion jedoch immer schneller und daher zeigen beide Materialien bei 77 K eine deutliche Wasserstoffadsorption. Die Ursache für diese Blockade der Wasserstoffaufnahme bei niedrigen Temperaturen liegt entweder in energetischen Barrieren die die Diffusion verhindern oder an geringeren Vibrationen des Gerüsts bei tiefen Temperaturen.

MOFs in Wasserstofftanks

In einem Tank ist nicht die bisher diskutierte adsorbierte Menge ausschlaggebend, sondern die gesamte im Tank vorhandene Wasserstoffmenge. Diese beinhaltet auch den Wasserstoff der nicht adsorbiert sondern in der Gasphase ist. In Bild 3.55 sind diese Wasserstoffmengen bei 77 K für die verschiedenen MOFs dargestellt. Die höchste Wasserstoffmenge zeigt bei 20 bar MOF-177 mit 80 mg Wasserstoff in 1 g MOF und die niedrigste DUT-4 mit 25 mg. Für die Wasserstoffspeicherung in mobilen Anwendungen ist jedoch nicht nur das Gewicht sondern auch die Größe des Tanks wichtig. Daher werden für die untersuchten Materialien auch die volumetrischen Speicherdichten mithilfe der Kristalldichten berechnet. In Bild 3.56 ist die volumetrische Wasserstoffaufnahme in Abhängigkeit der gravimetrischen Aufnahme der verschiedenen Materialien bei 77 K und 20 bar dargestellt. Die volumetrisch höchste Dichte unter diesen Bedingungen zeigt Cu-BTC mit 41 g l^{-1} , während MOF-177 die höchste gravimetrische Aufnahme von 78 mg g^{-1} zeigt.

Wenn für das Entladen des Wasserstofftanks keine zusätzliche Pumpe genutzt wird, ist der Minimaldruck des Tanks bei 1 bar. Für die Nutzung des Wasserstoffs ist die relevante Menge daher nicht die maximal aufgenommene Wasserstoffmenge, sondern die Differenz der aufgenommenen Menge bei einem Betankungsdruck von beispielsweise 20 bar zu einem Restdruck von 1 bar ist. MOF-177 hat mit 65 mg g^{-1} die höchste nutzbare Menge aller untersuchten Materialien. Eine Temperaturerhöhung des Tanks während des Entladens bei gleichbleibendem Restdruck vergrößert die nutzbare Menge Wasserstoff in MOF-177 auf 75 mg g^{-1} .

Schlusswort

In dieser Arbeit wurden die Wasserstoffspeichereigenschaften von 10 verschiedenen MOFs untersucht und mit ihren strukturellen Eigenschaften korreliert. Die maximal aufgenommene Wasserstoffmenge steigt mit der Oberfläche der MOFs und ist unabhängig von ihrer chemischen Zusammensetzung. Die Bindungsenthalpie wird bei niedrigen Wasserstoffaufnahmen von den Metallzentren der MOFs bestimmt. Bei höheren Aufnahmen im technisch relevanten Bereich sind diese Metallzentren gesättigt und die Bindungs-

enthalpie hängt von der Porengröße der MOFs ab. Kleinere Poren zeigen eine höhere Bindungsenthalpie für Wasserstoffmoleküle.

Durch einen für diese Arbeit neu entwickelten Kryostat konnten erstmals Wasserstoffadsorptionsisothermen bei 19,5 K gemessen und die Besetzung der verschiedenen Adsorptionsplätze direkt als Stufen im Niederdruckbereich der Isotherme beobachtet werden. Aus diesen Isothermen wurden erstmals Oberflächen und Porenvolumina aus Wasserstoffadsorptionsmessungen unterhalb der kritischen Temperatur bestimmt.

Die Physisorption von Wasserstoff unter cryogenen Bedingungen ist eine vielversprechende Möglichkeit für die Speicherung von Wasserstoff in mobilen Anwendungen. Die Korrelation der Speichereigenschaften zu den strukturellen Parametern ermöglicht die Synthese von MOFs mit optimalen Wasserstoffspeichereigenschaften.

1 Introduction to hydrogen storage

The world's growing energy demand combined with the limited resources of fossil fuels requires a change to new energy sources and carriers. Hydrogen is a very promising candidate as future energy carrier. Using renewable energy sources for the production, hydrogen has no environmental impact, e.g. no CO₂ emission, as the only combustion product is water. Hydrogen can be used either in a combustion engine or more efficiently in a fuel cell to produce electric energy. Especially for mobile applications hydrogen is very favorable due to its high energy density.

For the wide use of hydrogen as a fuel one of the challenges to overcome is the storage. Especially in mobile applications many requirements need to be regarded for the storage, e.g. light weight, small size, easy handling, fast refueling and high security standards. Nowadays hydrogen is used only in small test fleets of fuel cell cars with two storage systems. The first is compressed hydrogen, which is stored in high pressure cylinders under 70 MPa at room temperature. The high pressure requires special vessels and a heat management system for the heat of compression evolved during filling. The second is liquid hydrogen at a temperature of -253°C which requires a very good isolation system. Two further drawbacks of this storage are the facts that one third of the energy content of liquid hydrogen is needed for the liquefaction and secondly the tank needs to be an open-system to avoid over-pressurization, which yields a boil-off of approximately 0.3-1 % per day. Therefore a lot of effort is put into the search of a storage system for hydrogen that neither needs the high pressure of 70 MPa nor the low temperature of -250°C .

One alternative to these systems is hydrogen storage in solids. Hydrogen can interact with solids by strong chemical binding, which forms metal hydrides or complex hydrides, or by weak physical adsorption (physisorption) between the molecules. For physisorption the interaction strength is typically around a few kJ mol^{-1} . Therefore, on the one hand, low temperatures are needed to store hydrogen as the interaction is not strong enough to store remarkable amounts at room temperature. On the other hand, the low interaction energy is favorable, as the heat of interaction is evolved when loading the system with hydrogen, and needs to be provided when the hydrogen is used.

The heat involved in physisorption and the amount of hydrogen that can be adsorbed strongly depend on the solid used. One new class of materials with high potential, amongst others in the field of hydrogen storage, are metal-organic frameworks (MOFs). These porous organic-inorganic compounds have extremely high surface areas and well defined framework structures.

In this thesis hydrogen adsorption is measured in ten MOFs with pores ranging from 3.4 Å to 34 Å and ultra-high surface areas of up to $5000 \text{ m}^2 \text{ g}^{-1}$. Adsorption and desorption isotherms are measured in two different regimes. First, at temperatures between

77 K and room temperature and pressure up to 2 MPa. From these measurements the isosteric heat of adsorption is determined in dependence of the hydrogen uptake for the whole range important for technical application. Second, hydrogen adsorption is measured at approximately 20 K and pressure up to 0.1 MPa. For this new measurement technique a cryostat was developed, tested and calibrated.

Hydrogen adsorption at 20 K enables for the first time the determination of specific surface area and specific pore volume by hydrogen. From theoretical calculations there are indications that the specific surface area and specific pore volume depend on the gas used for the determination and that surface areas and pore volumes available for hydrogen are remarkably different from the surface area and pore volumes determined by nitrogen or argon adsorption. Therefore, for the characterization of hydrogen storage materials the surface area and pore volume should be determined by hydrogen adsorption which is done in this work for the first time.

Furthermore, adsorbed hydrogen at 20 K is less mobile than at 77 K. Therefore, adsorption sites with different adsorption energy in the framework are subsequently filled. This filling can be observed from steps in the low pressure isotherm. Similar observations have been made before for nitrogen at 77 K and argon at 87 K, but never for hydrogen.

Finally the results of hydrogen storage experiments are discussed concerning the requirements for application in a tank system.

This work on the relation of hydrogen storage properties to the structure of MOFs will enable tailored synthesis of optimized MOFs for hydrogen storage application.

2 Fundamentals

2.1 Introduction to adsorption

2.1.1 Adsorption

Two non-polar atoms or molecules approaching each other feel a long-range attraction due to fluctuations in the electron shell, which is named van der Waals interaction. At a certain distance a short-range repulsion force, caused by an overlap of the eigenfunctions of these particles, appears and increases in strength when the particles get closer. Therefore they will remain at an equilibrium distance from each other where these two forces compensate each other. If this happens between an atom or molecule and another atom belonging to a surface of a material, it is called adsorption, physical adsorption or physisorption. Particles adsorbed on a surface form a layer where the density of the particles is increased compared to the gas phase. This layer is called the adsorbate, while the free particles in the gas phase are named adsorptive and the material providing the surface is the adsorbent.

In the adsorption process no chemical bonds are formed, therefore the heat of adsorption which is involved is low, e.g. for hydrogen it is typically around $1 - 10 \text{ kJ mol}^{-1}$ [5]. At temperatures higher than the critical temperature, gases are adsorbed in a monolayer on the surface. The heat of adsorption for the second and higher layers is smaller than for the first layer. Consequently, multilayers only start to form when the temperature is decreasing to close or below the critical temperature of the adsorptive. For hydrogen, the boiling temperature (20.4 K) and critical temperature (33.0 K) are very low as the heat of condensation is only 0.9 kJ mol^{-1} . Thus even at 77 K hydrogen is adsorbed in a monolayer and no multilayer adsorption takes place as in contrast to adsorption at 20 K.

The amount of gas adsorbed on a surface depends on the pressure. For physisorption a type I isotherm in the classification of the IUPAC [10] is typically observed which is schematically shown in figure 2.1. At low pressure the amount adsorbed increases linearly with pressure which is the so called Henry's law region. With increasing pressure the monolayer is getting saturated and therefore a strong deviation from linearity of the gas uptake to the pressure is observed before saturation is reached. If the temperature of the system is close or below the critical temperature of the adsorptive, the completion of the monolayer is followed by multilayer adsorption. Therefore at higher pressure the adsorbed amount increases linearly with pressure. For materials with very small pores almost no multilayer adsorption is observed and therefore the plateau of the isotherm is almost horizontal as shown in figure 2.1. At a pressure close to the pressure of liquefaction at that temperature (P/P_0 close to 1), the gas in the pores and the surrounding is

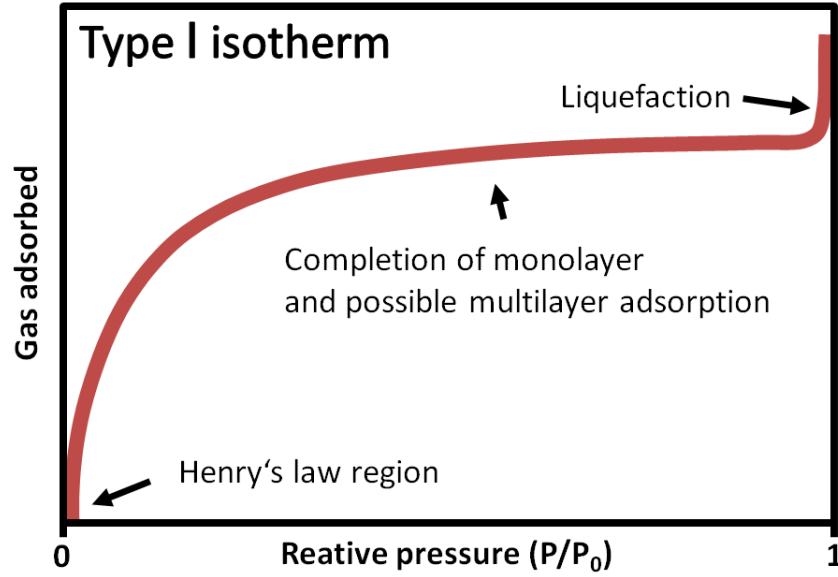


Figure 2.1: Type I isotherm of the IUPAC which is typical for physisorption on microporous materials and characterized by the steep initial increase and an almost horizontal plateau.

getting liquefied and therefore a strong increase of the adsorbed amount is observed.

2.1.2 Excess, absolute, and total adsorption

In figure 2.2 the gas density profile in a pore is shown schematically. Close to the pore walls the adsorbed gas has a high density which is close to the density of the liquid. The density decreases with increasing distance from the surface till a minimum is reached which is the density of the free gas and depends on the applied pressure.

Characterizing the adsorption system the excess hydrogen uptake n_{ex} is commonly reported. This is the amount of gas which is adsorbed additionally to the gas that would be present in the pore if there was no adsorption. In figure 2.2 this amount is represented by the areas **A** as the areas **B** and **C** represent the gas present in the free gas phase owing to the applied pressure. If the pressure is raising the density of the free gas rises and therefore the areas **B** and **C** are increasing, while the areas **A** will decrease as the upper limit of the density is defined by the density of the liquid. Therefore the adsorption isotherm shows a maximum if excess adsorption is reported, which is in contrast to the type I isotherm, shown in figure 2.1. This is because the amount adsorbed n_{ads} indicated in figure 2.1 refers to the so called absolute adsorption. This is the amount of gas which is adsorbed on the surface (areas **A** and **B** in figure 2.2) in contrast to molecules in the gas phase (area **C** in figure 2.2). Absolute adsorption cannot be measured experimentally and therefore it is calculated from the excess adsorption using approximations for the average density of the adsorbed gas and the volume of the adsorbed layer. Assuming the density of the adsorbed layer is equal to the density of the bulk liquid ρ_{lq} , the volume

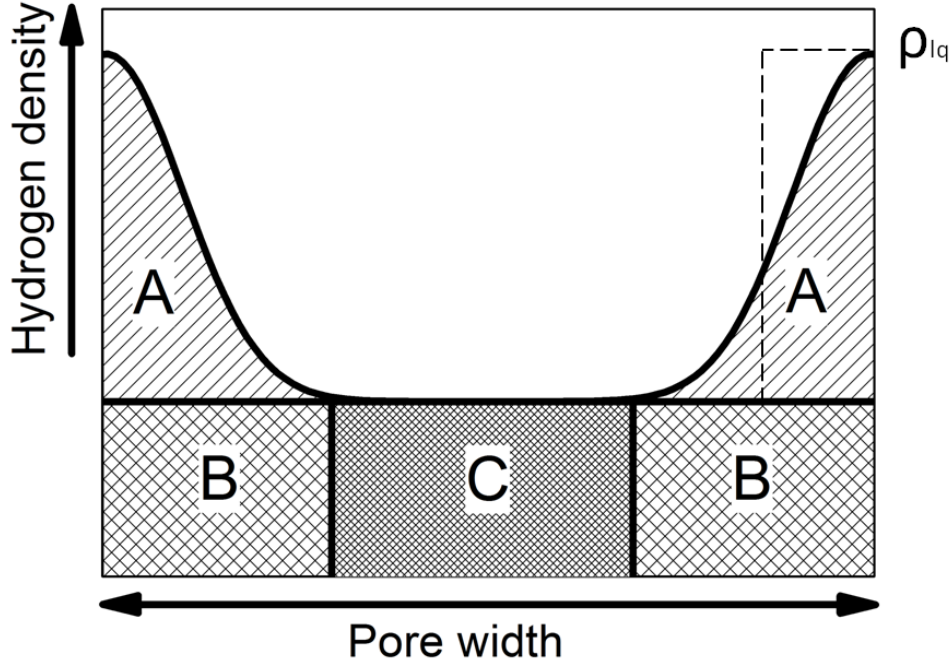


Figure 2.2: Hydrogen density profile in a pore. **A** denotes the excess, **A+B** the absolute, **A+B+C** the total adsorption and ρ_{lq} denotes the density of liquid hydrogen.

of the excess adsorbed layer V_{exc} (area **A** in figure 2.2) is approximately

$$V_{exc} = \frac{n_{exc}}{\rho_{lq}}. \quad (2.1)$$

This approximation underestimates the volume of the adsorbed layer as indicated with the dashed line in figure 2.2. The area within the dashed line is equivalent to area **A**, but as the density is assumed to be constant within the adsorbed phase, the thickness of this area is smaller than for area **A**. Thus the thickness calculated is less than the thickness of the area **B** indicated in figure 2.2. The estimated amount of gas present in the volume of the adsorbed layer (area **B** in figure 2.2) which is $n_{ads} - n_{exc}$, is given by the density of the gas phase using the corrected ideal gas equation. This yields

$$n_{ads} - n_{exc} = \frac{P}{Z \cdot R \cdot T} \cdot V_{exc} \quad (2.2)$$

$$n_{ads} = n_{exc} \cdot \left(\frac{P}{Z \cdot R \cdot T \cdot \rho_{lq}} + 1 \right) \quad (2.3)$$

with the correction factor Z for the non-ideal gas (see equation 4.1). If adsorption is used for storage purposes, the amount of interest is the total amount of gas present in the system. This is called total adsorption and represented in figure 2.2 by the areas **A**, **B** and **C**. If the material was a perfect single crystal, this parameter could be calculated

from the crystal data and the measured excess adsorption. The total adsorption is given by the excess adsorption (area **A**) adding the amount of gas in area **B** and **C** which is determined by the pore volume V_p and the pressure P

$$n_{tot} = n_{exc} + n_{B+C} \quad (2.4)$$

$$= n_{exc} + \frac{P \cdot V_p}{Z \cdot R \cdot T} \quad (2.5)$$

In reality the crystals are very small compared to the volume of a tank system and therefore inter particle space, which is influenced e.g. by the packing density, plays an important role. The total uptake is therefore actually the value which is of technical interest, but should be reported very carefully in order to make clear how it was evaluated [30].

Excess, absolute and total adsorption isotherms are shown for comparison schematically in figure 2.3. The excess uptake is the value which commonly reported in literature and,

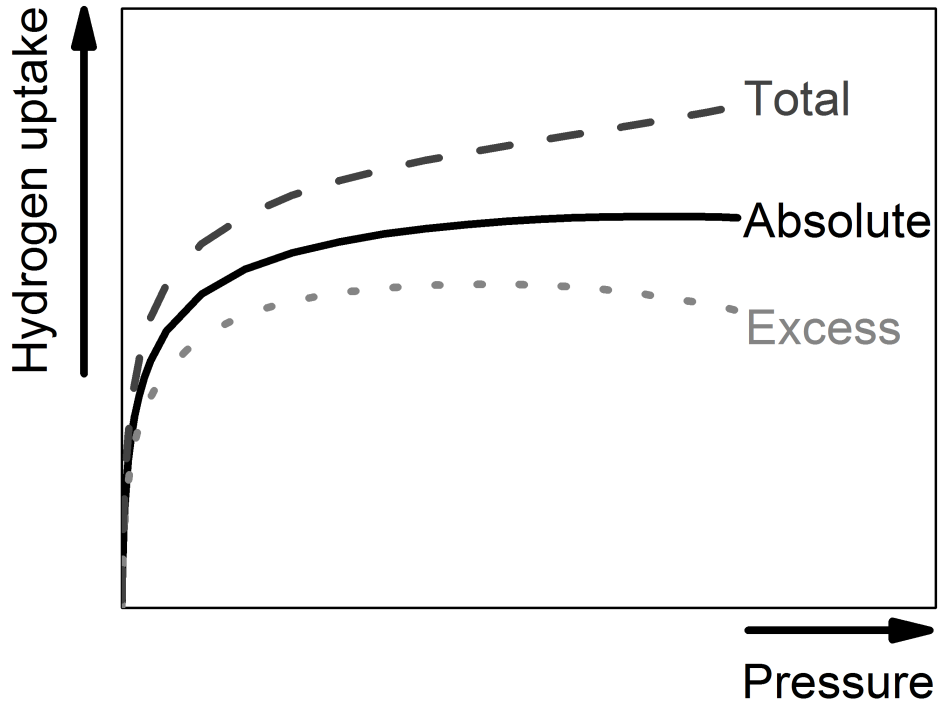


Figure 2.3: Typical isotherms for excess, absolute and total hydrogen uptake.

at the same time, the lowest. Absolute adsorption should exhibit a horizontal plateau and is higher than the excess uptake. The largest numbers are obtained from total adsorption which exhibits a linear rise of the hydrogen uptake at high pressure. This is due to the increasing density of the gas phase with increasing pressure.

2.1.3 Interpretation and theoretical description of adsorption isotherms

There are many theoretical models describing the adsorption of gases on porous system which are unlimited in complexity going as far as grand canonical Monte Carlo simulations or quasi liquid density functional theory. In the following some fundamental models which have been used for a long time and yield reasonable results are introduced.

Henry model

At very low surface coverage and high temperatures the adsorption only depends on the available gas molecules. This is the Henry's law region where the adsorbed molecules are independent of each other. The adsorbed amount correlates in this region linear with the pressure

$$n_{ads} = k_H \cdot P \quad (2.6)$$

with the Henry constant k_H . For experimental isotherms at cryogenic conditions the Henry's law region is often not well defined as strong deviations from linearity are observed even at very low pressure.

Langmuir model

The Langmuir model [6] was already proposed in 1916 and is one of the most often used models to describe adsorption isotherms. Assuming the adsorbent consists of a limited number of adsorption sites n_m , for any number of adsorbed molecules n , a fractional coverage $\theta = \frac{n}{n_m}$ of these sites can be calculated. The rate of adsorption depends on the pressure of the gas P , the number of unoccupied sites $1 - \theta$, and the affinity of the gas molecules to get adsorbed which is presented by the affinity coefficient α . The rate of adsorption $\frac{dn_a}{dt}$ can thus be written as

$$\frac{dn_a}{dt} = \alpha \cdot P \cdot (1 - \theta). \quad (2.7)$$

Analogue the rate of desorption $\frac{dn_d}{dt}$ depends on the affinity coefficient β , the surface coverage and the energy of activation

$$\frac{dn_d}{dt} = \beta \cdot \theta \cdot \exp\left(\frac{-E}{R \cdot T}\right). \quad (2.8)$$

In equilibrium the adsorption and desorption rates are equal and therefore

$$\alpha \cdot P \cdot (1 - \theta) - \beta \cdot \theta \cdot \exp\left(\frac{-E}{R \cdot T}\right) = 0. \quad (2.9)$$

If the affinity coefficients for adsorption and desorption are combined in a factor $K = \frac{\alpha}{\beta}$ and a new adsorption coefficient is introduced which is $b = K \cdot \exp\left(\frac{-E}{R \cdot T}\right)$ equation 2.9 can

2 Fundamentals

be rearranged to

$$\theta = \frac{b \cdot P}{1 + b \cdot P} \quad (2.10)$$

which is the Langmuir equation. Obviously there is no attention paid to energetically heterogeneous adsorption sites, interaction between the adsorbed molecules or multilayer adsorption at low temperature. At low pressure the Langmuir model reduces to the Henry model.

Commonly, for the evaluation of the monolayer capacity the linear form of the Langmuir equation

$$\frac{P}{n} = \frac{1}{n_m \cdot b} + \frac{P}{n_m} \quad (2.11)$$

is fitted to the measured adsorption isotherm. The maximum number of adsorption sites n_m , which represents the full coverage of the available surface with a monolayer of adsorbate, enables the calculation of the specific surface area (SSA) of the material. If the cross-sectional area A_c of the adsorbed molecules is known, the SSA is given as

$$SSA = A_c \cdot n_m. \quad (2.12)$$

The cross-sectional area A_c is most commonly calculated from the density of the liquid, assuming hexagonal closest packing of the molecules. For nitrogen and hydrogen this yields 16.2 \AA^2 and 14.2 \AA^2 , respectively.

Brunauer-Emmett-Teller model

At low temperature close to the critical point of the adsorptive, gas molecules can adsorb on the adsorbate itself and thereby form multilayers. Brunauer, Emmett, and Teller (BET) were able to extend the Langmuir model to multilayer adsorption in 1938 [7]. The general equation 2.9 can be rewritten for multilayer adsorption

$$\alpha_i \cdot P \cdot (1 - \theta_i) = \beta_i \cdot \theta_i \cdot \exp\left(\frac{-E_i}{R \cdot T}\right) \quad (2.13)$$

where $i \geq 1$ is the number of the layer and $i = 0$ presents the uncovered surface. Such multilayer adsorption is schematically shown in figure 2.4. Assuming an infinite number of layers can be adsorbed and the sum of all fractional coverages equals unity, $\sum_{i=0}^{\infty} \theta_i = 1$,

as schematically shown in figure 2.4, the total adsorbed amount is given by $n = n_m \cdot \sum_{i=1}^{\infty} i \theta_i$ where n_m is the amount adsorbed in a monolayer.

Further assumptions need to be made for the BET equation: starting from the second layer the heat of adsorption E_i is equal to the heat of liquefaction E_L and the multilayer has an infinite thickness at the saturation pressure. Then the BET equation can be derived as

$$n = \frac{n_m \cdot C \cdot P}{(P_0 - P)(1 + (C - 1)\frac{P}{P_0})} \quad (2.14)$$

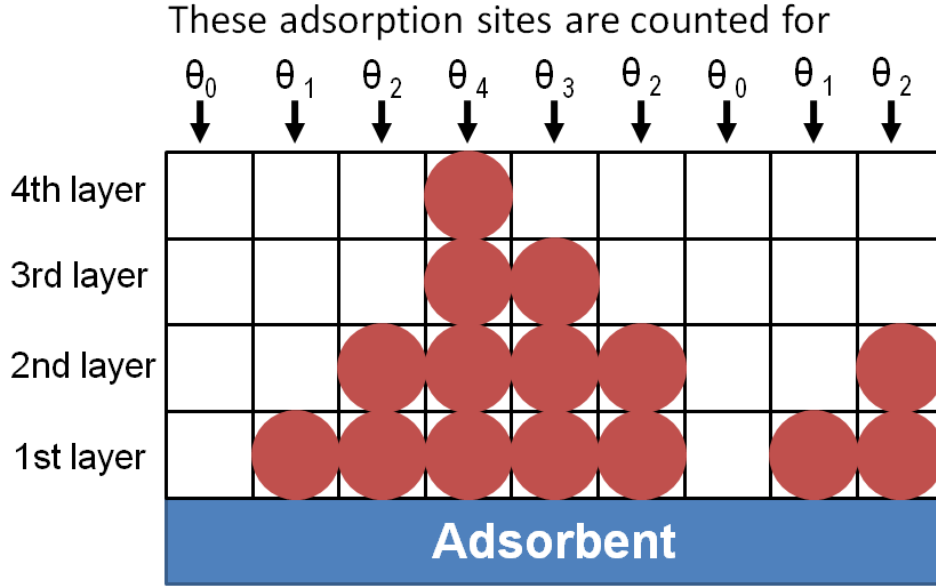


Figure 2.4: Sketch of multilayer adsorption denoting adsorption sites and layers.

with the BET constant C which is approximately $C \approx \exp\left(\frac{E_1 - E_L}{R \cdot T}\right)$. To fit the BET equation to experimental isotherms a linear version is used

$$\frac{p}{n \cdot (1 - p)} = \frac{1}{n_m \cdot C} + \frac{C - 1}{n_m \cdot C} \cdot p \quad (2.15)$$

and the SSA can be calculated from n_m according to equation 2.12.

At very low pressure ($P \ll P_0$) equation 2.14 reduces to

$$n = \frac{n_m \cdot C \cdot p}{1 + C \cdot p}, \quad (2.16)$$

which is the Langmuir equation derived for monolayer adsorption (section 2.1.3).

The BET and the Langmuir model are both based on assumptions that do not hold for real adsorption systems as e.g. no lateral interaction between the adsorbed molecules is allowed and all adsorption sites are energetically equal. Additionally, for the BET theory the number of possible adsorbate layers is limited in microporous materials. Regardless of these drawbacks both equations are widely used for the calculation of SSAs.

2.1.4 Adsorption in microporous materials

Pore shape and size

In the most simple model, a pore consists of two surfaces opposite to each other, which is a slit pore. The van der Waals potentials for adsorptive molecules of different diameter compared to the distance of the walls, the pore diameter, are shown in figure 2.5. If the

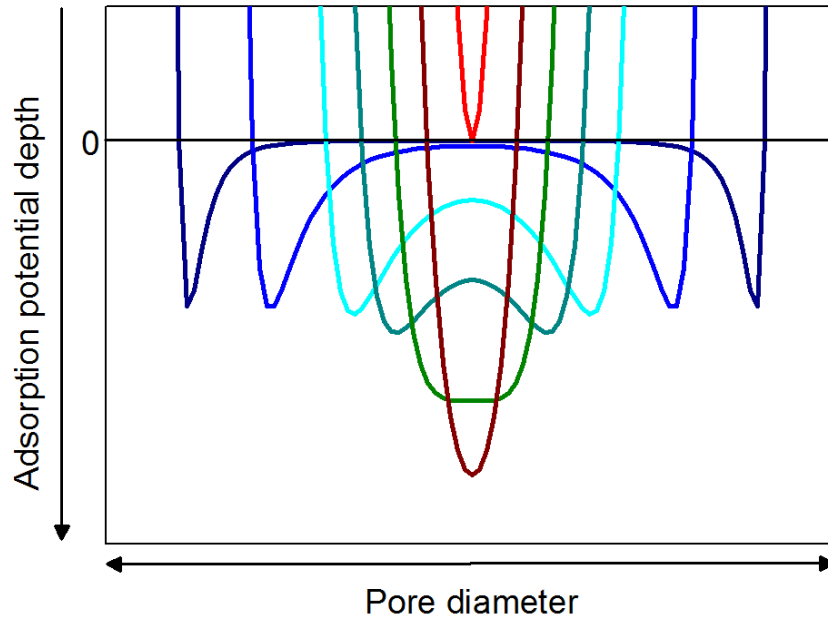


Figure 2.5: Simulation of van der Waals potentials for different ratios of adsorptive molecule diameter to pore diameter: 2:10, 4:10, 6:10, 7:10, 8:10, 9:10, and 10:10

adsorptive molecule is small compared to the diameter of the pore (2:10), the van der Waals potentials of the walls do not influence each other. When the adsorptive molecule is becoming larger compared to the pore diameter, the van der Waals potentials of the walls start to overlap. Until for a ratio of 9:10, the adsorption potential is doubled compared to the single surface potential. If the ratio is further increasing, the adsorption potential starts to decrease until the adsorptive cannot enter the pore anymore (ratio larger than 10:10). In microporous materials, surfaces are mostly not flat as in a slit pore. On a flat surface adsorbed molecules feel the van der Waals interaction of one or two atoms at the surface of the adsorbent. For surfaces exhibiting curvature, e.g. in spherical pores, the van der Waals potentials of these surface atoms overlap and strengthen the adsorption potential of the material. This overlap is getting stronger for decreasing pore size till the minima of the van der Waals potentials of opposite pore walls overlap. The increase in adsorption potential is therefore stronger than for the slit pore (figure 2.5) but the trend of first increasing and then decreasing adsorption potential is the same. Therefore the adsorption potential in microporous materials will not be uniform as it varies with the curvature of the surface and the distance to the opposite surface, i.e. pore size, position within the pore, windows between pores and outer surface.

Chemical composition

Another property of many microporous materials is that they are not composed of one single element but of a variety of different elements, e.g. MOFs. This inserts further energetic heterogeneity as the van der Waals interaction depends on the electron configuration of both partners and is therefore different for every element in the adsorbent. Furthermore in some microporous materials, e.g. zeolites or some metal-organic frameworks, not only van der Waals interaction but also electrostatic interaction with the adsorptive can occur and in some materials even strong chemical bonds can be formed. This can increase the adsorption potential strongly compared to pure physisorption.

Surface area

For Langmuir (section 2.1.3) and BET theory (section 2.1.3) an energetic homogeneous surface was assumed and furthermore for BET an unlimited multilayer adsorption. Both is not possible in microporous materials and therefore adsorption isotherms need to be analyzed very carefully. Another difficulty of surface area determination by gas adsorption was pointed out by Düren et al. [8] and is schematically shown in figure 2.6. Scanning a micropore with a small molecule slightly underestimates the inner surface

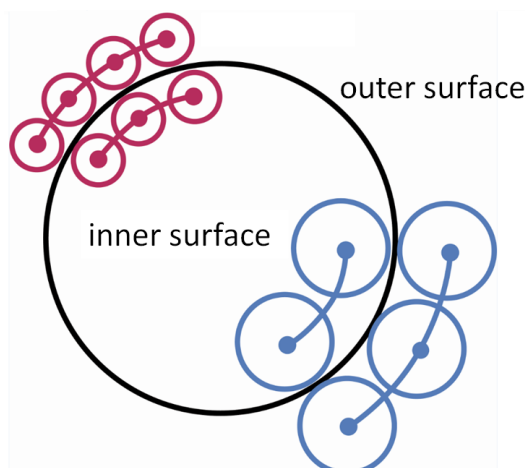


Figure 2.6: Scanning pores underestimates the inner- and overestimates the outer surface area depending on the probe molecule diameter. The measured area is therefore the accessible surface area for the respective molecule.

and at the same time overestimates the outer surface. For larger molecules the error in the determination of the specific surface area is higher. For the extreme case of molecules that cannot enter the pore, the inner surface is completely disregarded. Therefore an accessible surface area was defined that accounts for these variations with probe molecule diameter. A tool was developed that enabled calculation of the accessible surface area and the geometrical surface area from crystallographic data. The geometrical surface area is the area that would be measured by a probe molecule of infinitesimal size. This

model allows to compare surface areas of microporous materials determined by adsorption of different gases.

Pore volume

Gases adsorbed close to their critical temperature show monolayer adsorption at low pressure, followed by multilayer adsorption and depending on the pore structure pore condensation before liquefaction of the surrounding gas starts. In the case of microporous materials the pores are completely filled by a maximum of a few layers of adsorbate. Therefore pore condensation is not observed. The specific pore volume (SPV) of any material is determined by the maximum uptake (n_{max}) before liquefaction starts, typically at a relative pressure of 0.95. Assuming that the density of the adsorbate is approximately the density of the bulk liquid (ρ_{lq}), the pore volume is calculated according to Gurvich rule [9]

$$SPV = \frac{n_{max}}{\rho_{lq}} \cdot \frac{m_M}{m_s} \quad (2.17)$$

with the molecular mass m_M of the adsorptive and the mass of the sample m_s .

2.1.5 Enthalpy of adsorption

Adsorption of gas on a surface is a transition from a free gas with three degrees of freedom to a 2-dimensional adsorbed layer. Owing to the loss of one degree of freedom, adsorption is in general exothermic, i.e. heat is released. The amount of heat released is determined by the adsorption site and the adsorptive molecule.

In a Sieverts' type apparatus hydrogen adsorption is measured at constant temperature T and volume V . For the material investigated the surface area A and the volume are constant. Therefore the thermodynamic potential to describe the adsorption system is the Helmholtz energy $F_{T,V,A,n}$. The isosteric enthalpy of adsorption $\Delta_{ads} \dot{h}_{T,\theta}$ for the surface coverage of θ can be derived to

$$\Delta_{ads} \dot{h}_{T,\theta} = R \cdot \left(\frac{\partial \ln(P)}{\partial \frac{1}{T}} \right)_{\theta} \quad (2.18)$$

A detailed description of the derivation is given in "Adsorption by powders and porous solids" by Rouquerol et al. [31]. Assumptions made in the derivation are that the entire adsorption process is fully reversible and equilibrium was reached and maintained over the whole pressure range. Together with the assumption that A and V remain constant, this implies that the isosteric enthalpy of adsorption can e.g. not be calculated for materials changing their framework structure while adsorbing hydrogen or materials which form chemical bonds with hydrogen, as these are mostly non-reversible.

Equation 2.18 is analogue to the Clausius-Clapeyron equation for a one component gas-liquid system which can be achieved by integration of equation 2.18 for two temperatures T_1 and T_2

$$\Delta_{ads} \dot{h} = -R \cdot \frac{T_1 \cdot T_2}{T_2 - T_1} \cdot \ln \left(\frac{P_2}{P_1} \right) \quad (2.19)$$

From experimental data the isosteric enthalpy of adsorption can be calculated according to equation 2.18. The logarithm of the pressure which is needed to reach a certain surface coverage θ is plotted versus the reciprocal temperature in a Van't Hoff plot. In this representation the data should yield a linear correlation. The slope is proportional to the isosteric enthalpy of adsorption and can be determined more accurately if isotherms at many different temperatures are measured. A temperature difference of 10 K is recommended for the isotherms as small temperature fluctuations can be neglected and at the same time several isotherms can be measured within a set-up limited temperature range [31].

2.2 Metal-organic frameworks

There are two possibilities to produce a larger specific surface area (SSA). The first option is to decrease the particle size and thereby increase the outer surface area of the material. Problems arise when the particle size is reduced to extremely small diameters as the particles are thermodynamical not stable anymore which leads to an agglomeration of the particles. The second option is to introduce porosity and thereby produce an inner surface area. Porous materials are classified by their pore diameter, according to the IUPAC [10], as macroporous (pore diameter greater than 500 Å), mesoporous (pore diameter 20 – 500 Å), and microporous (pores of less than 20 Å in diameter). The last species is subdivided into ultramicroporous materials, having pore diameters of less than 7 Å, and supermicroporous, for pore diameters of 7 – 20 Å. In this work materials with ultramicropores, supermicropores and mesopores are investigated.

A new class of highly porous materials with large SSA are the so called metal-organic frameworks (MOFs). These metal-organic hybrid coordination polymers consist of organic linkers which connect metal ions or coordinated metal clusters and build a crystalline framework with high porosity, large SSA and low specific density. Most commonly transition metals are used to build up the metal complexes, but there are also some new reports on MOFs synthesized from lighter metals as e.g. Al^{3+} [32, 33] or Mg^{2+} [34, 35] which reduces the weight of the MOF. Additional to the metal, also the organic linker of the MOF can be varied which opens up a giant playground for modification of chemical composition and therefore pore size and SSA. In MOFs, all surfaces are accessible to gas owing to the framework structure and therefore MOFs exhibit extremely large SSAs. Furthermore, the framework topology is well defined and the structure can be tuned by using different metal clusters and linkers. This makes MOFs ideal candidates to study the fundamental relation of e.g. gas storage properties to framework topology. Nowadays it is possible to scale up the synthesis of many MOFs [36] which enables their testing in large prototype facilities and their technical application.

The MOFs investigated are characterized by their pore diameter, specific surface area (SSA), specific pore volume (SPV), and skeletal density which are presented at the end of the section in an overview table (2.1). The pore diameter is determined as the diameter of a sphere that can be included in the pore when taking account of the van der Waals radii of the wall atoms. The SSA is calculated according to the BET theory (section 2.1.3) from nitrogen adsorption measurements performed in house at 77 K if not cited otherwise. For microporous materials, the BET plot is mostly not linear in the standard pressure region used for BET (up to 0.35 [7]) and therefore the results obtained are not well reproducible and depend strongly on the data points measured. Rouquerol et al. [37] suggested stronger criteria that should be applied to determine the appropriate pressure range for the BET plot, e.g. a positive C constant and a monotonously increasing $n \cdot (P_0 - P)$. Using these stronger criteria for the application of the BET equation, Walton and Snurr [38] showed that BET SSAs for microporous metal-organic frameworks become well reproducible in different laboratories and agree with theoretically calculated surface areas. Therefore, these stronger criteria are applied to characterize the MOFs. From the nitrogen adsorption isotherms SPVs are calculated

at a relative pressure of 0.95 according to Gurvich's rule (section 2.1.4). The skeletal density is measured by helium at room temperature and approximately 0.2 MPa.

2.2.1 Ultramicroporous materials

Mg-Formate

The first MOF based on light weight magnesium atoms was reported in 2005 by Dinca and Long [34] and one year later a magnesium MOF with the shortest carboxylate ligand, formate, is reported [35]. Independently BASF SE found a semi-technical route to produce this Mg-formate efficiently in large scale [11] and kindly provided the material investigated in this work. The structure was analyzed by single crystal X-ray diffraction [11]. Each magnesium atom is coordinated by six oxygen atoms forming the metal complex. These metal complexes are interconnected by six formate molecules. Owing to the short ligand molecule the structure shows channels with an inner diameter of only 3.4-4.6 Å (fig. 2.7), which is in the range of the kinetic diameter of hydrogen molecules. Therefore, nitrogen cannot penetrate in the framework and a SSAs of only a few square meters per gram which is typical for nonporous powders are obtained from nitrogen adsorption [35, 11]. Large octahedral shaped single crystals of up to 100 µm diameter are observed in the SEM image (fig. 2.8).

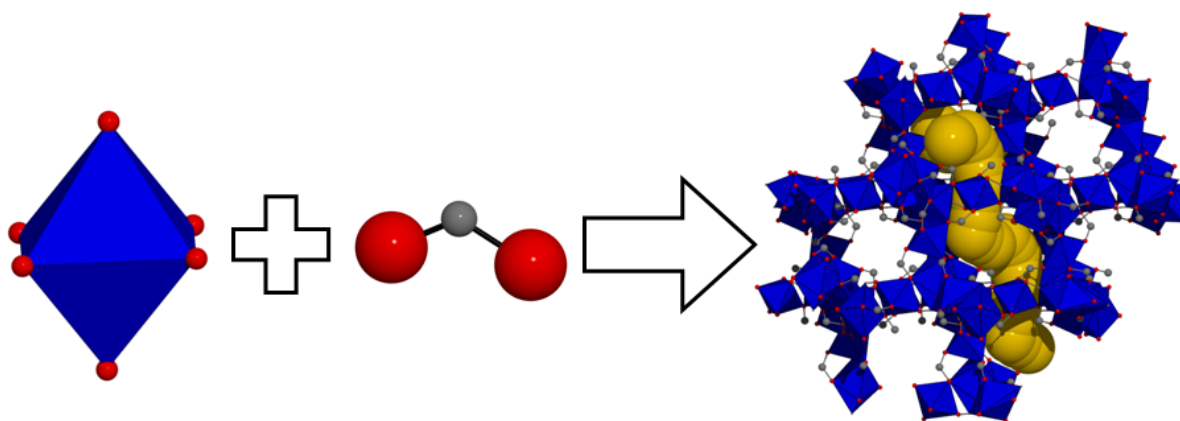


Figure 2.7: Left: magnesium complex (blue) consisting of a magnesium atom coordinated by six oxygen atoms. Middle: the formate ligand (C: dark grey, O: red). Right: the structure of Mg-formate along the (1,1,1) direction, which has interwoven zig-zag channels of 3.4 Å to 4.6 Å in diameter, indicated by the yellow spheres.

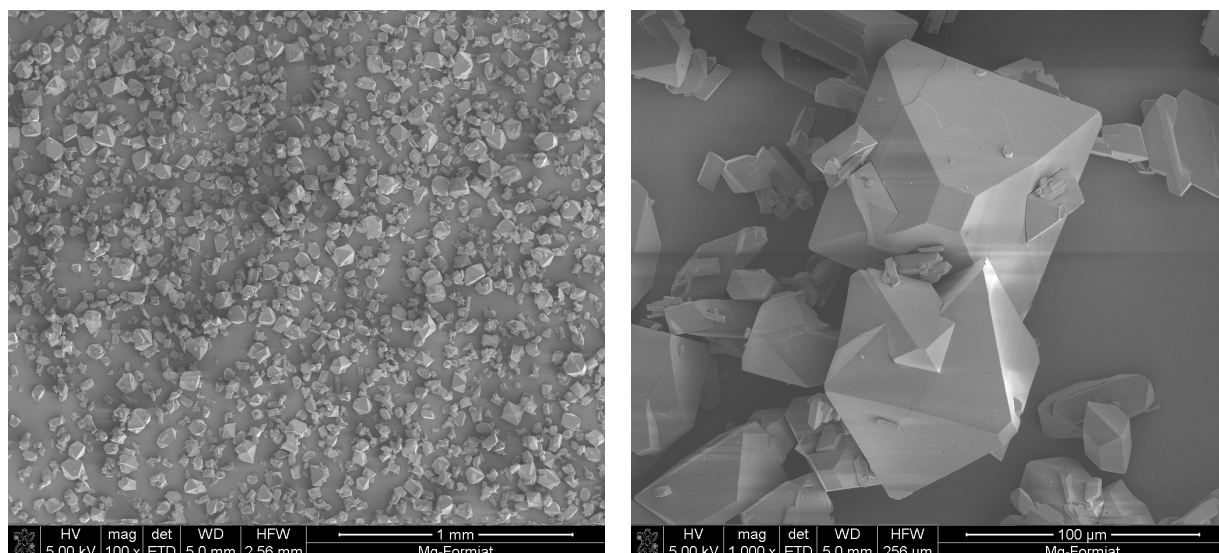


Figure 2.8: SEM images of Mg-Formate.

MFU-4

MFU is the abbreviation for Metal-organic Framework Ulm University. The MFU-4 consists of *BBTA* (=1H,5H-benzo(1,2-d:4,5-d')bistriazole) linkers which are connecting tetrahedral shaped pentanuclear $(\text{Zn}_5\text{Cl}_4)^{6+}$ subunits (Fig. 2.9). The first synthesis and structure determination is described in detail by Biswas et al [12]. The structure was determined by single crystal X-ray diffraction and the phase purity was confirmed by X-ray powder diffraction, IR spectroscopy, and elemental analysis. The framework shows a cubic structure with alternating pores of 3.87 Å and 11.9 Å in diameter (fig. 2.9). As all molecules need to pass the small pore in order to penetrate the framework it is accounted to be ultramicroporous. Nitrogen molecules are too big to enter the framework and therefore no nitrogen is adsorbed at 77 K and the SSA can therefore not be determined by nitrogen adsorption [12]. From theoretical calculations the accessible surface area according to Düren et al. [8] is calculated to $1611 \text{ m}^2 \text{ g}^{-1}$ [12]. In the SEM image (figure 2.10) mainly cubes around $3 \mu\text{m}$ and smaller fragments are observed.

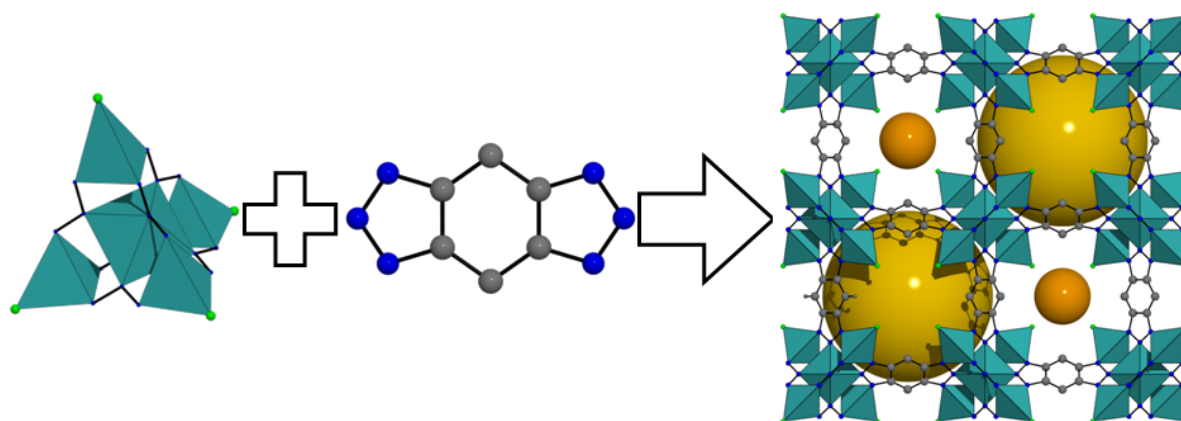


Figure 2.9: Left: the metal cluster containing five zinc atoms where the one in the middle is coordinated by 6 nitrogen atoms (blue) and the outer four zinc atoms are coordinated by three nitrogen and one chlorine (green) atom. Middle: BBTA, the linker of MFU-4 (C: dark grey). Right: Structure of MFU-4 with pore diameters of 3.87 Å (orange sphere) and 11.9 Å (yellow sphere) view along the (1, 0, 0) direction.

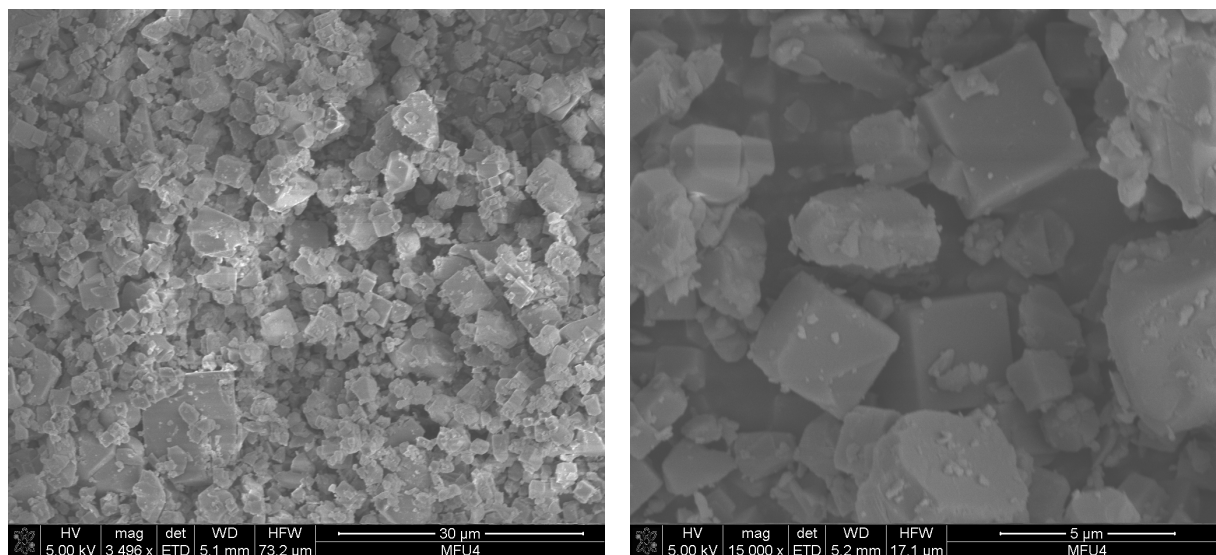


Figure 2.10: SEM images of MFU-4.

2.2.2 Supermicroporous materials

MFU-4 long

MFU-4 long (MFU-4L) is the first MFU-4 type framework with a more open structure than the original MFU-4. The synthesis is described in detail by Denysenko et al. [13], where also structure determination from X-ray powder diffraction and 3-dimensional electron diffraction is reported. The tetrahedral shaped pentanuclear $(\text{Zn}_5\text{Cl}_4)^{6+}$ metal clusters are the same as for MFU-4 but in MFU-4L they are interconnected by a longer linker (fig. 2.11). The linker is *BTDD* (= (bis-1H-1,2,3-triazolo-[4,5-b],[4',5'-i])dibenzo-[1,4]-dioxin) which has approximately double the length of *BBTA*. Owing to the

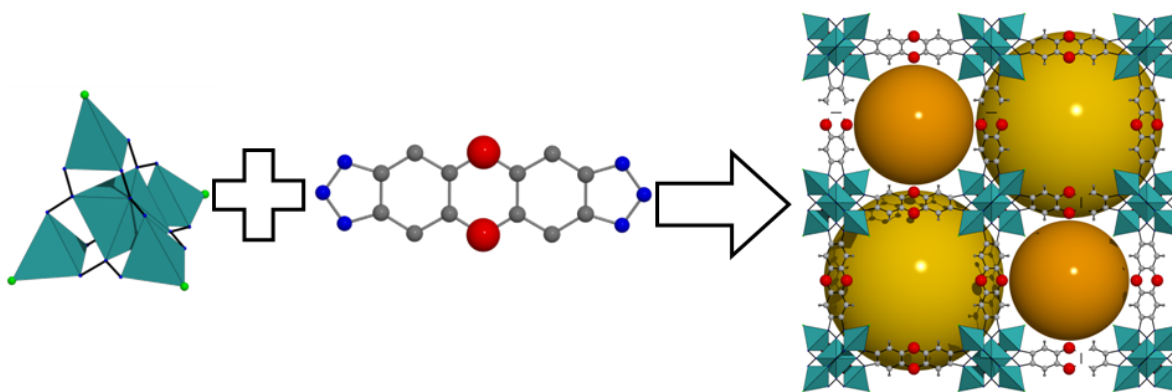


Figure 2.11: Left: the zinc cluster which is identical to MFU-4. Middle: BBDD, the linker of MFU-4L which is longer than for MFU-4 (C: dark grey, N: blue). Right: Structure of MFU-4L with pore diameters of 12.0 Å (orange sphere) and 18.6 Å (yellow sphere) view along the (0, 0, 1) direction.

identical metal cluster and the same functionality of the ligand, the framework has the same topology as MFU-4, but as the linker is longer, the pore size is increased to 12.0 Å and 18.6 Å. Also the aperture between the pores is larger with 9.13 Å compared to 2.52 Å in MFU-4. From nitrogen and argon [13] adsorption the SSA is determined to 2178 m² g⁻¹ and 2750 m² g⁻¹, respectively, and from theoretical calculations according to [8] an accessible surface area for argon and hydrogen is determined to 2987 m² g⁻¹ and 3095 m² g⁻¹, respectively [13]. In the SEM image cubic crystals of up to 4 μm are observed.

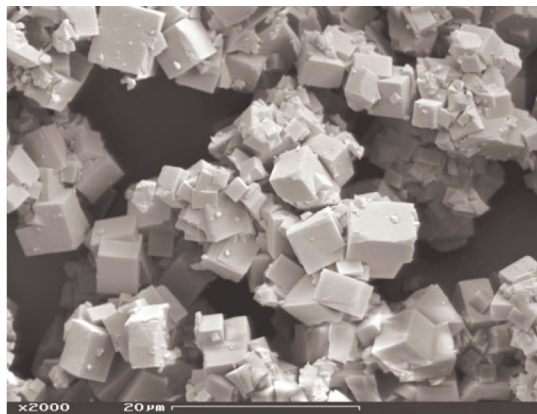


Figure 2.12: SEM image of MFU-4L from [13]

MOF-5

One of the most famous metal-organic frameworks is MOF-5 discovered by Yaghi et al. [14] in 1999. It consists of metal clusters built up from four zinc atoms each coordinated by four oxygen atoms sharing one central oxygen atom. The metal clusters are connected to each other by BDC (1,4-benzenedicarboxylate) and a 3-dimensional cubic framework is formed (fig. 2.13). Owing to the orientation of the aromatic ring in the

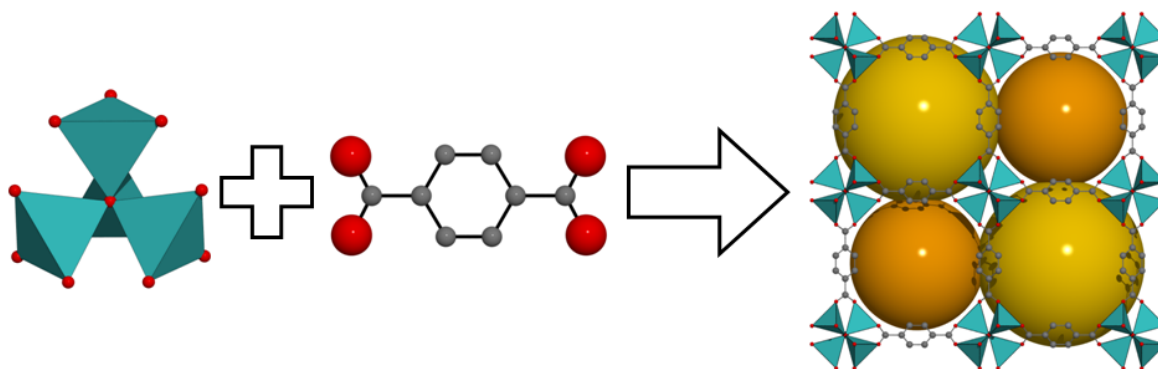


Figure 2.13: Left: Metal cluster containing four zinc (turquoise) atoms coordinated by 13 oxygen (red) atoms. Middle: BDC ligand (C: dark gray). Right: Structure of MOF-5 with pore diameters of 12 Å (orange sphere) and 15 Å (yellow sphere).

linker two different alternating pores are formed in MOF-5. In the smaller pore with a diameter of 12 Å the aromatic ring is pointing inside the pore whereas the larger pore with 15 Å in diameter is faced by the flat ring (fig. 2.13).

From this structure a whole series of isorecticular MOFs (IRMOFs) is formed with identical metal cluster but varying pore size due to different linkers. The MOF-5 is therefore also known as IRMOF-1.

The material investigated in this work was kindly provided by BASF SE and the synthe-

sis is described in [16]. The specific surface area is determined by nitrogen adsorption measurements at 77 K to $2360 \text{ m}^2 \text{ g}^{-1}$. From theoretical calculations an accessible surface area for hydrogen of $3895 \text{ m}^2 \text{ g}^{-1}$ is determined [29].

DUT-4 and DUT-5

DUT-4 and DUT-5 are two aluminum based metal-organic frameworks developed at the Dresden University of Technology (DUT). Synthesis and structure analysis is described in detail by Senkovska et al. [15]. DUT-4, which is $\text{Al}(\text{OH})(\text{ndc})$ (NDC=2,6-naphthalene dicarboxylate), is build up from chains of coordinated aluminum octahedra connected by NDC linkers (fig. 2.14). This forms a channel-like structure with a channel diameter of 9 \AA . DUT-5 possesses identical metal clusters like DUT-4 but the linker is longer.

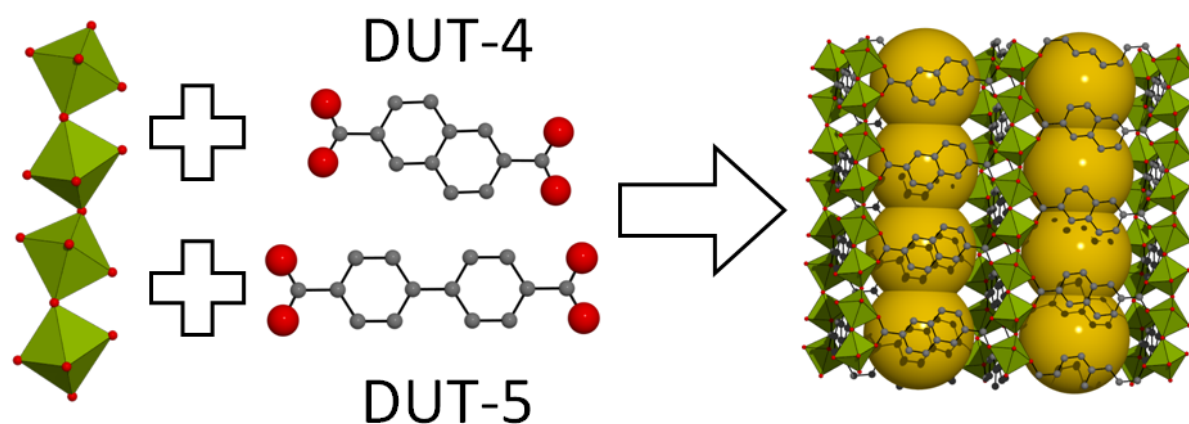


Figure 2.14: Building units of DUT-4 and DUT-5. Left: Aluminium clusters (green) form chains which are connected by NDC (middle top) and BPDC (middle bottom) for DUT-4 and DUT-5, respectively. (C: dark grey, O: red) Right: Structure of DUT-4 with channels of 9 \AA in diameter indicated by the yellow spheres.

For DUT-5 the aluminum chains are connected via 4,4'-biphenyldicarboxylate (BPDC) instead of NDC (fig. 2.14). This gives rise to a channel diameter of 11 \AA .

Irregular shaped crystals of approximately $1 \mu\text{m}$ in diameter are observed on the SEM picture (fig. 2.15). For DUT-4, the SSA is determined by nitrogen adsorption to $601 \text{ m}^2 \text{ g}^{-1}$ and the accessible surface area [29] for hydrogen, argon, and nitrogen is $2393 \text{ m}^2 \text{ g}^{-1}$, $2213 \text{ m}^2 \text{ g}^{-1}$, and $2090 \text{ m}^2 \text{ g}^{-1}$, respectively. For DUT-5 the SSA is determined by nitrogen and argon [39] adsorption to $1351 \text{ m}^2 \text{ g}^{-1}$ and $1554 \text{ m}^2 \text{ g}^{-1}$, respectively. The accessible surface area [29] is calculated to $2766 \text{ m}^2 \text{ g}^{-1}$, $581 \text{ m}^2 \text{ g}^{-1}$, and $2479 \text{ m}^2 \text{ g}^{-1}$ for hydrogen, argon, and nitrogen, respectively.

Senkovska et al. [15] reported a nitrogen uptake of DUT-4 and DUT-5 at 77 K of $450 \text{ cm}^3 \text{ g}^{-1}$ and $550 \text{ cm}^3 \text{ g}^{-1}$ (STP), respectively, which is both remarkably higher than

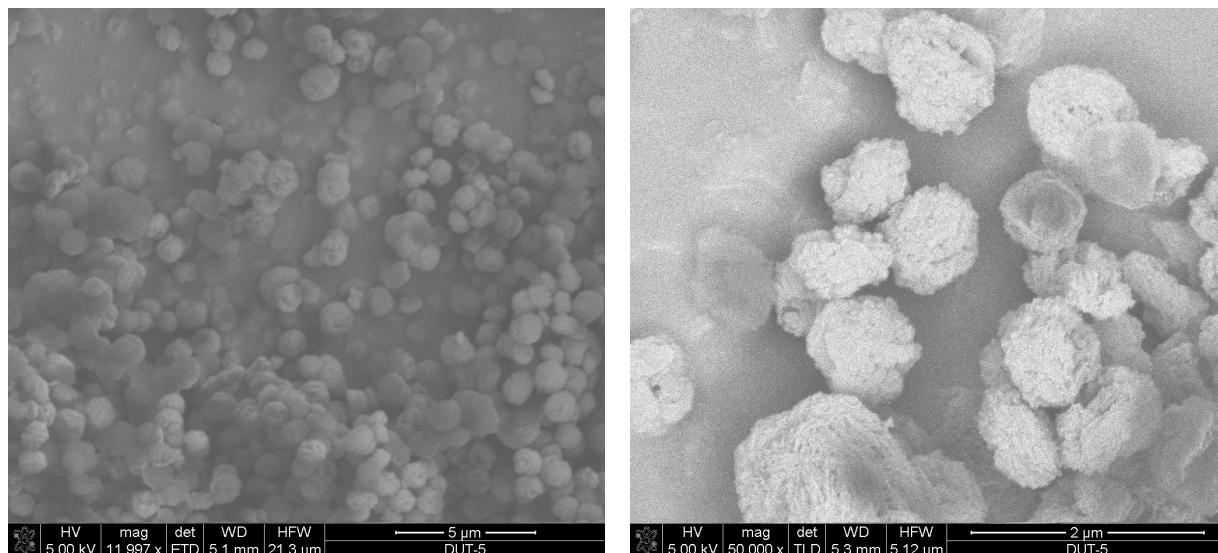


Figure 2.15: SEM images of DUT-5.

our results of $200 \text{ cm}^3 \text{ g}^{-1}$ and $400 \text{ cm}^3 \text{ g}^{-1}$. This is an indication that the frameworks partly decomposed between the two measurements. The hydrogen uptake at 77 K and higher temperatures of the materials was investigated shortly after synthesis and the nitrogen adsorption in house was measured approximately one year later at the same time as the 20 K hydrogen adsorption isotherms. Therefore the SSA of the material might have been remarkably higher at the time of the hydrogen adsorption measurement at 77 K. From the nitrogen adsorption experiment Senkovska et al. [15] calculated BET SSAs for DUT-4 and DUT-5 of $1308 \text{ m}^2 \text{ g}^{-1}$ and $1613 \text{ m}^2 \text{ g}^{-1}$, respectively. Therefore in the following the freshly synthesized materials are named by DUT-4f and DUT-5f with SSAs of $1308 \text{ m}^2 \text{ g}^{-1}$ and $1613 \text{ m}^2 \text{ g}^{-1}$, respectively, while the materials investigated one year later are named DUT-4o and DUT-5o with SSAs of $601 \text{ m}^2 \text{ g}^{-1}$ and $1351 \text{ m}^2 \text{ g}^{-1}$, respectively.

Cu-BTC

Cu-BTC, also named HKUST-1, consists of octahedral copper complexes connected by benzene-1,3,5-tricarboxylate (BTC). This leads to the formation of pores with a free inner diameter of 9 \AA and small side pockets which have a diameter of 5 \AA (fig. 2.16). As the larger pores are directly connected to each other, molecules do not need to pass through the small 5 \AA pore to penetrate the structure. Therefore it is accounted to the supermicroporous materials. The material investigated was provided by BASF SE and the electrochemical synthesis is described in [16, 17]. The SSA determined by nitrogen adsorption at 77 K is $1527 \text{ m}^2 \text{ g}^{-1}$ and for argon adsorption $1499 \text{ m}^2 \text{ g}^{-1}$. Theoretical

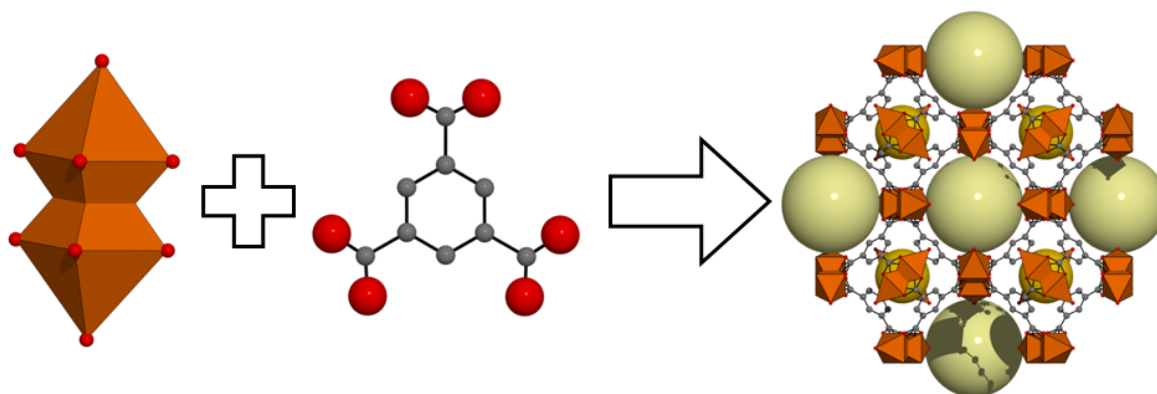


Figure 2.16: Left: The metal complex (orange) consists of two copper atoms coordinated by ten oxygen atoms (red). Middle: the metal complexes are interconnected by BTC ligands (C: dark gray). Right: Structure of Cu-BTC with pore diameters of 5 Å (dark yellow sphere) and 9 Å (light yellow sphere).

calculations of the ASA for nitrogen, argon, and hydrogen yield $2268 \text{ m}^2 \text{ g}^{-1}$, $2449 \text{ m}^2 \text{ g}^{-1}$, and $2691 \text{ m}^2 \text{ g}^{-1}$, respectively. The Cu-BTC powder is turquoise when in contact with humidity from air and turns dark blue by heating under vacuum. On the SEM image (fig. 2.17) small crystals of approximately $2 \mu\text{m}$ are shown. At higher resolution also some mesopores and even macropores of $200 - 600 \text{ Å}$ are observed.

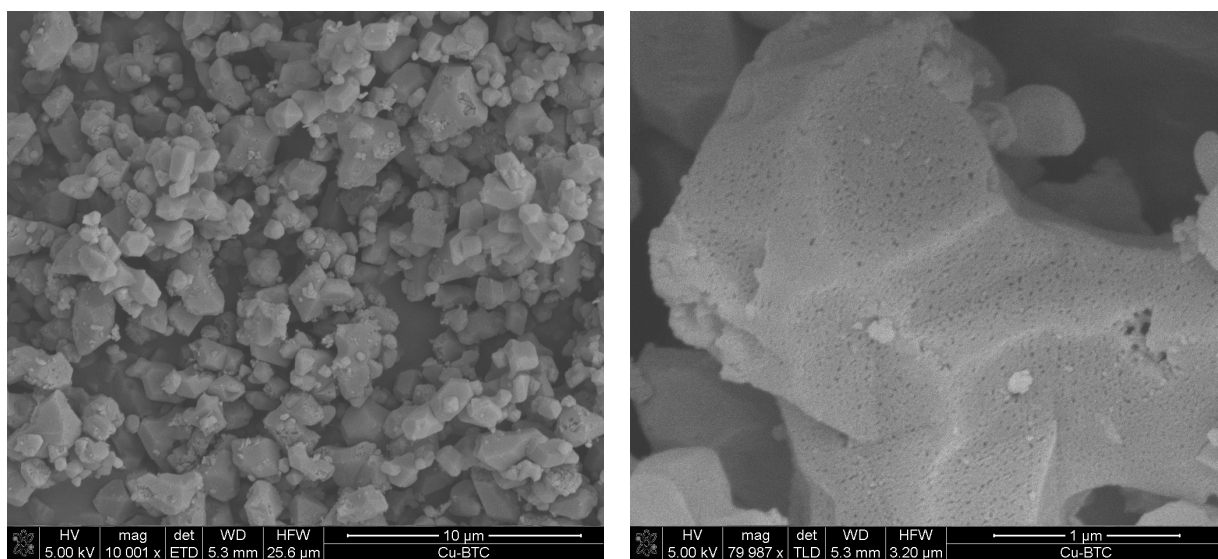


Figure 2.17: SEM images of Cu-BTC.

MOF-177

MOF-177 was reported for the first time by the group of Omar Yaghi in 2004 [18]. With a SSA of $4728 \text{ m}^2 \text{ g}^{-1}$ determined by nitrogen adsorption it was the MOF with the highest SSA until MOF-210 was synthesized in 2010 [40]. As shown in figure 2.18, it consists of Zn_4O clusters connected via BTB-linkers (benzene-1,3,5-tribenzoate), which forms a very open framework structure with ellipsoid shaped pores. When taking van der Waals radii of the wall atoms into account it can accommodate a sphere of 11 \AA in diameter which represents the short axis, while the long axis is 19 \AA . The material

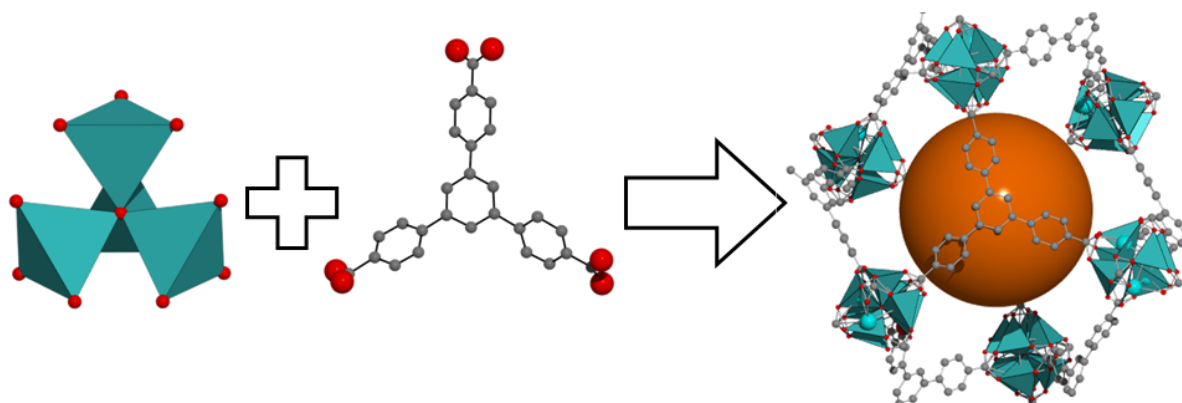


Figure 2.18: Left: MOF-177 is built up from Zn_4O clusters (turquoise) and BTB linkers (C: dark grey, O: red). Right: MOF-177 has ellipsoidal pores (orange sphere) with a short axis of 11 \AA and a larger axis of 19 \AA .

investigated was synthesized and provided by BASF SE. The accessible surface area [29] is $4790 \text{ m}^2 \text{ g}^{-1}$ and $4722 \text{ m}^2 \text{ g}^{-1}$ for nitrogen and hydrogen, respectively. In the SEM image 2.19 large grains with a diameter of approximately $50 \mu\text{m}$ are observed. They are build up from layer-like structures which seem to have no well defined orientation to each other.

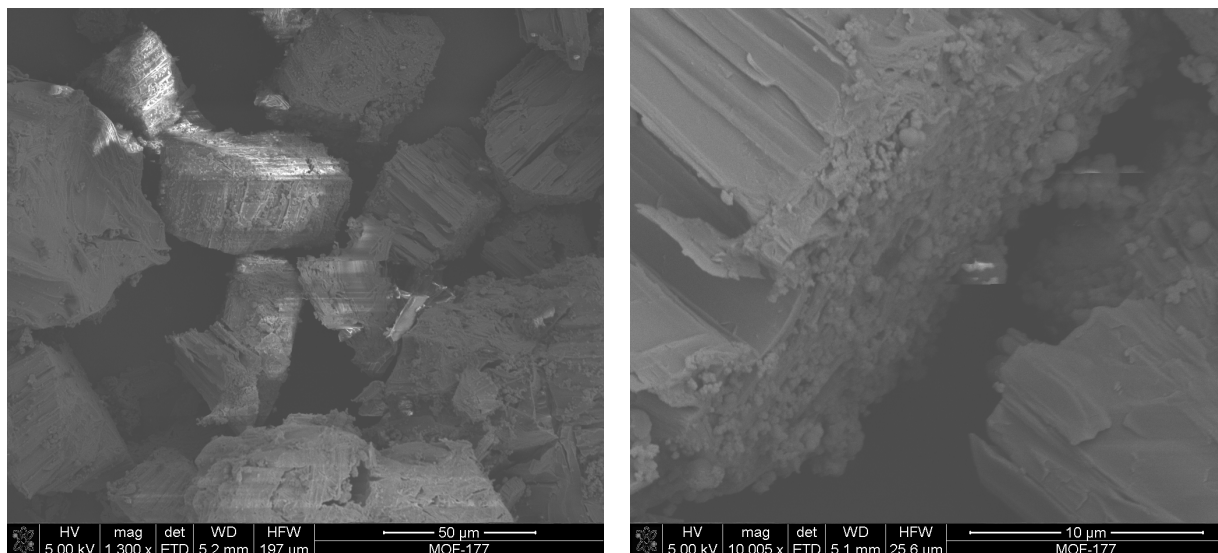


Figure 2.19: SEM image of MOF-177

2.2.3 Mesoporous materials

MIL-101

MIL-101 (Materials of Insitut Lavoisier) was first reported in 2004 by Férey et al. [19, 20] who kindly provided the material investigated. It is built up from chromium clusters connected by BDC ligands, which form small tetrahedrons having an inner diameter of 7 Å (fig. 2.20). These tetrahedrons share their edges and form two large mesoporous cages. The smaller one is build up from chromium tetrahedrons forming pentagonal openings and has a free inner diameter of 29 Å. The larger pore has pentagonal as well as hexagonal windows and has therefore a larger pore diameter of 34 Å. This is one of the largest pore sizes observed so far for metal-organic frameworks and offers therefore unique possibilities to store large molecules as for example important for medical applications [41]. MIL-101 has a very high SSA determined by nitrogen adsorption at 77 K of 3007 m² g⁻¹. In the SEM image figure 2.21 small octahedral single crystals with a diameter of approximately 500 nm can be observed.

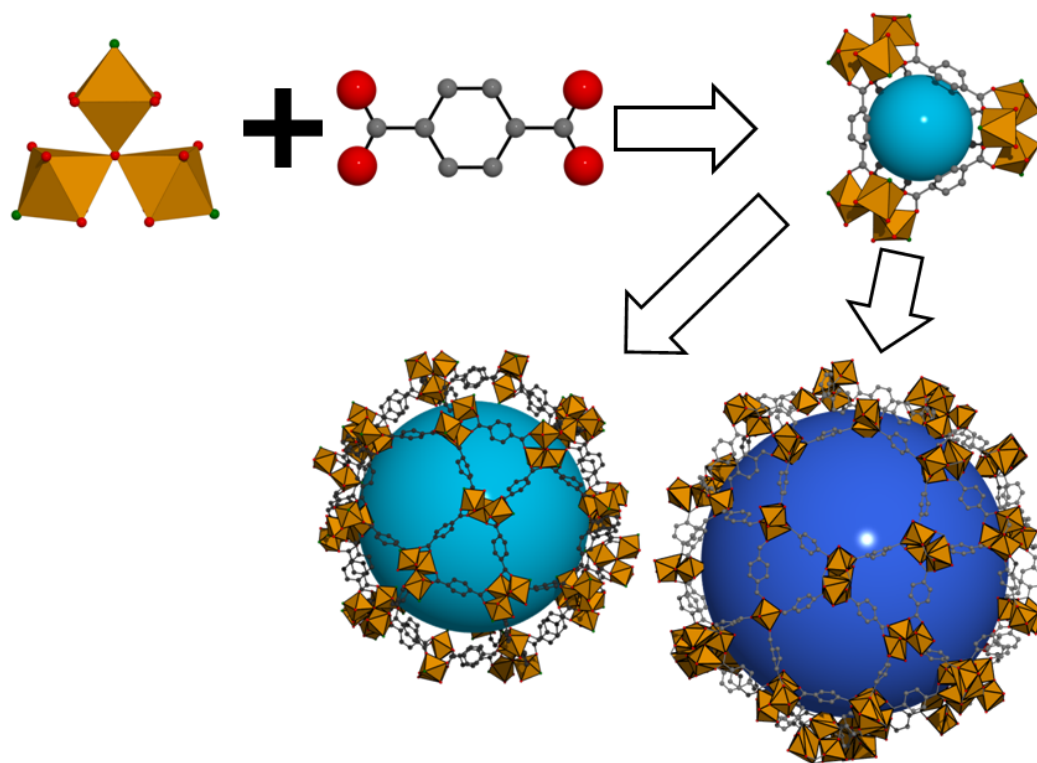


Figure 2.20: Building units of MIL-101. Top row: left: chromium cluster (orange) (O: red, F: green), middle: BDC ligand (C: dark grey), right: small tetrahedral side pocket of approximately 7 Å diameter. Bottom row: medium (29 Å) and large (34 Å) pore with a diameter of 34 Å build up from triangular structure of the small side pocket.

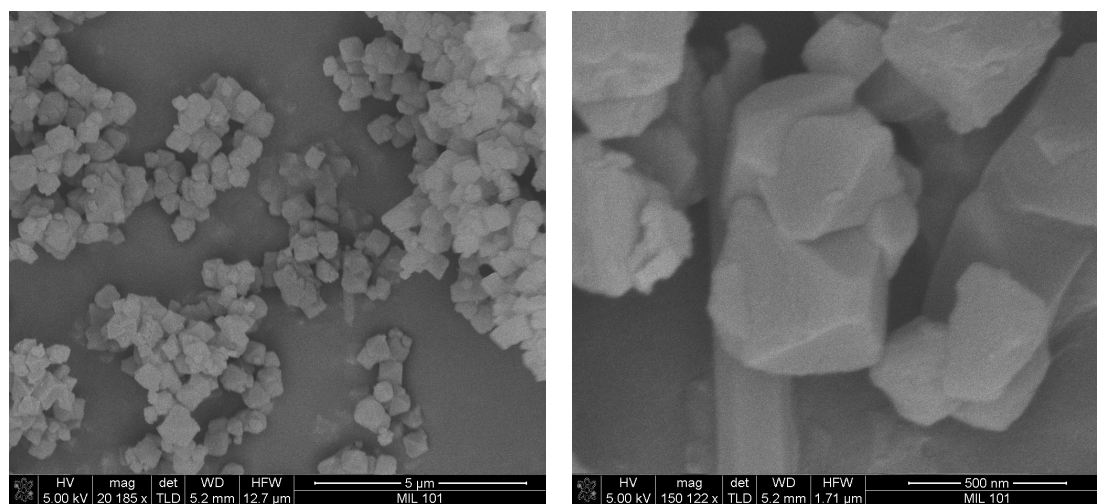


Figure 2.21: SEM images of MIL-101.

MIL-101 filled with metal clusters

In order to investigate the influence of the pore size to hydrogen adsorption the large pores of the framework MIL-101 was filled by $\text{Mo}_6\text{Br}_8\text{F}_6$ clusters [21]. A new intercalation technique was used to introduce the fluorinated inorganic clusters into the MOF material. Therefore the dried MIL-101 framework and the metal clusters were dispersed in a mixture of ethanol and a small amount of aqueous solution of fluorhydric acid. The incorporation was proven by various techniques. X-ray powder diffraction showed that the MIL-101 framework remained intact upon loading. While infrared spectroscopy, thermal gravimetric analysis, and surface area measurements on the loaded MIL-101 yielded strong differences to the unloaded material. The SSA for example decreased from $2761 \text{ m}^2 \text{ g}^{-1}$ to $852 \text{ m}^2 \text{ g}^{-1}$, as the framework structure remained the same as proven by X-ray powder diffraction this indicates that the material became heavier. Elemental analysis finally showed that the MIL-101 framework is having the same composition as the starting MIL-101 and the average loading of the two pores in MIL-101 is 7-8 clusters per pore. By ^{19}F solid state NMR it was shown that also the $\text{Mo}_6\text{Br}_8\text{F}_6$ cluster remain intact upon loading into the framework and that most of the clusters are inside the pores of MIL-101. Figure 2.22 shows schematically the $\text{Mo}_6\text{Br}_8\text{F}_6$ cluster and the pore of MIL-101 without regard to the relative size.

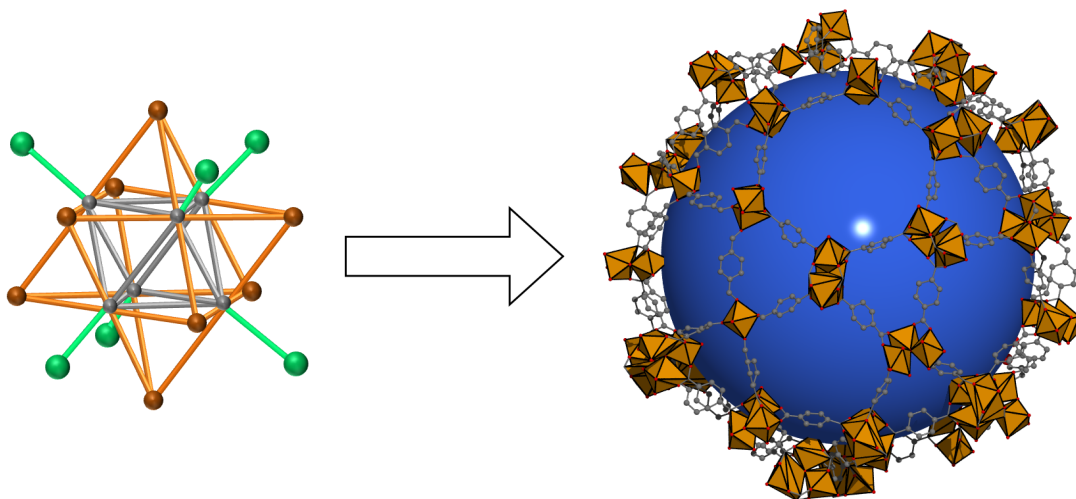


Figure 2.22: Clusters of $\text{Mo}_6\text{Br}_8\text{F}_6$ (left) (Mo: gray, Br: orange, F: green) were intercalated into the pores of MIL-101 (right).

IUPAC class	Material	Pore diameter [Å]	SSA from gas adsorption [m ² g ⁻¹]	Accessible SSA [m ² g ⁻¹]	SPV from gas adsorption [cm ³ g ⁻¹]	Skeletal density from He ads. [g cm ⁻³]
ultra- micro- porous	Mg-formate	3.4	0 (N ₂)			1.47
	MFU-4	3.88, 11.9	0 (N ₂ [12])	1736 (H ₂ [13]) 1611 (N ₂ [12]) 1350 (Ar [13])		1.8
	MFU-4L	12.0, 18.6	2178 (N ₂) 2750 (Ar [13])	3095 (H ₂ [13]) 2987 (Ar [13])	1.02 1.42 [13]	1.61
super- micro- porous	MOF-5	12, 15	2713 (N ₂)	3895 (H ₂ [29]) 3580 (N ₂ [8])	1.15	1.71
	DUT-4	9	fresh: 1308 (N ₂ [15]) old: 601 (N ₂)	2393 (H ₂ [29]) 2213 (Ar [29]) 2090 (N ₂ [29])	fresh 0.68 [15] old 0.41	1.29
	DUT-5	11	fresh: 1613 (N ₂ [15]) old: 1351 (N ₂) old: 1554 (Ar) [39]	2766 (H ₂ [29]) 2581 (Ar [29]) 2479 (N ₂ [29])	fresh 0.81 [15] old 0.56	1.48
	Cu-BTC	5, 9	1499 (Ar [39]) 1527 (N ₂)	2691 (H ₂ [29]) 2449 (Ar [29]) 2268 (N ₂ [29])	0.62	1.70
	MOF-177	11	4728 (N ₂)	4790 (N ₂ [29]) 4722 (H ₂ [29])	1.96	1.37
meso- porous	MIL-101	7, 29, 34	2761 (N ₂)		1.51	1.52
	MIL-101F		852 (N ₂)		0.46	2.08

Table 2.1: Overview of the classification, pore diameter, specific surface area (SSA), specific pore volume (SPV), and skeletal density for the materials investigated.

3 Experimentals, Results and Discussion

3.1 High pressure hydrogen adsorption

3.1.1 Volumetric device for high pressure adsorption

Adsorption of gases is measured volumetrically in a Sievert's type apparatus, PCT-Pro2000 from HyEnergy LLC (Setaram Inc.), equipped with a microdoser for measurements of small amounts of material. Figure 3.1 shows the main components of this apparatus. Helium or hydrogen is connected to the internal supply volume. The supply

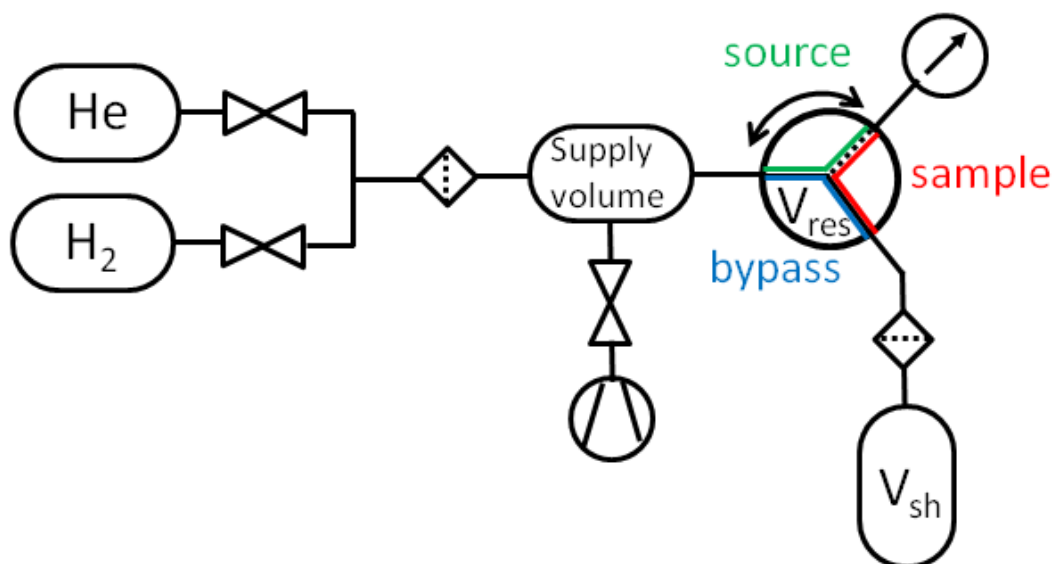


Figure 3.1: Scheme of the PCTPro2000 equipped with a microdoser. The rotating valve enables three connections, bypass, sample, and source, and at the same time, together with the manometer, provides the reservoir volume.

volume is connected to a rotating valve which offers three possible connections. **Source** connects the supply volume directly to a gauge and therefore enables determination of the pressure in the supply volume and connecting lines. **Sample** connects the gauge to the sample holder volume. The third option, **bypass**, connects the sample holder to the supply volume which enables direct loading of the sample holder with gas or evacuation

3 Experimentals, Results and Discussion

by the turbo molecular pump which can be connected to the supply volume. The volumetric measurement technique is based on the expansion of gas from a reservoir volume to a sample holder volume.

To measure adsorption first the sample holder volume, then the skeletal volume of the material and finally the adsorbed amount is determined. To determine the sample holder volume V_{sh} helium at room temperature is used. The sample holder is evacuated and the reservoir is filled with helium at the pressure P_{ini} . The amount of gas present in the reservoir volume n_{total} can be calculated by the corrected ideal gas law 4.1

$$n_{total} = \frac{P_{ini} \cdot V_{res}}{Z \cdot R \cdot T}. \quad (3.1)$$

When the valve is opened, the pressure drops as the gas expands from the reservoir volume to the sample holder volume. As the total amount of gas present n_{total} in the system remains constant, the free volume of the sample holder can be determined by the measured equilibrium pressure P_{eq}

$$V_{sh} = \frac{n_{total} \cdot R \cdot T \cdot Z}{P_{eq}} - V_{res}. \quad (3.2)$$

For determination of the skeletal volume V_{sk} of an adsorbent a non adsorbing gas is used which is typically helium at room temperature. The reservoir is filled with the pressure P_{ini} and the valve to the evacuated sample holder is opened. The sample holder volume is now reduced by the skeletal volume of the adsorbent. Therefore the skeletal volume is calculated from the equilibrium pressure P_{eq} after expansion from the reservoir to the sample holder

$$V_{sk} = V_{res} + V_{sh} - \frac{n_{total} \cdot R \cdot T \cdot Z}{P_{eq}}. \quad (3.3)$$

To measure the amount of adsorbed hydrogen the sample holder with the adsorbent is evacuated and the reservoir is filled with the pressure P_{ini} . When the valve is opened the pressure drops due to expansion into the volume $V_{sh} - V_{sk}$ and adsorption. The amount adsorbed is therefore the difference of the total amount of gas that was loaded in the reservoir n_{total} and the amount of gas which is present in the gas phase at equilibrium n_{gas}

$$n_{ads} = n_{total} - n_{gas} \quad (3.4)$$

$$= \frac{P_{ini} \cdot V_{res}}{Z_{P_{ini}} \cdot R \cdot T} - \frac{P_{eq} \cdot (V_{res} + V_{sh} - V_{sk})}{Z_{P_{eq}} \cdot R \cdot T} \quad (3.5)$$

This yields the excess adsorbed amount. Therefore, to measure adsorption the pressure, volumes and temperature needs to be determined precisely. The reservoir volume of $V_{Res} = 0.51 \text{ cm}^3$ is realized in the microdoser by the volume of the connection pipe in the rotating valve and the volume of the manometer. The sample holder volume is 1.27 cm^3 . The pressure is measured by a pressure gauge which is limited to 6.5 MPa with an accuracy of 1 % of reading. Typically a sample mass in the range of 100-200 mg is used.

As adsorption is caused by the very weak Van der Waals interaction the adsorbed amount of hydrogen at room temperature is typically very low. To increase the amount adsorbed and get a better insight in the processes involved, the sample needs to be cooled to cryogenic temperatures. For the PCTPro2000 two cooling devices are used: a liquid bath cryostat with nitrogen and argon (for 77 K and 87 K) and a cooling system (87 K and above) as schematically shown in figure 3.2. In the liquid bath cryostat the level is kept constant by manual refilling. For temperatures above 87 K a cooling system was developed. The sample holder is surrounded by a copper block with a copper finger sticking

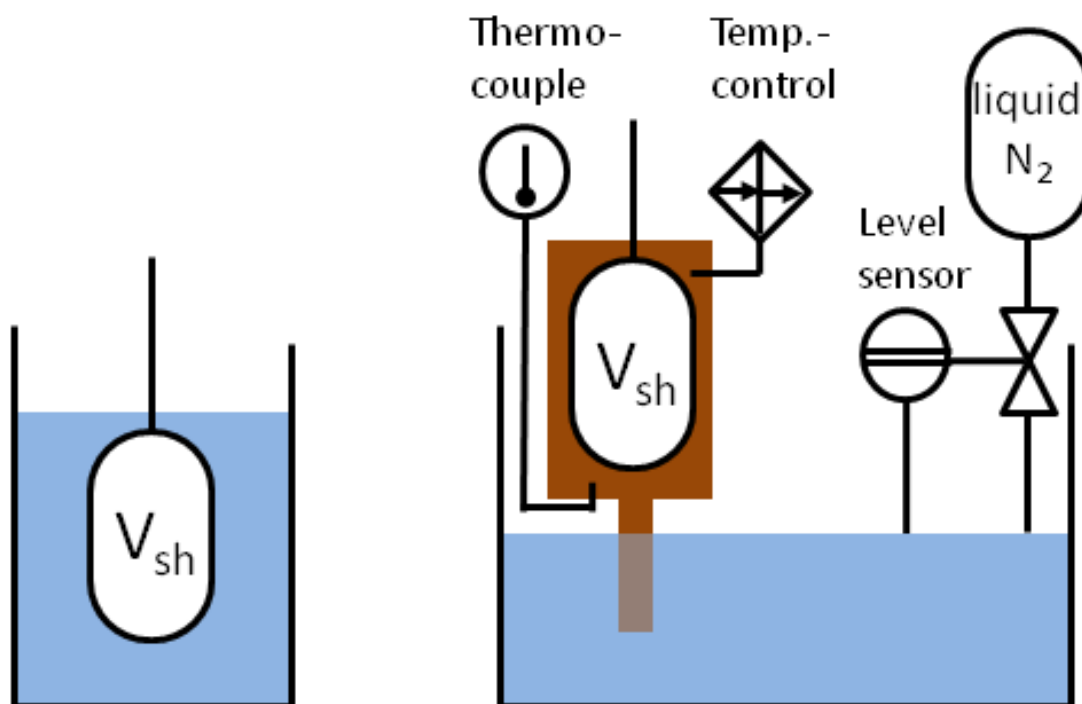


Figure 3.2: Cooling systems for the PCTPro2000 microdoser. Left: bath cryostat for cooling with liquid nitrogen 77 K and liquid argon 87 K. Right: Cooling system for temperatures above 87 K where the sample holder is surrounded by a copper block (brown) and the refill of the liquid gas is controlled automatically.

into a liquid nitrogen bath. The temperature is monitored and controlled by a PID control which heats the copper block with a heater coil which is wrapped around the block. The temperature of the copper block is measured by K-type thermocouples. The level of nitrogen is automatically kept constant within 0.2 cm by a level sensor controlling a supply system for liquid nitrogen.

3.1.2 Calibration

With the microdoser the reservoir volume is extremely small with 0.51 ml. The sample holder volume is calibrated by expansion of helium gas from the reservoir to the sample holder volume with an equilibrium pressure of approximately 0.2 MPa. Different measurements of the volume of the empty sample holder yielded a volume of 1.27 ± 0.02 ml and therefore the uncertainty of the sample holder volume of the PCTPro2000 equipped with the microdoser is approximately 2%. For each material investigated the empty volume in the sample holder is measured four times in adsorption and desorption. From these eight values the average volume is used for the measurement.

In the cooling device three K-type thermocouples in the copper block monitor and control the temperature of the sample holder. They are calibrated in liquid nitrogen and liquid argon. To make sure the sample holder is at 87 K when the temperature control is set to 87 K the measurement is compared to the measurement with the sample holder in a liquid argon bath. With the cooling device the temperature remains constant during the measurement to approximately ± 1 K.

For all measurements below room temperature, a temperature gradient develops between sample and reservoir. To correct for this, the hydrogen expansion in the empty sample holder and of non-adsorbing material (sea sand) is measured at different temperatures and pressure for various volumes of material. This yields the amount of gas which is present in the gas phase only due to expansion considering all temperatures and temperature gradients. The measurements of an adsorbing material are corrected with these values of non-adsorbing material of the same volume.

To test accuracy, three identical measurements of the empty sample holder at room temperature were performed and yielded a hydrogen amount of approximately $18 \mu\text{g}$ of hydrogen at 2 MPa with a maximum deviation between the measurements of $0.74 \mu\text{g}$. In figure 3.3 one of these measurements of the empty sample holder at room temperature is shown and different sources of possible uncertainties are regarded, e.g. temperature variation of 1K between the volume used and the place where the temperature is measured or an uncertainty in the volume determination of 2% for the reservoir and sample holder. Temperature variations of 1K in the reservoir and/or sample holder yield a maximum variation in hydrogen uptake of $20 \mu\text{g}$ up to a pressure of 2 MPa. An under- or overestimation of the volumes of the reservoir or sample holder only by 2% yields an uncertainty of approximately $60 \mu\text{g}$. By figure 3.3 it becomes clear how sensitive volumetric devices are to uncertainties in the volume calibration. The uncertainty of the measurement at room temperature is therefore given by

$$\Delta m_{ads} = 30 \frac{\mu\text{g}}{\text{MPa}} \cdot P + 3\% \cdot m_{ads} \quad (3.6)$$

where the first term accounts to the uncertainty of the empty sample holder and the second term includes the uncertainty correlated to the adsorbed gas n_{ads} . Therefore to distinguish between the adsorbed amount of hydrogen and the uncertainty in the measurement a sample of 100 mg or 50 mg needs to have an uptake of minimum 0.62 mg g^{-1}

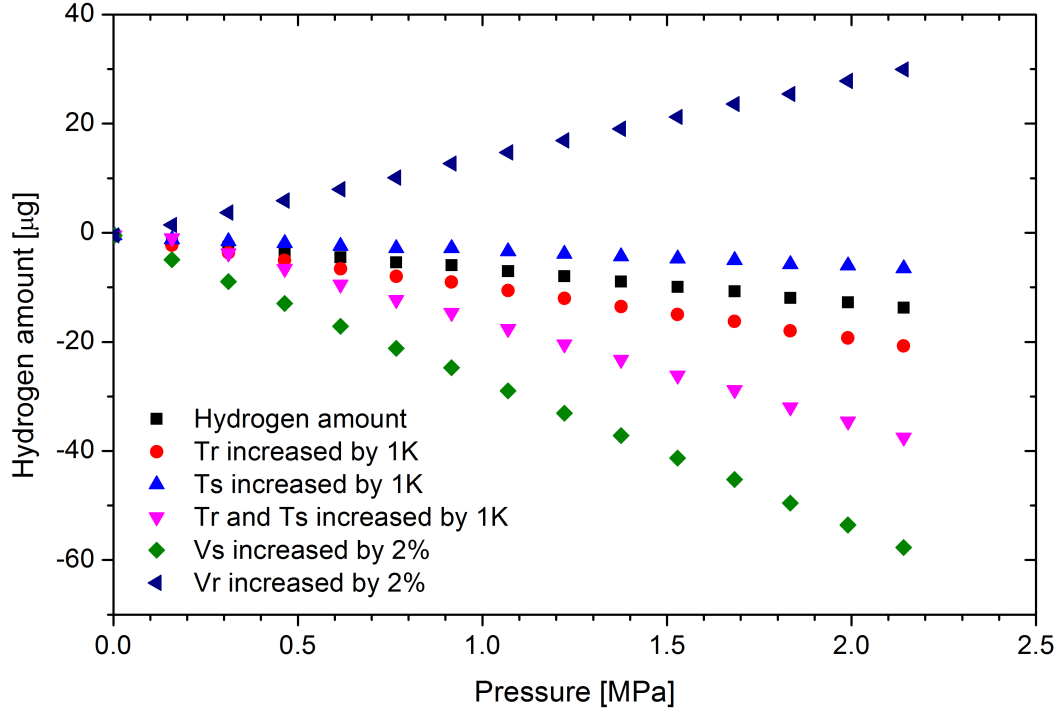


Figure 3.3: Hydrogen amount in an empty sample holder in dependence of the pressure at room temperature assuming different sources of uncertainty.

or 1.24 mg g^{-1} , respectively.

For cryogenic temperatures there are more sources of uncertainties as for example the variations in the level of the coolant and uncertainties in the correction measurements with non-adsorbing material. As an example in figure 3.4 measurements of the empty sample holder are shown which were corrected for influences of temperature and temperature gradients with the calibration used for all measurements. The error bars indicate an error of 2% in the determination of the correction for the temperature gradients. The measurements themselves show a hydrogen amount of $160 \mu\text{g}$ at 2 MPa, including the uncertainty in the correction term even $250 \mu\text{g}$. The uncertainty in the measurement of the empty sample holder at 77 K is therefore approximately $125 \mu\text{g MPa}^{-1}$. Analogue to room temperature the uncertainty in a measurement at 77 K depends additionally on the amount adsorbed and is therefore given by

$$\Delta m_{ads} = 125 \frac{\mu\text{g}}{\text{MPa}} \cdot P + 2,5\% \cdot m_{ads}. \quad (3.7)$$

Therefore to distinguish between adsorption and uncertainty of the measurement, a sample of 100 mg or 50 mg needs to have an uptake of minimum 1.28 mg g^{-1} or 2.56 mg g^{-1} , respectively.

To verify the hydrogen uptakes measured for materials two tests were performed. First,

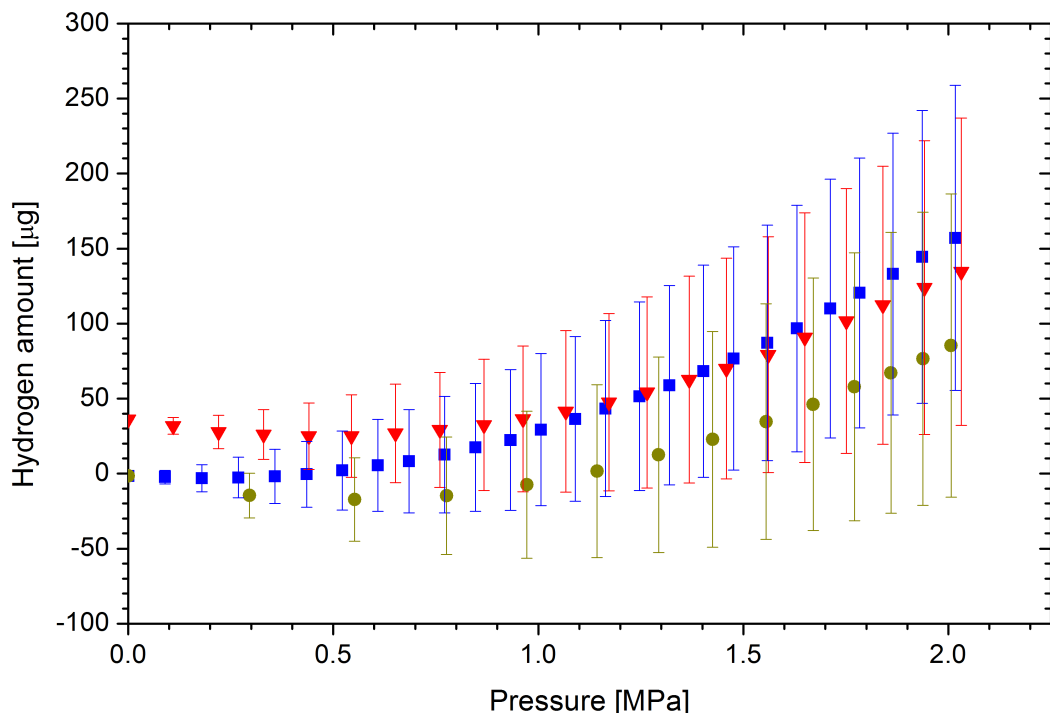


Figure 3.4: Three individual measurements of the amount of hydrogen in an empty sample holder at 77 K in dependence of the pressure. The error bars indicate an uncertainty of 2% in the temperature correction.

different amounts of the same material were measured. If the weight specific hydrogen uptake varies with the mass of the sample it is a clear indication for a leak, an error in the volume calibration or the pressure gauge. In the test, materials with different mass yielded the same weight specific hydrogen uptake within experimental uncertainty. Second, measurements were compared to results from other laboratories. A round robin test within the NESSHY Project was carried out on the activate carbon material, Takeda 4A, under precisely controlled conditions. This is reported by Zlotea et al. [22] where our laboratory is denoted as number 6. The comparison shows that hydrogen uptake at 77 K and room temperature were determined precisely for this material in our laboratory.

Additionally in figure 3.5 the hydrogen uptake measured for MOF-177 at different laboratories at 77 K is shown. There are no measurements given at higher temperature as these are rarely found in literature. Our measurement is indicated by the blue squares which is identical to the results obtained by Poirer et al. [42] (orange triangle). Furukawa et al. [43] measured the hydrogen uptake twice with a volumetric device (yellow and dark yellow) and once with a gravimetric device (green). The hydrogen uptake is slightly below the data from our laboratory and data given by Poirer. Volumetric measurements reported by Wong-Foy et al. [24] (red) yield the same hydrogen uptake as the volumetric

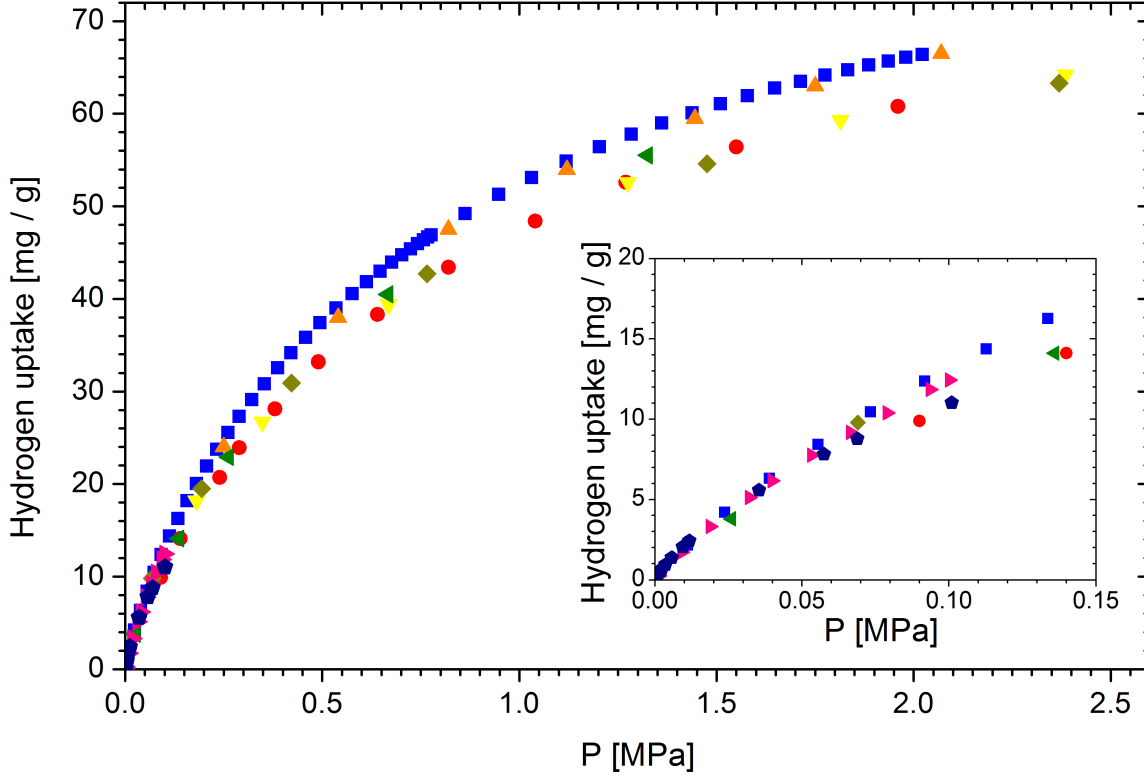


Figure 3.5: Comparison of measurements of excess hydrogen uptake in MOF-177 with results from other laboratories. This work: \square , Poirer et al. [42]; \triangle , Furukawa et al. [43] volumetric: ∇ and \diamond ; gravimetric: \triangleleft , Wong-Foy et al. [24]; \circ , Rowsell et al. [44]; \blacktriangleright and \diamond .

data given by Furukawa. At high pressure of 2 MPa MOF-177 shows a hydrogen uptake of $63 \pm 3 \text{ mg g}^{-1}$ in all laboratories. Additionally low pressure adsorption measurements (pink and dark blue) reported by Rowsell et al. [44] are shown in figure 3.5 in the inset. They indicate that the precision of the device is also very good at low pressure.

3.1.3 Results

Hydrogen adsorption isotherms at 77 K

For ten different metal-organic frameworks, adsorption and desorption isotherms were measured in a fully automated Sievert's device at temperatures of $T = 77 - 298$ K and pressure up to 2.5 MPa. The materials are activated by heating the sample holder for several hours under vacuum in order to remove solvent molecules or any adsorbed molecules. The material mass is in the range of 99 – 361 mg. The adsorbed amount is reported in wt% which is defined as mass of hydrogen m_{ads} per mass of the system, which consists of the sample mass m_S and the adsorbed hydrogen

$$[wt\%] = \frac{m_{ads}}{m_S + m_{ads}} \quad (3.8)$$

An overview of the excess hydrogen uptake at 2 MPa for all materials at 77 K and 298 K can be found in table 3.1.

Ultramicroporous materials

Figure 3.6 and 3.7 show the excess hydrogen uptake of the ultramicroporous metal-organic frameworks MFU-4 and Mg-formate in dependence of the pressure for temperatures between 77 K and room temperature. At 77 K a typical IUPAC type I isotherm

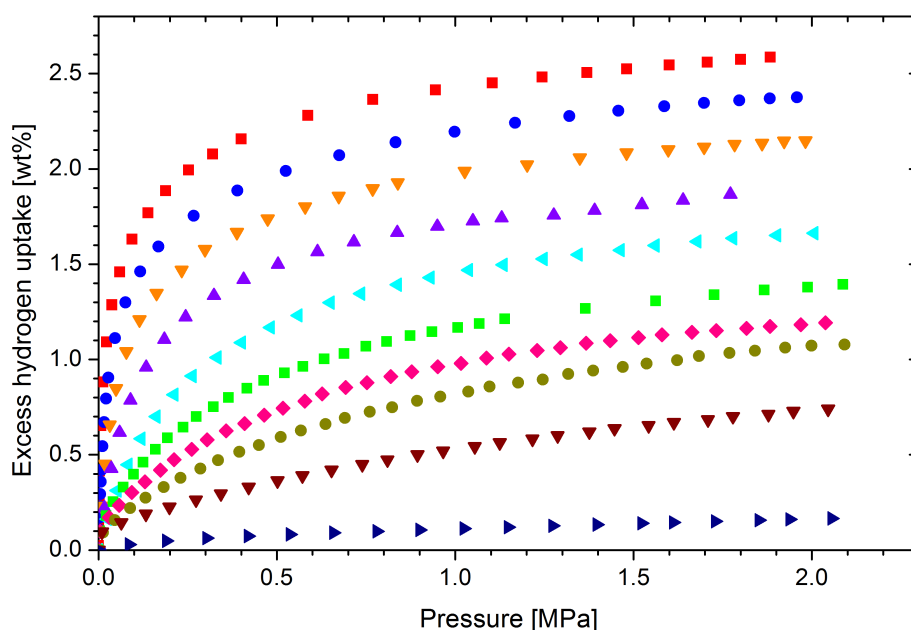


Figure 3.6: Excess hydrogen adsorption (filled symbol) of MFU-4 at \square 77 K (liquid N_2), \circ 87 K (liquid Ar), ∇ 97 K, \triangle 107 K, \triangleleft 117 K, \square 127 K, \diamond 137 K, \circ 147 K, ∇ 177 K, and \triangleright 298 K

with a steep increase at low pressure followed by a saturation plateau at higher pressure is observed for both materials. With increasing temperature the initial increase is less pronounced and saturation is not observed anymore. At room temperature the hydrogen uptake increases linearly with the pressure. The isotherms are reversible for all temperatures and no hysteresis is observed between adsorption and desorption. The isotherms are measured by adding a specific amount of gas to the sample holder and then waiting for equilibrium. When measuring isotherms with many equilibrium points the uncertainty of each point adds up. Therefore all isotherms are measured twice once with small dosing steps which yields many equilibrium points to have high resolution and once with very large doses. The measurements with small and large doses agree well for all measured materials. At 77 K and 2 MPa, MFU-4 shows an excess hydrogen uptake of 2.58 wt% which decreases to 0.17 wt% at room temperature and 2 MPa. The excess hydrogen uptake of Mg-formate is lower with 1.17 wt% at 77 K and 0.05 wt% at room temperature.

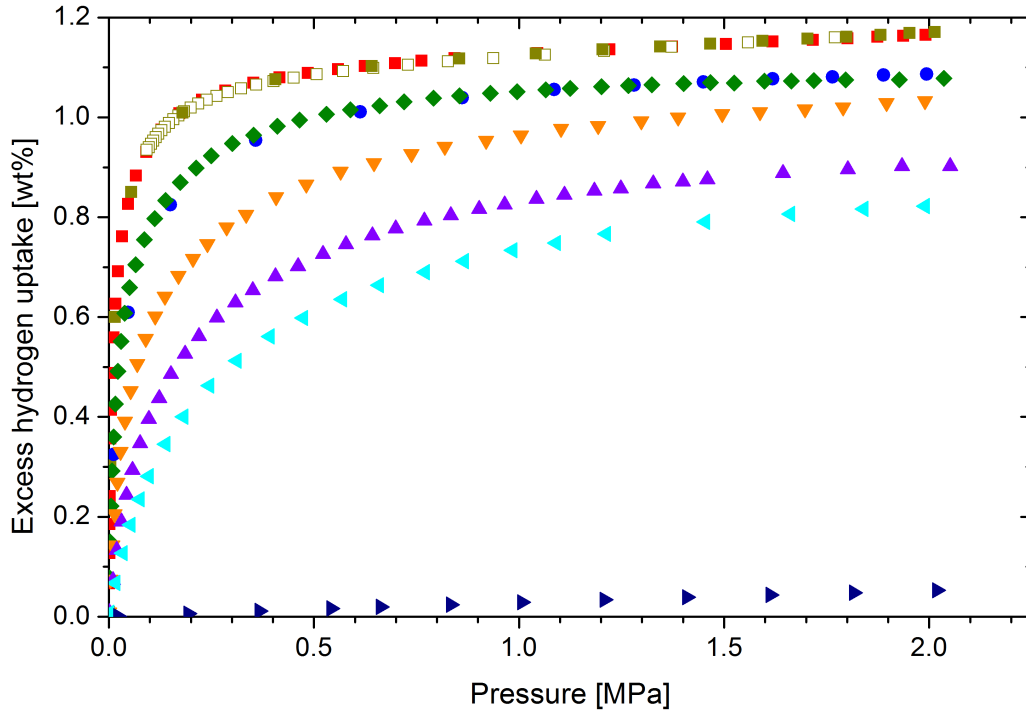


Figure 3.7: Excess hydrogen adsorption (filled symbol) and desorption (open symbol) of Mg-formate at \square \square 77 K (liquid N_2), \circ 87 K (liquid Ar), \diamond 87 K, ∇ 97 K, \triangle 107 K, \triangleleft 117 K, and \triangleright 298 K

Supermicroporous materials

Figure 3.8 - 3.13 shows the excess hydrogen uptake for the supermicroporous materials, MFU-4L, MOF-5, DUT-4f, DUT-5f, Cu-BTC, and MOF-177.

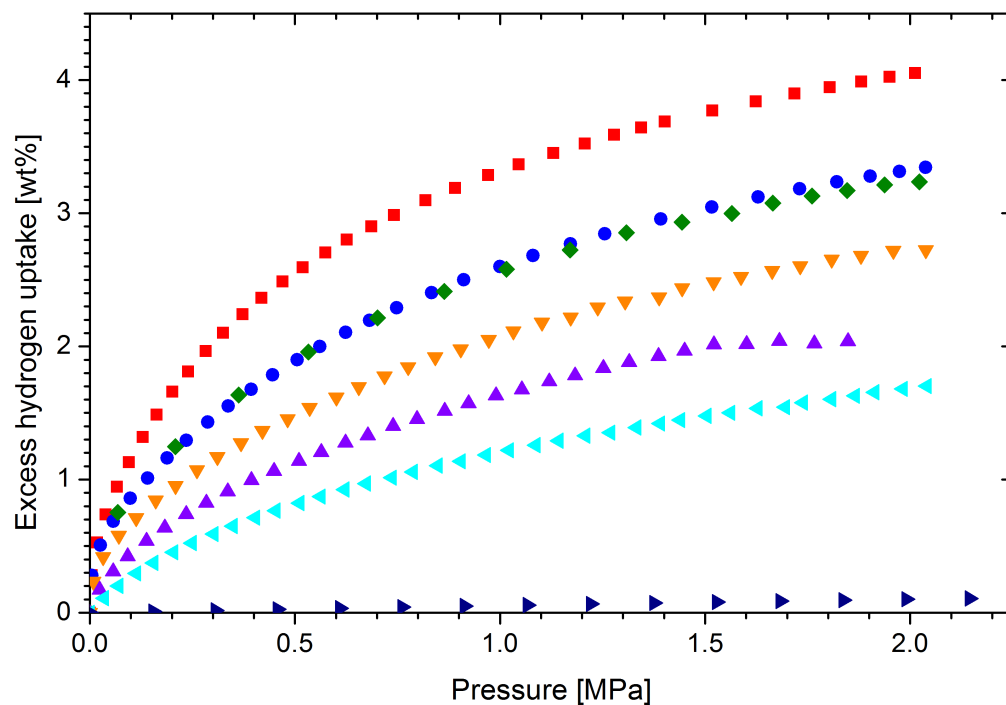


Figure 3.8: Excess hydrogen adsorption of MFU-4L at \square 77 K (liquid N_2), \circ 87 K (liquid Ar), \diamond 87 K, ∇ 97 K, \triangle 107 K, \triangleleft 117 K, and \triangleright 298 K

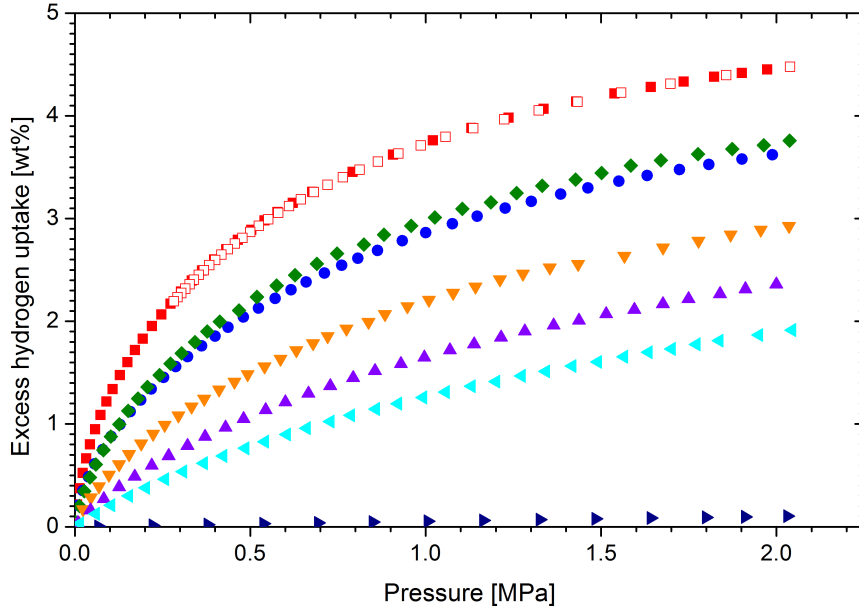


Figure 3.9: Excess hydrogen adsorption (filled symbol) and desorption (open symbol) of MOF-5 at \square 77 K (liquid N₂), \circ 87 K (liquid Ar), \diamond 87 K, ∇ 97 K, \triangle 107 K, \triangleleft 117 K, and \triangleright 298 K

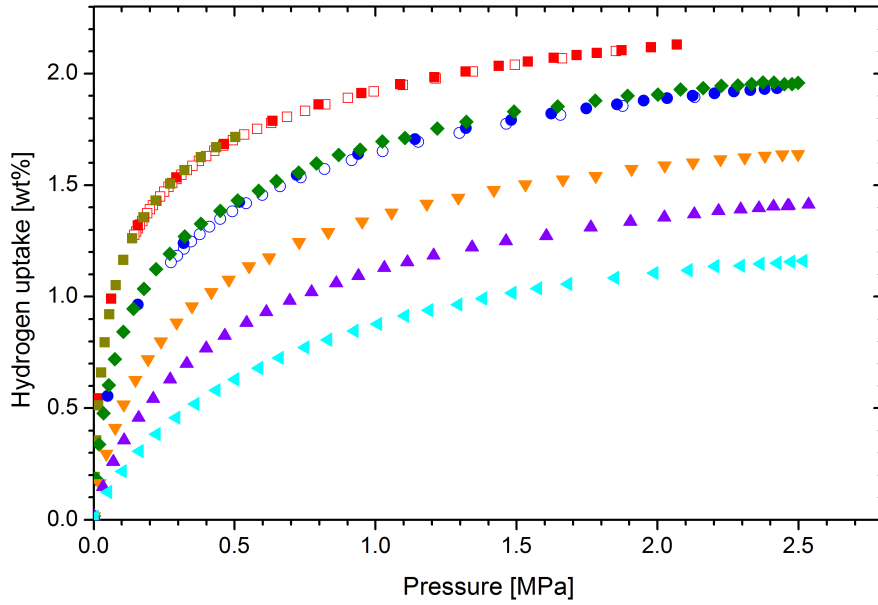


Figure 3.10: Hydrogen uptake of DUT-4f at \square 77 K (liquid N₂), \circ 87 K (liquid Ar), \diamond 87 K, ∇ 97 K, \triangle 107 K, and \triangleleft 117 K. [45]

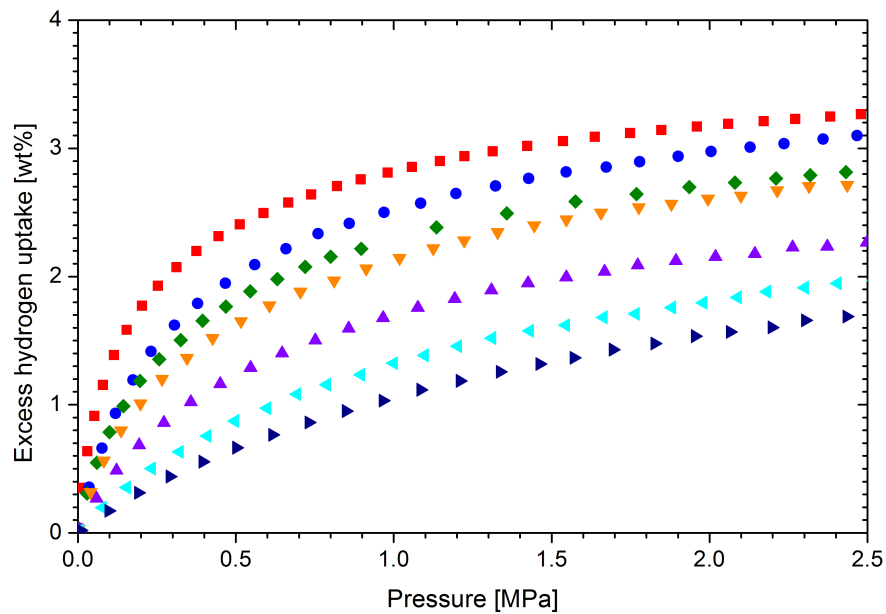


Figure 3.11: Excess hydrogen adsorption of DUT-5f at \square 77 K (liquid N_2), \circ 83 K, \diamond 87 K (liquid Ar), ∇ 91 K, \triangle 100 K, \triangleleft 111 K, and \triangleright 125 K. [45]

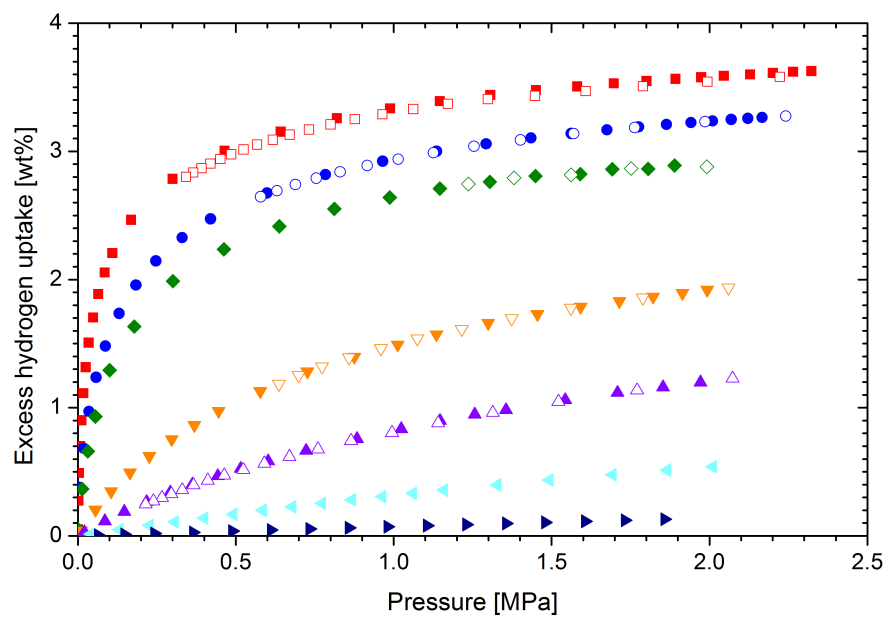


Figure 3.12: Excess hydrogen adsorption of Cu-BTC at \square 77 K (liquid N_2), \circ 87 K (liquid Ar), \diamond 93 K, ∇ 128 K, \triangle 158 K, \triangleleft 218 K, and \triangleright 298 K.

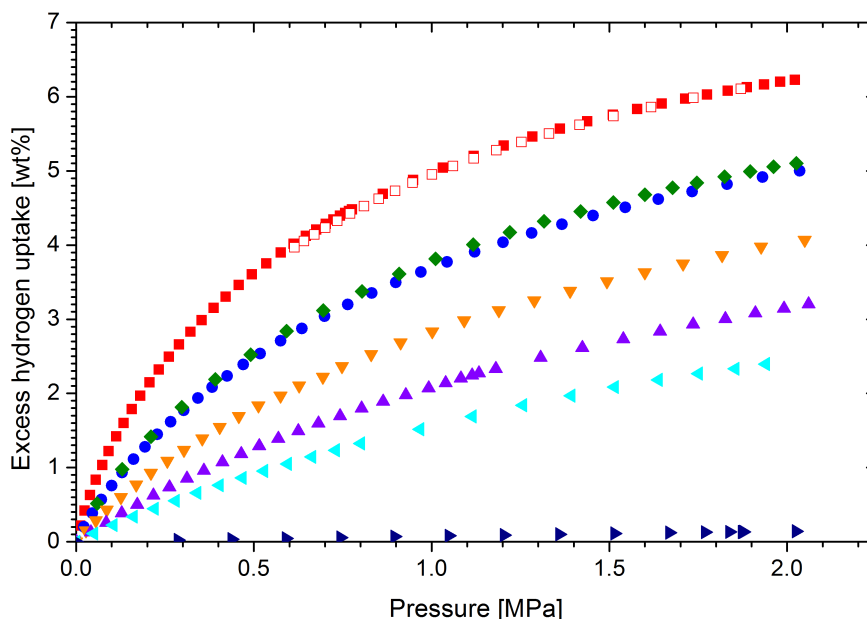


Figure 3.13: Excess hydrogen adsorption (filled symbol) and desorption (open symbol) of MOF-177 at \square 77 K (liquid N_2), \circ 87 K (liquid Ar), \diamond 87 K, \triangle 97 K, \triangle 107 K, \triangleleft 117 K, and \triangleright 298 K.

Compared to the ultramicroporous materials the type I behavior is less pronounced and the isotherms are not reaching saturation up to 2 MPa, but their maximum hydrogen uptake at 77 K and 2 MPa is with up to 6.23 wt% higher than for ultramicroporous materials.

Mesoporous materials

Hydrogen excess adsorption for the mesoporous material MIL-101 with empty pores and filled with metal clusters is shown in figure 3.14 and 3.15. Their shape and hydrogen uptakes at 77 K and room temperature are very similar to the supermicroporous materials. MIL-101 shows a hydrogen uptake of 4.62 wt% at 77 K and 2 MPa which decreases strongly with increasing temperature. Saturation is not reached under these conditions. At room temperature the hydrogen uptake at 2 MPa is only 0.1 wt%. Furthermore in the pores of the mesoporous MIL-101 $Mo_6Br_8F_6$ clusters were incorporated to form MIL-101F. The hydrogen uptake of MIL-101F is lower than for MIL-101 with 1.7 wt% at 77 K and 2 MPa but the shape of the isotherms of the two materials are similar and MIL-101F does also not reach saturation under these conditions. At room temperature the hydrogen uptake of MIL-101F is only 0.05 wt%. Furthermore in the pores of the mesoporous MIL-101 $Mo_6Br_8F_6$ clusters were incorporated to form MIL-101F. The hydrogen uptake of MIL-101F is lower than for MIL-101 with 1.7 wt% at 77 K and 2 MPa but the shape of the isotherms of the two materials are similar and MIL-101F does also not reach saturation under these conditions. At room temperature the hydrogen uptake of MIL-101F is only 0.05 wt%.

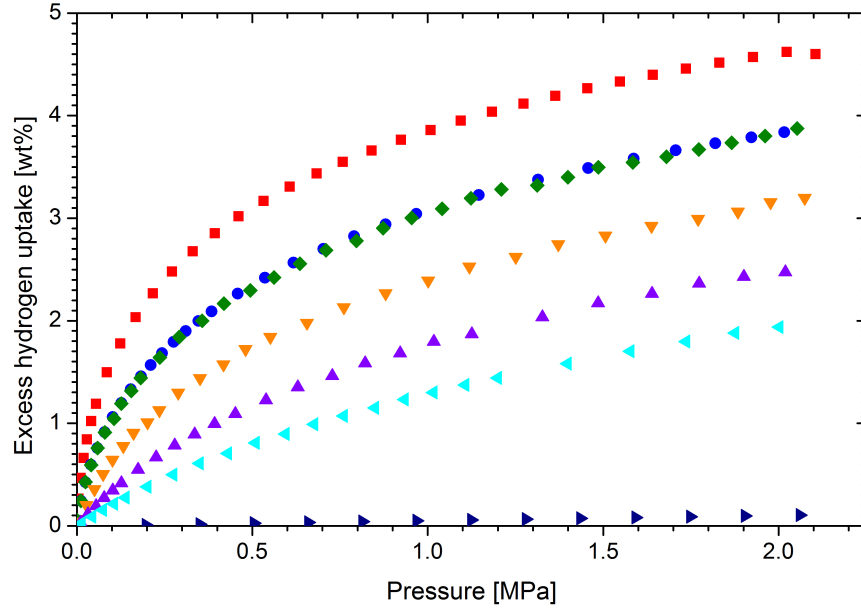


Figure 3.14: Excess hydrogen adsorption of MIL-101 at \square 77 K (liquid N_2), \circ 87 K (liquid Ar), \diamond 87 K, \triangledown 97 K, \triangle 112 K, \triangleleft 127 K, and \triangleright 298 K.

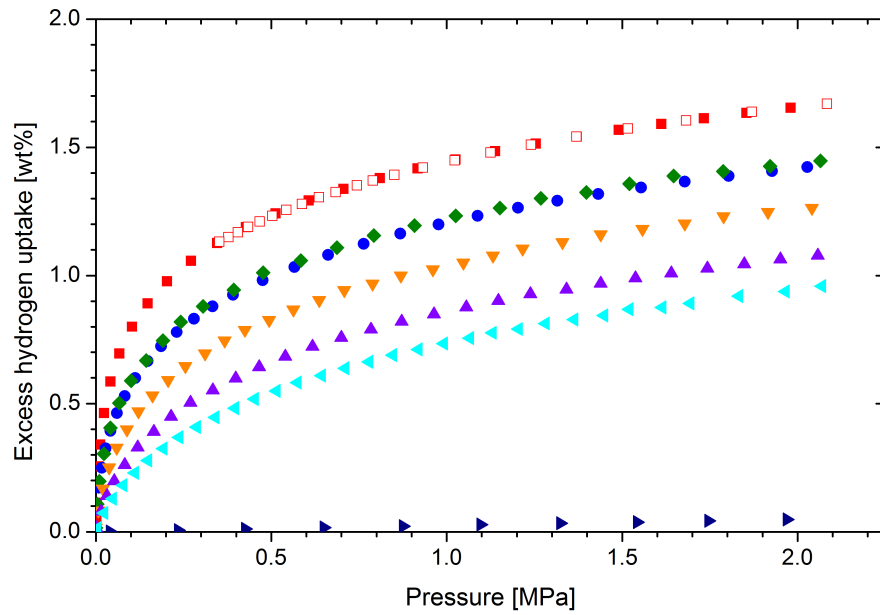


Figure 3.15: Excess hydrogen adsorption of MIL-101F at \square 77 K (liquid N_2), \circ 87 K (liquid Ar), \diamond 86 K, \triangledown 96 K, \triangle 106 K, \triangleleft 116 K, and \triangleright 298 K.

IUPAC classification	Material	Hydrogen adsorbed at 77 K and 2 MPa	Hydrogen adsorbed at 298 K and 2 MPa
ultra-microporous	Mg-formate	1.17 wt%	0.05 wt%
	MFU-4	2.58 wt%	0.17 wt%
super-microporous	MFU-4L	4.02 wt%	0.10 wt%
	MOF-5	4.48 wt%	0.10 wt%
	DUT-4f	2.13 wt%	not measured
	DUT-5f	3.19 wt%	not measured
	Cu-BTC	3.69 wt%	0.14 wt%
	MOF-177	6.23 wt%	0.14 wt%
meso-porous	MIL-101	4.62 wt%	0.10 wt%
	MIL-101F	1.67 wt%	0.05 wt%

Table 3.1: Excess hydrogen uptake of metal-organic frameworks at 77 K and 298 K and a pressure of 2 MPa

Isosteric heat of adsorption

From the excess adsorption isotherms the absolute adsorbed hydrogen is calculated which represents the amount adsorbed on the material (see section 2.1.2). Using the Clausius-Clapeyron equation the isosteric enthalpy of adsorption is calculated from the adsorption isotherms. The pressure which is needed to reach a certain uptake for different temperatures is plotted versus the reciprocal temperature. In this method experimental uncertainties have the strongest influence in either extremely steep or flat regions of the isotherm. Therefore only data from isotherm regions with an intermediate slope are used for this Van't Hoff plot. The slope of a linear fit of pressure points of same uptake is proportional to the isosteric heat of adsorption. Isotherms removed from or added to the Van't Hoff plot result in steps in the isosteric heat of adsorption spectra which therefore represent the experimental uncertainty.

In figure 3.16 the isosteric enthalpy of adsorption is shown in dependence of the surface coverage, which is the hydrogen uptake normalized to the uptake at 2 MPa and 77 K. For all materials investigated the isosteric enthalpy of adsorption ranges between 3.5 kJ mol^{-1} and 7.4 kJ mol^{-1} . The ultramicroporous materials, Mg-Formate and MFU-4, have the highest enthalpy of adsorption with average 6.8 kJ mol^{-1} up to a surface coverage of 70 %. Both enthalpies can be regarded as constant within the experimental uncertainty which is approximately 0.5 kJ mol^{-1} . For some MOFs, like MIL-101, MIL-101F, Cu-BTC, MFU-4L, and MOF-5, the isosteric heat of adsorption decreases strongly with increasing surface coverage, while others, like MFU-4, Mg-Formate, MOF-177, and DUT-5f, remain constant. The lowest enthalpy of adsorption shows MOF-177 with average 3.8 kJ mol^{-1} .

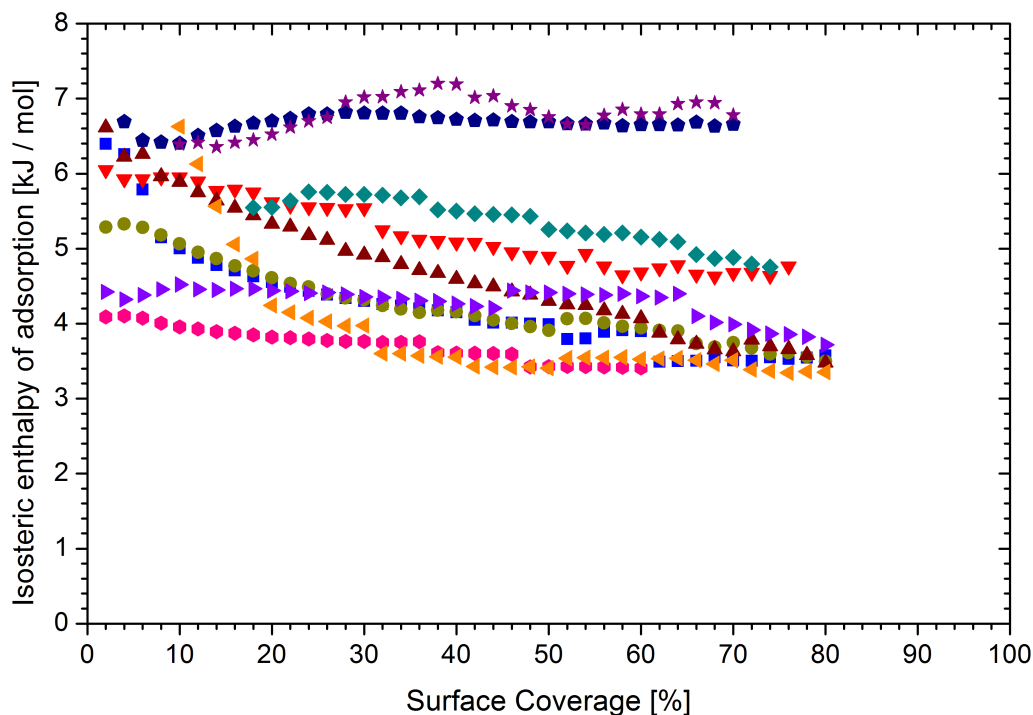


Figure 3.16: Isosteric heat of adsorption for \square MOF-5, \circ MIL-101, \triangle MIL-101F, ∇ Cu-BTC, \diamond DUT-4f, \triangleright DUT-5f, \circ MOF-177, \diamond Mg-formate, \star MFU-4, and \triangleleft MFU4L

3.1.4 Discussion

Surface area

Hydrogen molecules at 77 K, which is well above the critical temperature of 33 K for hydrogen, adsorb on surfaces but are not able to adsorb on one another. Therefore adsorption only occurs in a so-called monolayer on surfaces. An upper limit of the amount adsorbed by any surface is therefore the amount of hydrogen which is contained in a monolayer of liquid hydrogen on the same surface area. Liquid hydrogen at 20 K has a density of $28.35 \text{ cm}^3 \text{ mol}^{-1}$ at 0.1 MPa. Assuming a hexagonal closest packing of the bulk liquid yields a cross-sectional area of 14.2 \AA^2 for one hydrogen molecule. Therefore a monolayer of liquid hydrogen on 1000 m^2 contains 23.57 mg hydrogen.

In figure 3.17 the maximum absolute hydrogen adsorption of the materials investigated is shown in dependence of the specific surface area determined by nitrogen adsorption at 77 K. Mg-formate and MFU-4 do not adsorb any nitrogen at 77 K and therefore the SSA could not be determined and is not shown in figure 3.17. For some of the materials saturation is not observed up to 2 MPa. Therefore the maximum absolute adsorption does not represent the saturation uptake. The dashed line presents the amount of hydrogen assuming a full monolayer coverage of the surface with the density of liquid hydrogen at 20 K.

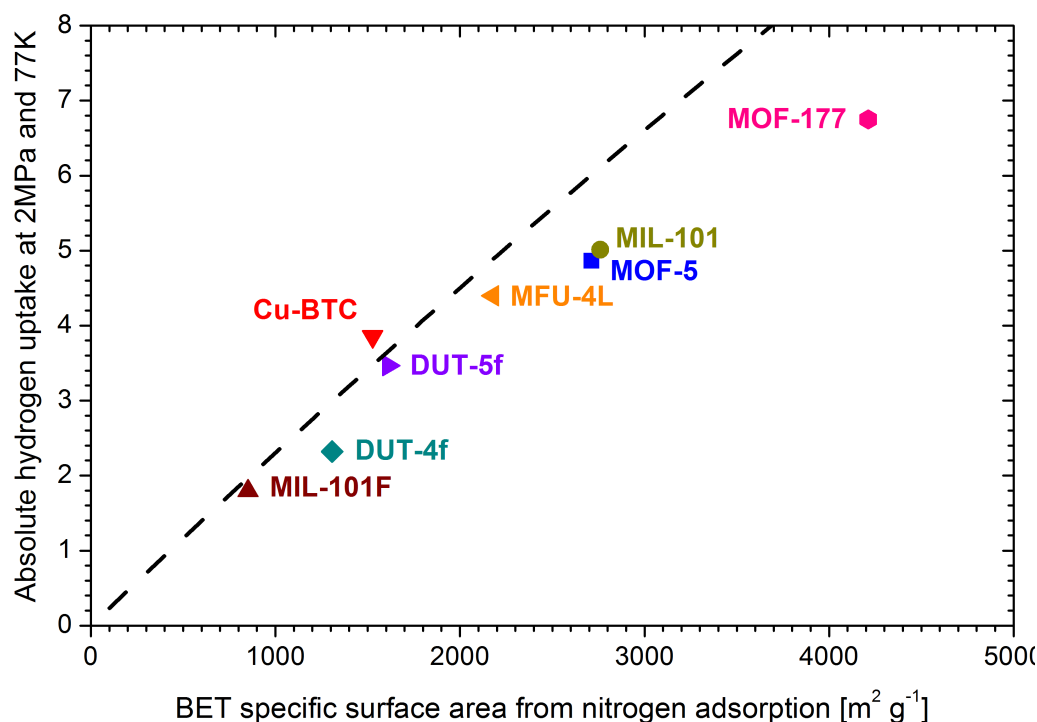


Figure 3.17: Absolute hydrogen uptake of different MOFs at 77 K and 2 MPa correlated to their BET specific surface area.

The hydrogen uptake of most materials investigated lie close to this line. Materials with large SSAs, e.g. MOF-5, MIL-101, and MOF-177, show remarkably less hydrogen uptake as liquid hydrogen in a monolayer. Taking a look at the adsorption isotherms at 77 K of MOF-5 (fig. 3.9), MOF-177 (fig. 3.13), and MIL-101 (fig. 3.14) exhibits that especially these materials have not reached saturation at 2 MPa and therefore their maximum hydrogen uptake will be higher than shown in figure 3.17. Therefore the surface area of these materials is not completely covered.

The calculation of absolute uptake requires assumptions about the density and volume of the adsorbed layer and therefore, it is more convenient to use excess hydrogen uptakes, which are directly measured, for comparison with other laboratories. In figure 3.18 saturation excess hydrogen adsorption uptakes are correlated to the SSA of materials from different classes as MOFs [46, 47], carbons [48, 49], Zeolites [50] and Prussian Blue [51]. All materials follow the same trend of approximately 1 wt% hydrogen uptake per 500 m² which is known as Chahine's rule [52]. The linear correlation of SSA to saturation excess hydrogen uptake for MOFs was shown before experimentally, e.g. by Panella et al. [23] and simultaneously by Wong-Foy et al. [24], and theoretically, e.g. by Frost et al. [25]. Therefore the maximum hydrogen uptake of metal-organic frameworks depends on the SSA available for adsorption.

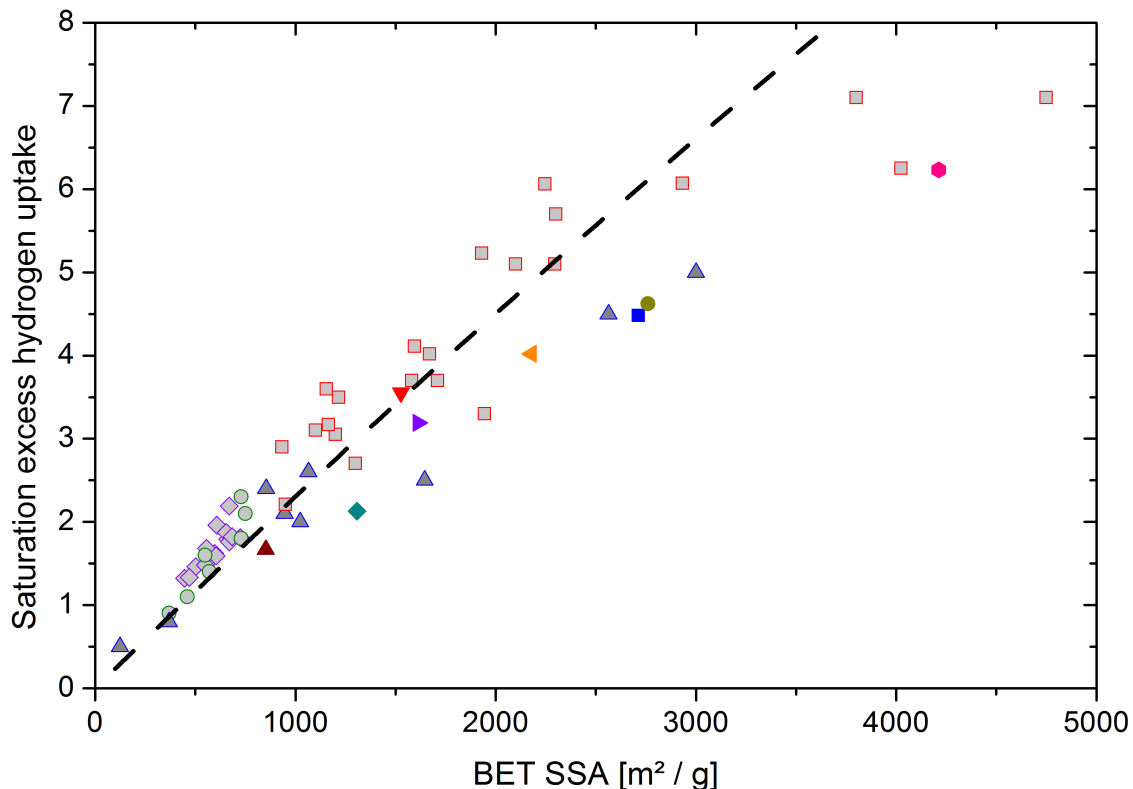


Figure 3.18: Literature data of saturation excess hydrogen uptake for porous materials at 77 K \square MOFs, \circ Prussian blue, \diamond Zeolites, \triangle carbons, and investigated materials from this work at 2 MPa: \square MOF-5, \circ MIL-101, \triangle MIL-101F, ∇ Cu-BTC, \diamond DUT-4f, \triangle DUT-5f, \circ MOF-177, and \triangleleft MFU4L.

Chemical composition

Metal-organic frameworks are built from organic ligands connected by inorganic metal clusters. The ligands are mainly based on carbon which interacts with hydrogen only by weak van der Waals interaction as described in section 3.1.4. But metal clusters offer stronger mechanism for interaction besides van der Waals, e.g. electrostatic interaction, as summarized in the review of Dinca and Long [26]. Investigating hydrogen adsorption sites in MOFs often yields that the strongest adsorption sites are in close proximity of the metal cluster which offers the strongest adsorption potential. E.g. Spencer et al. [53] and Yildirim and Hartman [54] identified by neutron diffraction the strongest adsorption site in MOF-5 close to the zinc complex. Similar results are obtained infrared spectroscopy and ab initio calculations by Bordiga et al. [55]. This was also supported by theoretical calculations e.g. by Klotzas et al [56] and Sillar et al. [57].

Especially if the metal sites are unsaturated the binding strength in the surrounding of the metal cluster can strongly increase. This was experimentally e.g. shown for MOFs containing Cu^{2+} [58, 59, 60], Mn^{2+} [61], and Ni^{2+} [62, 63]. Comparison of different MOF

also indicate that the metal sites do have a strong influence on the hydrogen storage properties [64, 65, 66]. Adsorption sites at the unsaturated metal clusters have isosteric enthalpies of adsorption of up to 13.5 kJ mol^{-1} [63]. But in all cases the strong adsorption sites at the metal cluster present only very few of the overall available adsorption sites. Therefore the enthalpy of adsorption decreases strongly after adsorption of the first hydrogen molecules since these sites are saturated.

In the isosteric enthalpy of adsorption spectra (figure 3.16) influence of the metal cluster is observed only below 20 % surface coverage. At higher coverage the isosteric enthalpies of adsorption are below 6 kJ mol^{-1} for most frameworks.

Therefore it is in general a promising way to increase the interaction strength of hydrogen with a MOF by introducing unsaturated metal sites, but for technical application it is important to analyze the enthalpy of adsorption over the whole range of hydrogen adsorption until saturation is reached [16].

Pore size

Adsorption is due to van der Waals interaction between the atoms of the adsorbent and the molecule adsorbed. On a flat surface adsorption is dominated by the interaction between one surface atom and the gas molecule. If the surface of the adsorbent exhibits some curvature the distance between the adsorbed molecule and the neighboring surface atoms is decreasing. Therefore the overlap of the van der Waals potentials increases and the interaction of the adsorbent to the adsorbate increases. This is schematically shown for two dimensions in figure 3.19 where for each surface atom an identical 12-6 Lennard-Jones potential is assumed. The atoms of the adsorbent are presented by the white spheres in different geometries. The qualitative adsorption potential is indicated by the colored areas. Grey indicates repulsion, red weak adsorption which is getting stronger with yellow, green and blue, respectively. In the upper left picture a flat surface is shown where the adsorption potential is homogeneous over the surface available. In the upper right picture, a corner of two flat surfaces along the x- and y-axis is shown. The van der Waals potential is almost doubled in the corner where the two surfaces meet, as the potentials of the surrounding wall atoms overlap strongly. In the lower left figure a spherical surface is assumed. The interaction potential is increased compared to the flat surface. With decreasing diameter of the sphere, the interaction potential is increasing strongly as shown by the small pore in the lower right picture. In the small sphere the adsorption potential is four times larger than for the flat surface.

This simple theoretical calculation indicates that the isosteric enthalpy of adsorption depends on the framework geometry. From the experimental data this is observed in the isosteric enthalpies of adsorption determined by the adsorption isotherms. The two ultramicroporous materials investigated, Mg-formate and MFU-4 show the highest enthalpy of adsorption of approximately 6.8 kJ mol^{-1} up to a surface coverage of 70 %. The two supermicroporous MOFs DUT-4f and DUT-5f have a lower enthalpy of adsorption. They have the same topology as the metal cluster is identical and only the length of the linker is different. DUT-4f and DUT-5f exhibit channels with a diameter of 9 Å and 11 Å, respectively. This is reflected in the isosteric heat of adsorption which is approxi-

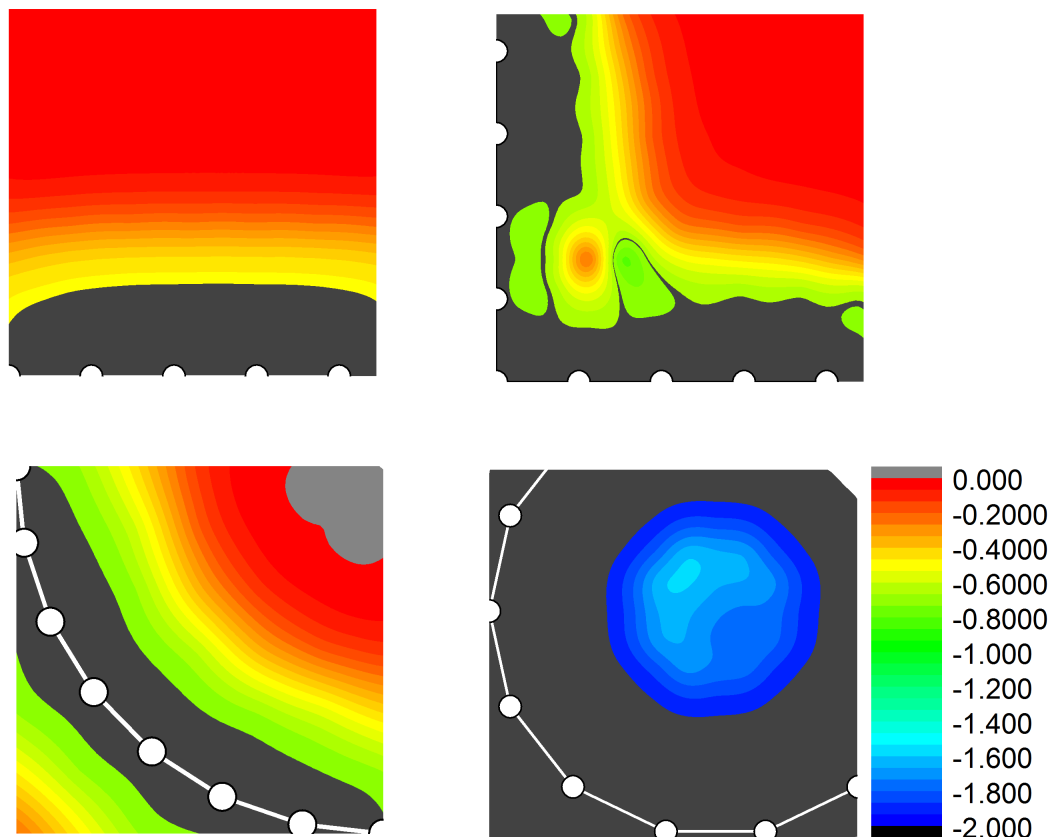


Figure 3.19: Sketch of adsorption potentials for different constellations of surface atoms (white spheres). The effective potentials is increasing strongly with the curvature of the pore wall even though the potential of the single surface atom remains constant.

mately 1.5 kJ mol^{-1} higher for DUT-4f than for DUT-5f. Another pair of MOFs that is isostructural with the only variation in the length of the linker is the ultramicroporous MFU-4 and the supermicroporous MFU-4L. While the isosteric enthalpy of adsorption for the supermicroporous material is almost constant at 6.8 kJ mol^{-1} a strong decrease is observed for the MFU-4L. The isosteric enthalpy of adsorption starts at similar values as for MFU-4 with approximately 6.8 kJ mol^{-1} and decreases strongly before a surface coverage of 20 % is reached. Up to 40 % surface coverage the enthalpy decreases slowly to 3.6 kJ mol^{-1} where it remains constant up to 80 % surface coverage. Above 20 % surface coverage the difference in the enthalpy of adsorption can be explained by the increased pore size which is 3.9 \AA and 12 \AA in MFU-4 compared to 12 \AA and 19 \AA in MFU-4L. But the enthalpy below 20 % surface coverage indicates that the pore size is not the only parameter that needs to be regarded. In both compounds an exposed chlorine atom sticks into the small pore. It was shown before (section 3.1.4) that metal centers can offer strong adsorption sites. Assuming each chlorine atom in MFU-4L interacts with one or

two hydrogen molecules, this would correspond to a surface coverage of 15 % (0.6 wt%) or 30 % (1.2 wt%). This assumption agrees with the range of increased adsorption enthalpy for MFU-4L.

In the following the observed isosteric enthalpy will be analyzed with respect to the diameter of the available pores.

The ultramicroporous framework Mg-formate has channels that vary in their diameter between 3.4 Å and 4.6 Å. The average isosteric enthalpy is 6.7 kJ mol⁻¹.

The supermicroporous materials have lower enthalpies of adsorption than the ultramicroporous materials. As an example, in figure 3.20 the isosteric enthalpy of adsorption is shown for MOF-5. At low surface coverage the enthalpy is 6.4 kJ mol⁻¹ and decreasing to approximately 5 kJ mol⁻¹ below 10 % surface coverage. This strong interaction can

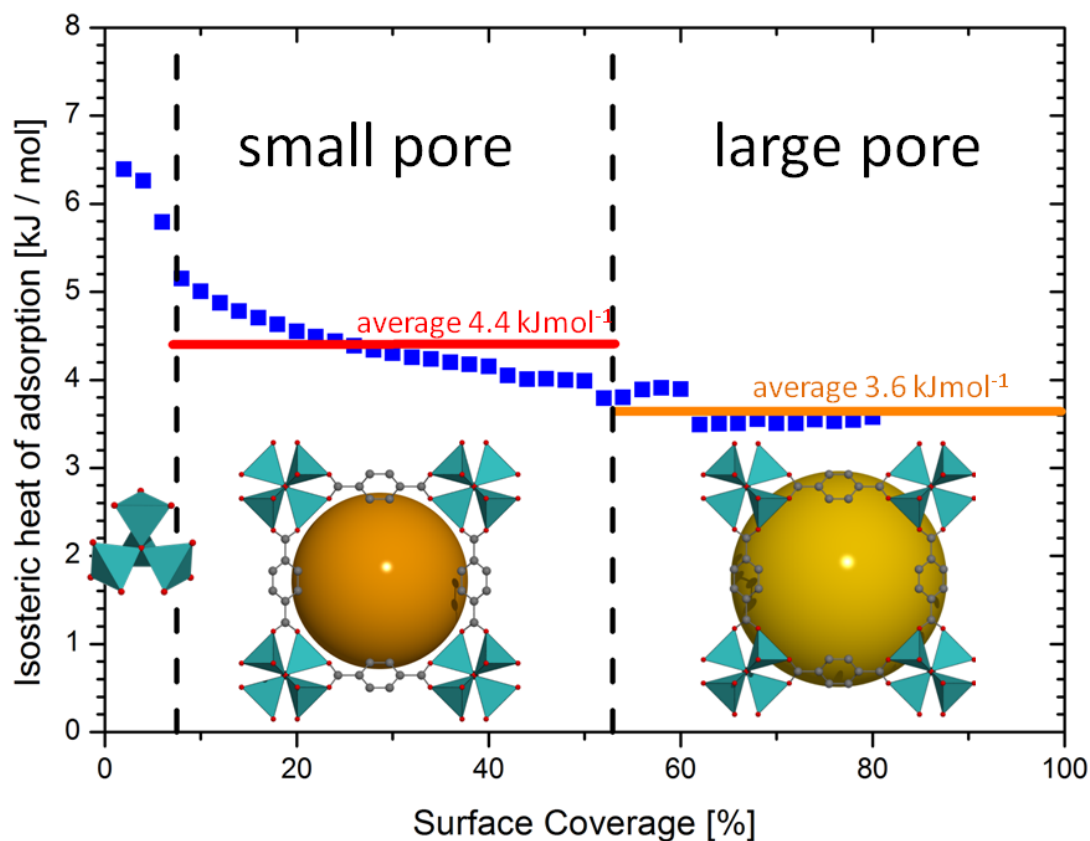


Figure 3.20: The isosteric enthalpy of adsorption of hydrogen in MOF-5 is assigned to the metal centers at low loadings followed by hydrogen adsorption in the small and large pore.

be assigned to strong adsorption sites at the metal cluster as for example pointed out by Sillar et al. [57]. MOF-5 has alternating pores with a inner free diameter of 12 Å and 15 Å, but owing to the framework structure the volume of both pores is the same. Assuming half of the hydrogen adsorbed at 77 K above saturation of the strong site in

the small pore and the rest in the large pore, the average value of the isosteric enthalpy of adsorption below 54 % surface coverage which is 4.4 kJ mol^{-1} is assigned to adsorption in the small 12 \AA pore and above 54 % surface coverage which is 3.6 kJ mol^{-1} to the large 15 \AA pore.

For the supermicroporous MFU-4L the hydrogen adsorption isotherm does not reach saturation at 77 K and 2 MPa. Therefore it cannot be determined if hydrogen is adsorbed only in the small pores or also in the large pores and the isosteric enthalpy of adsorption of 3.5 kJ mol^{-1} which remains constant from 30 – 80 % surface coverage is assigned to both pore diameters.

For the supermicroporous frameworks DUT-4 and DUT-5 only channels of 9 \AA and 11 \AA , respectively, are available. The average value of the observed isosteric enthalpy of adsorption is 4.3 kJ mol^{-1} and 5.4 kJ mol^{-1} .

Cu-BTC has a pore system of 9 \AA pores and the same number of small side pockets with an inner free diameter of 5 \AA . As hydrogen can pass through the framework without penetrating the small side pockets, it is categorized to be supermicroporous even though the small side pockets are ultramicropores. Assuming spheres, the surface area ratio of the small pore to the larger pore is approximately 0.3. The range of surface coverage up to 30 % has an average isosteric enthalpy of adsorption of 5.76 kJ mol^{-1} which is assigned to the small side pocket. At higher surface coverage the average value of the enthalpy of adsorption is 4.9 kJ mol^{-1} .

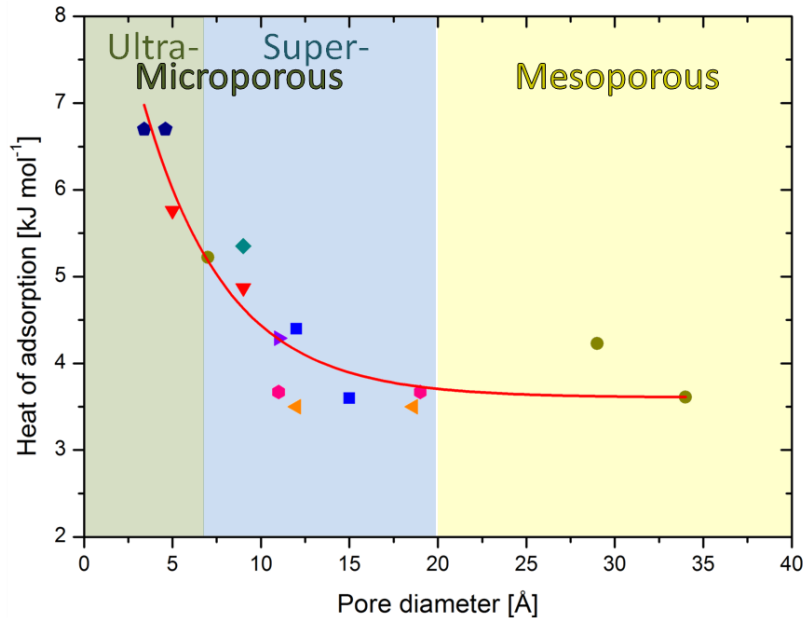
MOF-177 has larger ellipsoidal pores with a short axis of 11 \AA and a large axis of 19 \AA . As the overlap of the van der Waals potentials depends on the curvature and distance to the opposite wall, neither the small nor the large axis characterizes the pore properly and therefore both are given in the following. The isosteric enthalpy of adsorption is almost constant over the range of surface coverage investigated with 3.7 kJ mol^{-1} .

The mesoporous MIL-101 consists of small tetrahedral building units which have an inner free diameter of 7 \AA . These building units form two types of large mesopores with an inner diameter of 29 \AA and 34 \AA . The ratio these pores is 17:2:1, respectively, which results in a ratio of their surface areas of approximately 2:4:3. Hydrogen below a surface coverage of 11 % is adsorbed in the small tetrahedral shaped side pocket with an average value of the isosteric enthalpy of adsorption of 5.2 kJ mol^{-1} . Assuming the large pores are not simultaneously filled, the small pore governs the range up to 67 % surface coverage which has an average value of 4.2 kJ mol^{-1} and last the large pore is filled with an average value of 3.6 kJ mol^{-1} in the range investigated.

All average values for the isosteric enthalpy of adsorption and the corresponding pore size are summerized in table 3.2. The data of table 3.2 are presented in figure 3.21 where the red line is intended to guide the eye.

IUPAC classification	Material	Pore diameter	Average isosteric enthalpy of adsorption
ultra-microporous	Mg-formate	3.4-4.6 Å	6.6 kJ mol ⁻¹
	MFU-4	(3.87 Å, 11.9 Å)	6.8 kJ mol ⁻¹
	Cu-BTC	5 Å	5.8 kJ mol ⁻¹
super-micro-porous	MIL-101	7 Å	5.2 kJ mol ⁻¹
	DUT-4	9 Å	5.4 kJ mol ⁻¹
	Cu-BTC	9 Å	4.9 kJ mol ⁻¹
	DUT-5	11 Å	4.29 kJ mol ⁻¹
	MOF-177	11 Å	3.7 kJ mol ⁻¹
	MFU-4L	12 Å	3.5 kJ mol ⁻¹
	MOF-5	12 Å	4.4 kJ mol ⁻¹
		15 Å	3.6 kJ mol ⁻¹
	MFU-4L	19 Å	3.5 kJ mol ⁻¹
meso-porous	MIL-101	29 Å	4.2 kJ mol ⁻¹
		34 Å	3.6 kJ mol ⁻¹

Table 3.2: Pore diameter and average isosteric enthalpy of adsorption for metal-organic frameworks.

Figure 3.21: Average isosteric enthalpies of adsorption for different MOFs in dependence of their pore diameter. \square MOF-5, \circ MIL-101, ∇ Cu-BTC, \diamond DUT-4, \triangleright DUT-5, \circ MOF-177, \diamond Mg-formate, and \triangleleft MFU4L.

The ultramicropores yield the highest enthalpies of adsorption of up to 6.8 kJ mol^{-1} . With increasing pore diameter the enthalpy decreases strongly. The comparably high enthalpy of adsorption for the medium pore of MIL-101 (4.2 kJ mol^{-1}) could be influenced from the small side pockets. The adsorption isotherm did not reach saturation at 77 K and 2 MPa. Therefore the surface of the large pore is not completely populated and thus the uptake for each pore calculated from the surface ratio underestimates the uptake of the smaller pores. Therefore some of the hydrogen accounted to the medium pore might be adsorbed in the small pore, giving rise to the high enthalpy of adsorption for the 29 \AA pore. Decreasing binding strength with increasing pore diameter in MOFs was shown before by various experimental techniques. Panella et al. [46] showed by thermal desorption spectroscopy (TDS) on various MOFs that the desorption temperature, which is related to the binding strength, decreases strongly for increasing pore diameter. For MOFs with different pores, e.g. Cu-BTC, distinct peaks in the desorption spectrum were observed and correlated to first desorption from the larger pore and, at elevated temperature, from the smaller pore.

For the same MOF, Cu-BTC, Peterson et al. [58] investigated adsorption sites for hydrogen by neutron powder diffraction. The strongest adsorption site was offered by the metal cluster, followed by the small pore and the weakest adsorption site was observed in the large pore. Similarly, Yildirim and Hartman [54] investigated adsorption sites in MOF-5 by neutron powder diffraction and reported nine adsorption sites which can be assigned to adsorption at the metal center, followed by narrow windows, the small pore and last the large pore.

Also various theoretical calculations, e.g. by Frost et al. [67] and Kuc et al. [68, 69], yield that decreasing pore size leads to increased enthalpy of adsorption in MOFs.

Micropore volume

The specific pore volume (SPV) is determined by nitrogen adsorption at 77 K according to Gurvich's rule (section 2.1.4) and reported in the overview table 2.1. While the BET SSA is determined typically at a relative pressure below 0.35 where monolayer adsorption should be completed, the SPV is determined at a relative pressure of 0.95 where the pores of the material are completely filled. The difference in the uptake between the relative pressure used for BET SSA and SPV is the amount of gas adsorbed in multilayers. If an arbitrary orientation of the adsorbed nitrogen molecules is assumed, they can be approximated as spheres with a diameter of approximately 4.5 Å. The investigated materials are microporous, except for MIL-101 which is just above the border to mesoporous materials. To accommodate one molecule in the second layer a minimum diameter of 15 Å is required for the pore as indicated in figure 3.22. The pores

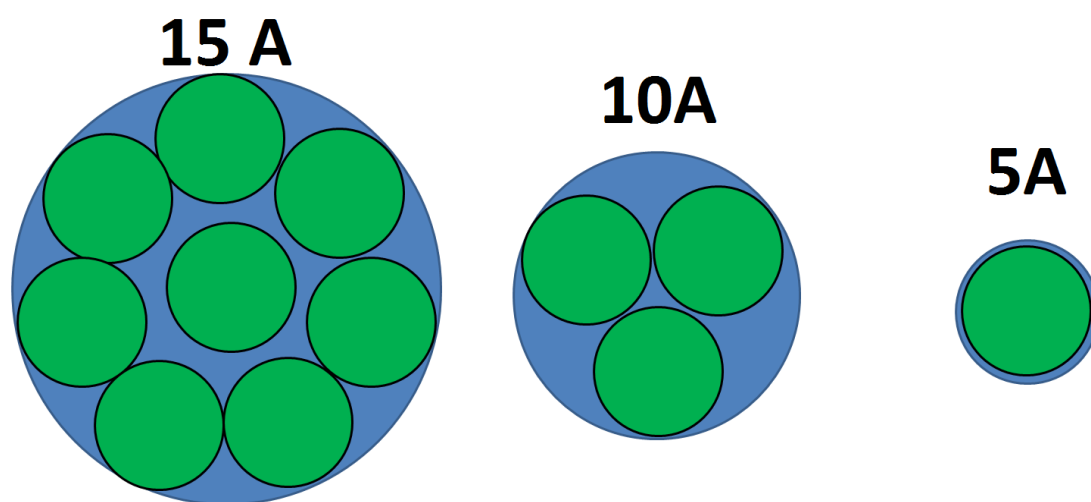


Figure 3.22: A sketch of nitrogen molecules in small pores. A minimum diameter of 15 Å is required to enable multilayer adsorption.

of most investigated MOFs are in the range of 15 Å and therefore almost no multilayer adsorption will take place. For materials in which only one monolayer is adsorbed, the BET SSA and the SPV are proportional with a correlation factor of 3.56×10^{-8} cm. In figure 3.23 the SPV of the investigated materials is shown in dependence of the BET SSA. The dashed line indicates the position of materials that adsorb only a monolayer. As expected from the framework topology, all materials are close to this linear correlation, which is a clear indication for mainly monolayer adsorption. This implies that the total surface area consists of the inner surface provided by the micropores and not by larger mesopores or outer surface, which is negligible. MIL-101 and MOF-177 have the largest pores, which enables more molecules to adsorb in second and higher layers. This is observed in figure 3.23 as they exhibit the largest deviation from the linear correlation for monolayer adsorption.

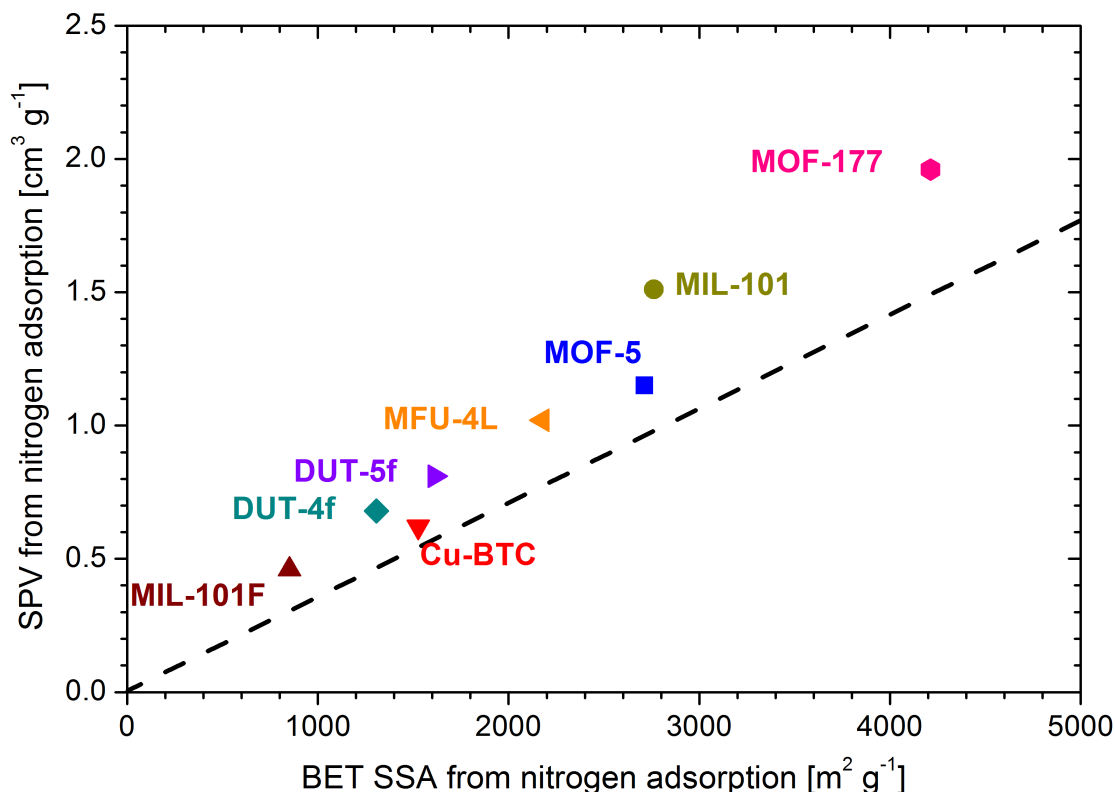


Figure 3.23: The specific pore volume of the investigated materials correlates almost linear to the BET specific surface area. The dashed line indicates the lower limit for the materials as pure monolayer adsorption is assumed.

Gating effect in MFU-4 at 77 K

The isosteric enthalpy of adsorption for hydrogen in MFU-4 is constant at 6.8 kJ mol^{-1} over a wide range of surface coverage. This high heat of adsorption originates from the strong adsorption site offered by the small pore. As shown in figure 3.24, MFU-4 has an alternating pore structure with pores of 3.88 \AA and 11.9 \AA in diameter using the van der Waals radii of the framework atoms. The windows between the pores are even smaller with a diameter of 2.5 \AA . For comparison the pore structure of MFU4-L is shown in figure 3.24, which is has a longer ligand and therefore pores with diameters of 12.0 \AA and 18.6 \AA . In both figures a hydrogen molecule is indicated as a sphere with the kinetic diameter of hydrogen which is 2.98 \AA . To penetrate the framework molecules have to pass through the window and the small pore. Larger molecules e.g. nitrogen with a kinetic diameter of 3.681 \AA is excluded from penetrating the framework. For small molecules, like hydrogen, the small pores offer strong adsorption sites and are therefore occupied first. The observed saturation hydrogen uptake of 2.58 wt% at 77 K corresponds to 100 hydrogen molecules per unit cell which contains three small and three large pores. Owing to the size of the small pore only one molecule can be accommodated and therefore only

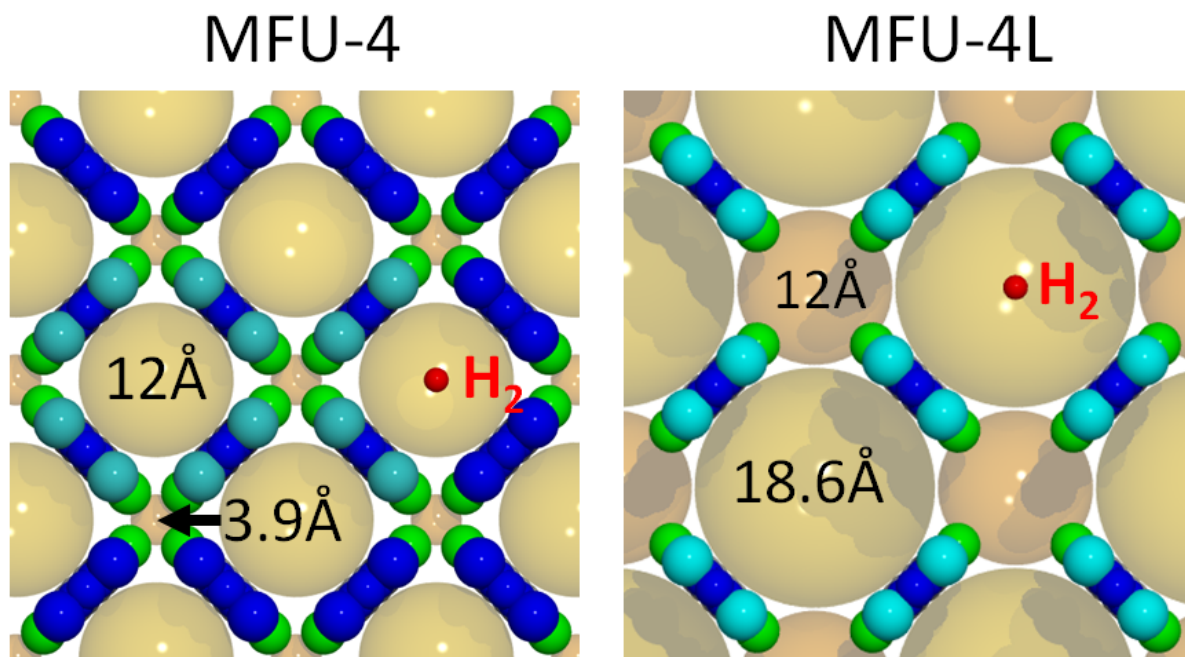


Figure 3.24: Pore structure of MFU-4 and MFU-4L using van der Waals radii of the framework atoms (blue and green). The yellow and orange spheres represent the free volume. For comparison a hydrogen molecule (kinetic diameter: 2.98 Å) is indicated in red.

3% of the maximum hydrogen uptake corresponds to hydrogen molecules adsorbed in the small cell. To enter the large pore molecules need to pass through the small pores. Owing to their diameter, the small pores are blocked if only one molecule is adsorbed in the pore and form a strong barrier for other hydrogen molecules to pass through. Therefore these small pores govern the kinetics and adsorption enthalpy of MFU-4, which is reflected in the high heat of adsorption over a large range of surface coverage and the exclusion of large molecules like nitrogen.

3.2 Low pressure hydrogen adsorption

3.2.1 Volumetric device for low pressure and low temperature adsorption

The Quantachrome Autosorb is like the PCTPro2000, a fully automated set-up based on the Sieverts' apparatus. Compared to the PCTPro2000 the volumes in the Autosorb are much larger with $V_{res} = 19 \text{ cm}^3$ and $V_{sh} = 10 \text{ cm}^3$. However the set-up is able to measure very small amounts of sample accurately (section 3.2.2) as the the pressure transducers are extremely sensitive. There are five pressure transducers covering the range up to only 0.1 MPa. The most sensitive one has a maximum pressure of 133 Pa. Therefore, measurements can be performed in the range of $1 \times 10^{-8} - 0.1 \text{ MPa}$ on sample masses of approximately 20 mg.

Originally the Autosorb is equipped with a liquid bath cryostat for nitrogen. In order to measure at temperatures down to 20 K, a helium flow cryostat was developed. The

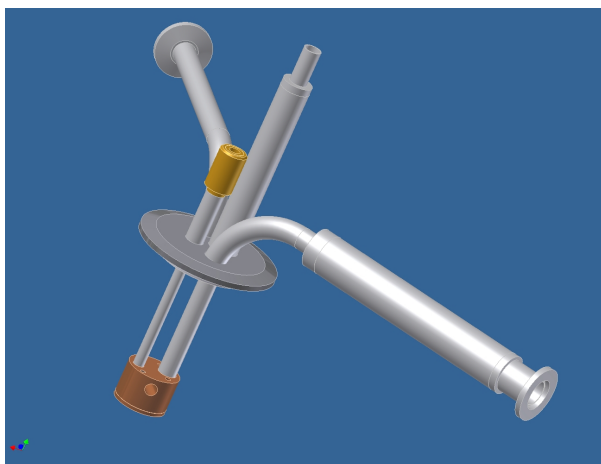


Figure 3.25: Inner part of the cryostat developed to measure hydrogen adsorption at 20 K with the Quantachrome Autosorb.

inner part of the cryostat is shown in figure 3.25. The lower part with the sample holder is surrounded by an isolation vacuum. Liquid helium is pumped through a small copper block which contains the sample cell. In the hole of the copper block a heating element is placed as counterpart to the cooling provided by the liquid helium flow. Temperature is measured with a platinum resistor (PT-111) which is placed in the copper block close to the sample cell and controlled by a temperature controller (ITC503). The cryostat can reach temperatures down to approximately 11 K.

The sample is placed in a small steel basket which is positioned at the bottom of the sample cell. To reduce the empty volume in the sample cell a glass cylinder is used which fills up the volume above the sample holder. The sample holder and the reference cell can be connected to the Autosorb set-up which contains the reservoir volume and pressure gauges.

3.2.2 Calibration

Temperature Calibration

Hydrogen exists in two spin states which are named ortho- and para-hydrogen. At room temperature hydrogen in equilibrium is a mixture of both configuration with approximately 75% ortho-hydrogen (p-hydrogen) and 25% para-hydrogen (o-hydrogen). In the following this room temperature mixture is named normal-hydrogen (n-hydrogen). At temperatures below 200 K the portion of p-hydrogen is increasing strongly, a 1:1 mixture is reached at approximately 80 K and below 25 K all hydrogen is in the para configuration. The conversion from ortho- to para-hydrogen is in general quite slow but can be much faster if hydrogen is adsorbed on a surface [5, 70]. In the adsorption experiment, hydrogen is cooled down from room temperature and is therefore a mixture of para- and ortho-configuration with a ratio greater 1:3. Therefore the properties of adsorbed hydrogen may range between the properties of n-hydrogen and p-hydrogen for which the saturation pressure for liquefaction are given in table 3.3 and shown in figure 3.26. The saturation pressure in dependence of the temperature can be approximated for both mixtures by a polynomial of 4th order.

temperature [K]	normal-hydrogen pressure [kPa]	para-hydrogen pressure [kPa]
14	7,451	7,88
15	12,74	13,42
16	20,54	21,54
17	31,50	32,91
18	46,29	48,20
19	65,61	68,12
21	90,21	93,42
22	120,9	124,9

Table 3.3: Saturation pressure of normal- and para-hydrogen [71].

In the cryostat of the Autosorb the temperature is measured by a platinum resistor which is in the copper block of the sample holder. Platinum resistors are in general well calibrated above 70 K where the resistance is increasing linear with temperature. At low temperatures the resistance is not linear any more and depends strongly on the residual resistance of the individual platinum resistor. Therefore it is necessary to calibrate the platinum resistor. The resistor is calibrated in the set-up, therefore any temperature differences between the sample holder and the location of the resistor is included in the calibration. For the calibration of the resistor, different temperatures have been set by the temperature control and the corresponding liquefaction pressure of hydrogen is measured. The liquefaction pressure is directly correlated to the temperature by the phase diagram (figure 3.26) and therefore the temperature in the sample holder is known. Analogous measurements were performed for the liquefaction of nitrogen. It is assumed

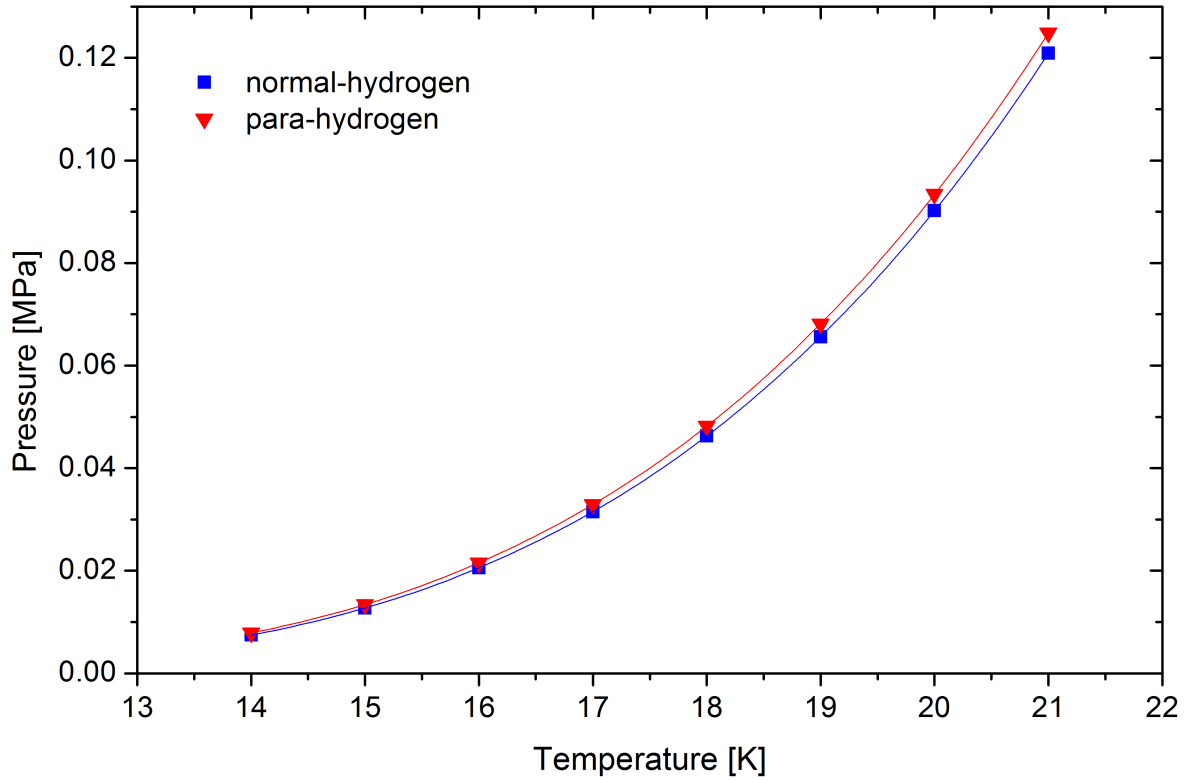


Figure 3.26: Phase diagram of hydrogen at low temperature and pressure [71].

that above 200 K the temperature gradient between PT-resistor and sample holder is negligible and the resistance increases with the temperature according to DIN IEC 751. During the measurement the temperature remains constant to approximately ± 0.1 K.

Volume Calibration and temperature gradient correction

The volume of the sample holder is calibrated by expansion of helium. At room temperature, the reservoir volume is loaded with a defined pressure and then the helium is allowed to expand to the evacuated sample holder. This yields a sample holder volume of $V_{sh} = 10.085 \pm 0.003 \text{ cm}^3$.

For the low temperature measurement the sample holder is partly cooled to 19.5 K. Between the cooled part and the apparatus a temperature gradient from 19.5 K to room temperature is present which needs to be corrected for. The easiest assumption for the temperature gradient is to assume only two different temperatures within the volume of the sample holder: an imaginary volume V_{cold} at 19.5 K and a volume V_{RT} at room temperature

$$V_{sh} = V_{cold} + V_{RT} \quad (3.9)$$

To calculate this imaginary cold volume V_{cold} gas expansion from the reservoir to the sample holder volume is measured. The equilibrium pressure is lower than expected if the sample holder was at room temperature, as the gas density in the cold part is higher than for room temperature. From the equilibrium pressure the imaginary cold volume is calculated to $V_{cold} = 0.6574 \text{ cm}^3$.

In figure 3.27 the hydrogen amount in the empty sample holder at 19.5 K is shown using the calculated imaginary cold volume. Therefore the uncertainty of the hydrogen amount in the empty sample holder is 0.4 cm^3 (STP) which is $18 \mu\text{g}$. For the measurements the

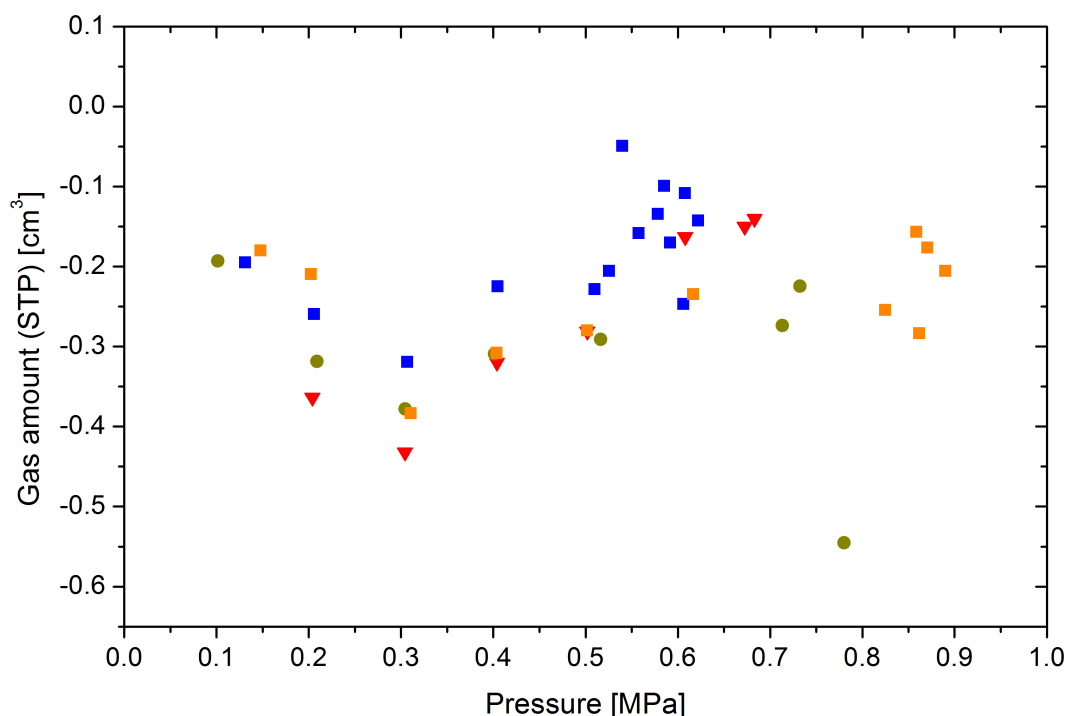


Figure 3.27: Four measurements of the hydrogen amount in an empty sample holder of the Autosorb cryostat at 19.5 K.

material mass is approximately 20 mg. The skeletal density, determined with helium at room temperature, is for most metal-organic frameworks approximately $1.5 - 2 \text{ cm}^3 \text{ g}^{-1}$ (table 2.1) which results in a skeleton volume of the materials below 0.01 cm^3 . This volume at 19.5 K and 0.1 MPa would accommodate 0.1 cm^3 (STP) of hydrogen which is below the uncertainty of the measurement. Therefore the skeletal volume of the materials can be neglected and the imaginary cold volume is regarded as constant for all materials investigated.

3.2.3 Results

Hydrogen adsorption isotherms at 19.5 K

Low pressure high resolution adsorption and desorption isotherms are measured by a fully automated volumetric device Autosorb1 (Quantachrome GmbH) at temperatures around 20 K and pressure below 0.1 MPa. The materials are activated by heating under high vacuum for several hours prior to the measurement. Typical sample masses are 14 – 30 mg. The isotherm is measured by predefining the equilibrium pressure for each point and the machine is dosing gas as often as needed to reach equilibrium at that pressure. The relative pressure p is defined as the ratio of the pressure P to the saturation pressure P_0 and therefore saturation is reached at $p = 1$. Figure 3.28 shows the hydrogen uptake of MIL-101 at 19.5 K in cm^3 at STP per material mass in dependence of the relative pressure p . The isotherm exhibits a typical type I behavior with a very

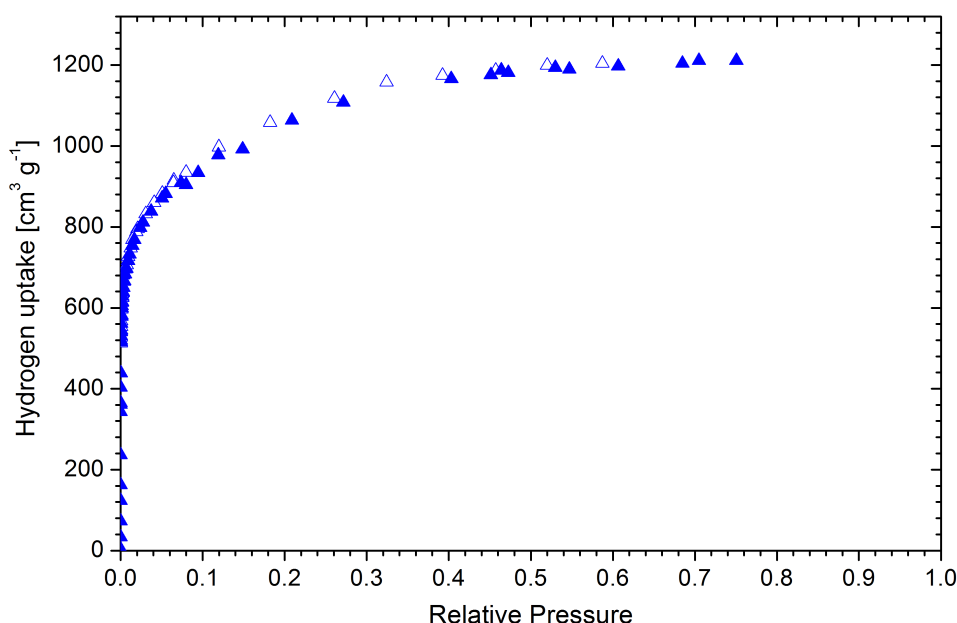


Figure 3.28: Hydrogen uptake of MIL-101 at 19.5 K.

steep initial increase at low pressure followed by a saturation plateau. Saturation uptake of approximately $1200 \text{ cm}^3 \text{ g}^{-1}$ (9.6 wt%) is reached above a relative pressure of $p = 0.5$. Desorption is measured from $p = 0.7$ to $p = 3 \times 10^{-4}$. The isotherm is fully reversible and no hysteresis is observed, which is typical for physisorption. From the saturation uptake the pore volume is calculated according to Gurvich's rule to $1.5 \text{ cm}^3 \text{ g}^{-1}$. Additionally, from these low pressure isotherms the specific surface area can be calculated according to the BET model. For MIL-101 the hydrogen adsorption isotherm yields a specific BET surface area of $3007 \text{ m}^2 \text{ g}^{-1}$.

For MOF-5, DUT-4o, DUT-5o, Cu-BTC, MOF-177 and MFU-4L the shape of the isotherm is similar but the saturation uptake ranges from $300 \text{ cm}^3 \text{ g}^{-1}$ (2.6 wt%) to

$1550 \text{ cm}^3 \text{ g}^{-1}$ (12 wt%) for DUT-4o and MOF-177, respectively. The saturation hydrogen uptakes, specific BET surface areas, and pore volumes are summarized in the table 3.4. To have a better insight in the adsorption properties of the material, the adsorption and desorption isotherms are presented in a logarithmic pressure scale in figure 3.29 - 3.35. The two ultramicroporous materials Mg-formate and MFU-4 were also measured but adsorb only 0.05 wt% and 0.14 wt%, respectively, which is for both materials within the experimental uncertainty of 0.4 cm^3 .

The hydrogen uptake of the supermicroporous materials, MFU-4L, MOF-5, DUT-4o, DUT-5o, Cu-BTC, and MOF-177, are presented in figure 3.29 -3.34.

MFU-4L with a bimodal pore size distribution shows a clear step-like behavior. In adsorption there is a very small step at relative pressure below $p = 4 \times 10^{-5}$ with a hydrogen uptake of approximately $70 \text{ cm}^3 \text{ g}^{-1}$. This small step is followed by two larger steps at higher relative pressure. The second step reaches up to $700 \text{ cm}^3 \text{ g}^{-1}$ hydrogen uptake at a relative pressure of $p = 3 \times 10^{-3}$ and the third step yields a maximum hydrogen uptake of MFU-4L of $1050 \text{ cm}^3 \text{ g}^{-1}$ at $p = 0.95$. Owing to temperature fluctuations, the pressure of the sample cell sometimes increases quickly which yields scatter in the adsorption isotherm. Desorption from $p = 0.6$ to $p = 7 \times 10^{-4}$ exhibits like in MIL-101 no hysteresis compared to the adsorption isotherm, which is typical for physisorption.

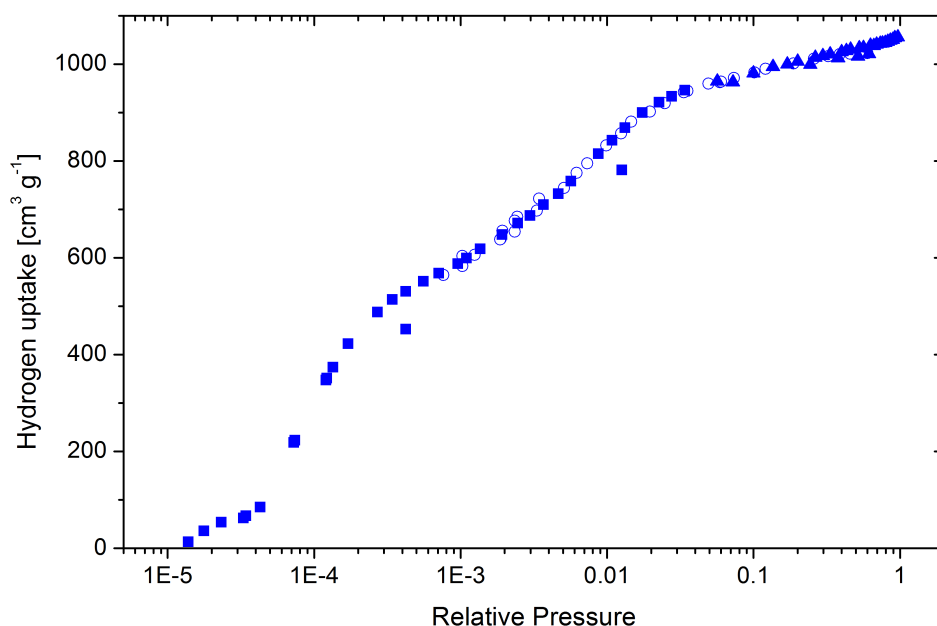


Figure 3.29: Hydrogen adsorption of MFU-4L at 19.5 K.

MOF-5, which has the same topology as MFU-4L but smaller pores, was measured at 19.5 K, 25.5 K, and 31.0 K. At 19.5 K, the hydrogen uptake increases slowly with the relative pressure up to $p = 2 \times 10^{-5}$ where an hydrogen uptake of $180 \text{ cm}^3 \text{ g}^{-1}$ is reached. Then a very steep increase up to $600 \text{ cm}^3 \text{ g}^{-1}$ at $p = 5 \times 10^{-5}$ is observed, which is followed by two small steps that reach their maximum at $p = 1 \times 10^{-3}$ ($820 \text{ cm}^3 \text{ g}^{-1}$) and $p = 2 \times 10^{-3}$ ($1000 \text{ cm}^3 \text{ g}^{-1}$). This is followed by a slow linear increase up to $1100 \text{ cm}^3 \text{ g}^{-1}$ at $p = 0.8$. Increasing the temperature by 6 K to 25.5 K yields the same adsorption isotherm up to $p = 5 \times 10^{-5}$ where the first pronounced step is completed. Afterwards the two smaller steps are shifted to higher relative pressure compared to the 19.5 K isotherm and the step-like behavior is less distinct. The maximum hydrogen uptake is reached at approximately $p = 0.01$ with an hydrogen uptake of $1000 \text{ cm}^3 \text{ g}^{-1}$. At 31 K, the small initial increase in hydrogen uptake with pressure remains the same as for 19.5 K and 25.5 K, but than even the first step is shifted to higher relative pressure. The region of initial increase ends at $p = 1 \times 10^{-4}$ where the first step starts. The slope starts to decrease again at an uptake of $600 \text{ cm}^3 \text{ g}^{-1}$ which is reached at $p = 7 \times 10^{-4}$. At higher pressure a linear increase of the hydrogen uptake with the logarithm of the relative pressure is observed. At $p = 0.15$ the hydrogen uptake is $1000 \text{ cm}^3 \text{ g}^{-1}$ which is close to the uptake at 19.5 K of $1100 \text{ cm}^3 \text{ g}^{-1}$.

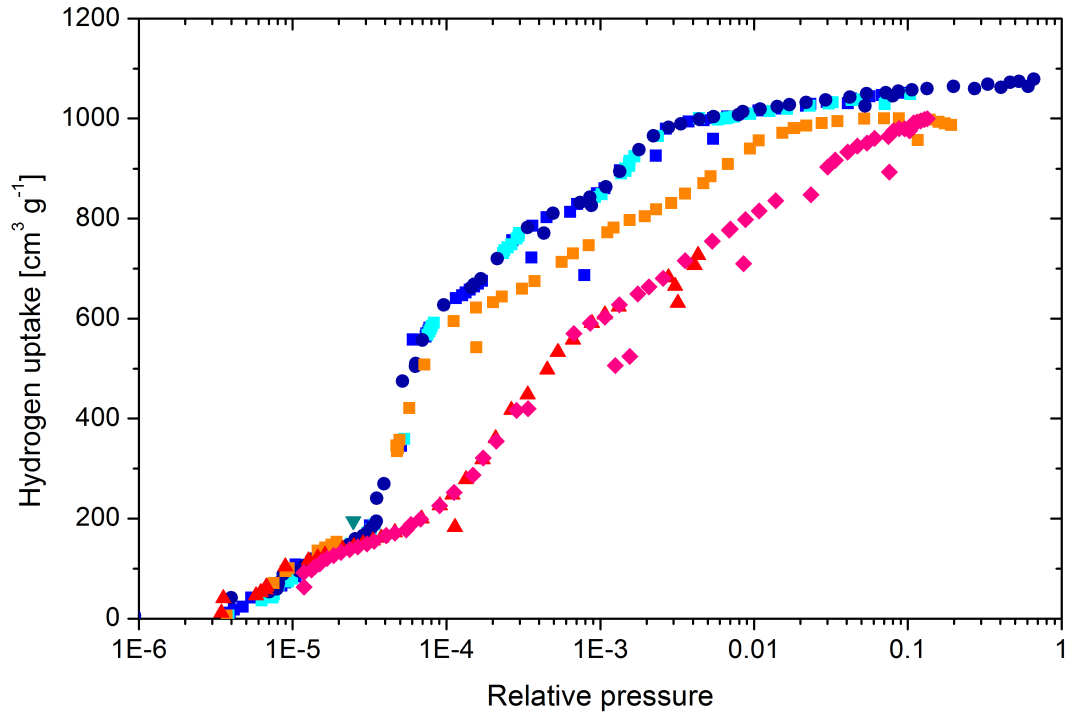


Figure 3.30: Hydrogen adsorption of MOF-5 at 19.5 K (blue and turquoise), 25.5 K (orange) and 31.0 K (red and pink).

For DUT-4o a slow initial increase which is becoming steeper up to $p = 4 \times 10^{-5}$ is observed. Then the slope is decreasing till a region where the hydrogen uptake is proportional to the logarithm of the pressure is reached. This linear region stretches from $p = 3 \times 10^{-4}$ to $p = 0.3$. At higher pressure the slope is increasing again till liquefaction is reached at a relative pressure of $p = 1$.

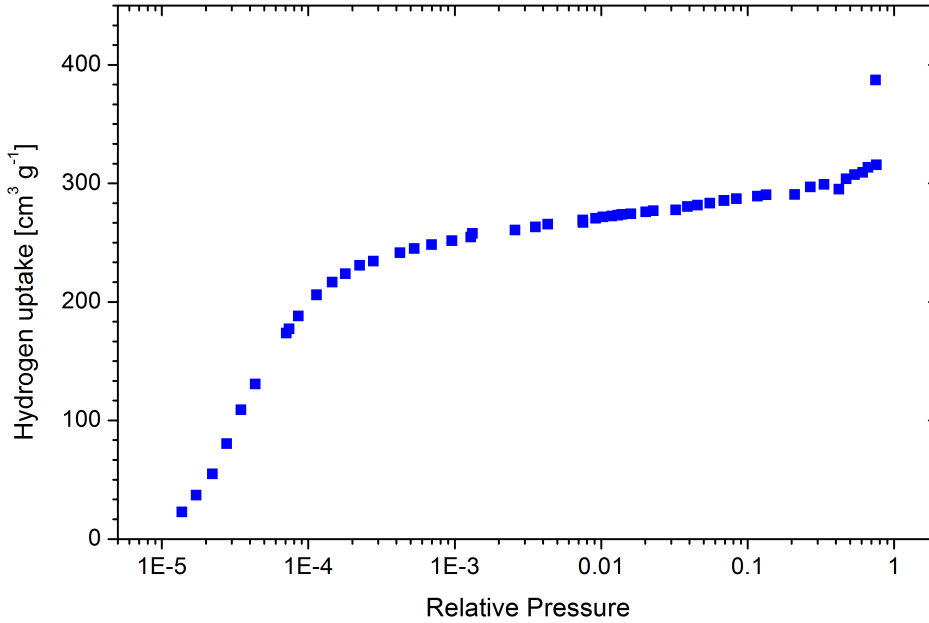


Figure 3.31: Hydrogen adsorption of DUT-4o at 19.5 K.

DUT-5o shows similar hydrogen adsorption behavior at 19.5 K as DUT-4o up to $p = 3 \times 10^{-4}$. The first increase is saturated at a higher hydrogen uptake of $350 \text{ cm}^3 \text{ g}^{-1}$ compared to $240 \text{ cm}^3 \text{ g}^{-1}$ for DUT-4. At higher pressure the slope of the isotherm increases again for a second smaller step at $p = 6 \times 10^{-4} - 6 \times 10^{-3}$. At higher relative pressure the hydrogen uptake correlates linear to the logarithm of the pressure. A maximum hydrogen uptake of $550 \text{ cm}^3 \text{ g}^{-1}$ is reached at $p = 0.9$. Desorption is measured down to $p = 1 \times 10^{-4}$ and reproduces well the intermediate step.

For Cu-BTC (figure 3.33) the hydrogen uptake also rises strongly with increasing pressure up to a relative pressure of $p = 1 \times 10^{-3}$ and then the slope is decreasing and it seems as if a saturation will be reached, but at $p = 0.05$ a small step in this saturation is reached where the uptake is increasing from $760 \text{ cm}^3 \text{ g}^{-1}$ to $800 \text{ cm}^3 \text{ g}^{-1}$. At higher pressure the hydrogen uptake remains constant up to $p = 0.9$ where the measurement ends.

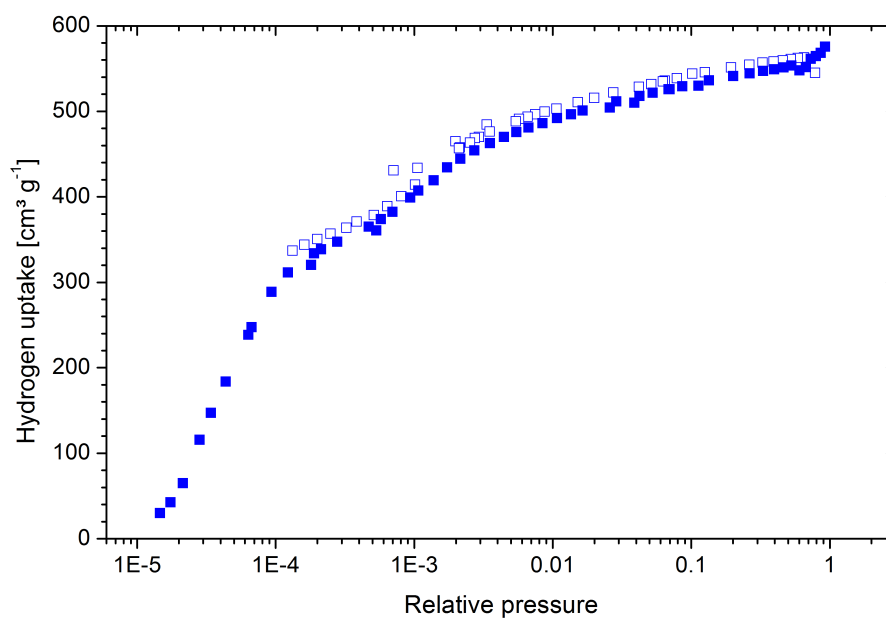


Figure 3.32: Hydrogen adsorption (filled symbols) and desorption (open symbols) of DUT-5o at 19.5 K.

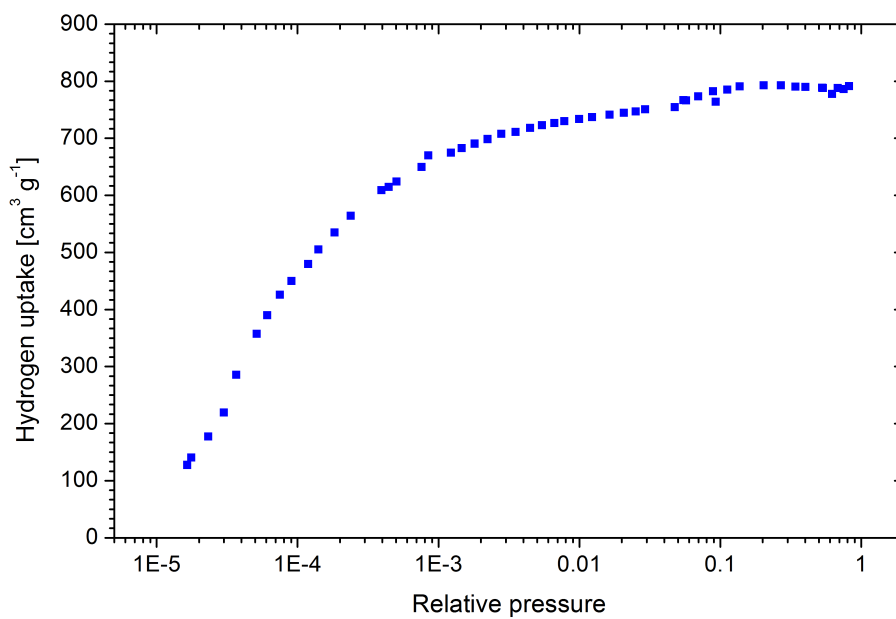


Figure 3.33: Hydrogen adsorption of Cu-BTC at 19.5 K.

MOF-177 (figure 3.34) exhibits a multi-step behavior with a maximum hydrogen uptake at $p = 0.9$ of $1550 \text{ cm}^3 \text{ g}^{-1}$. The first small step is observed below $p = 4 \times 10^{-5}$ with an uptake of approximately $100 \text{ cm}^3 \text{ g}^{-1}$. Then a second step with an elbow at $p = 1 \times 10^{-4}$ and a third at $p = 1 \times 10^{-2}$ is observed. At higher pressure the hydrogen uptake increases by $150 \text{ cm}^3 \text{ g}^{-1}$ over the relative pressure range of $p = 1 \times 10^{-2}$ -0.9.

The hydrogen adsorption isotherm of the mesoporous material, MIL-101, is shown in

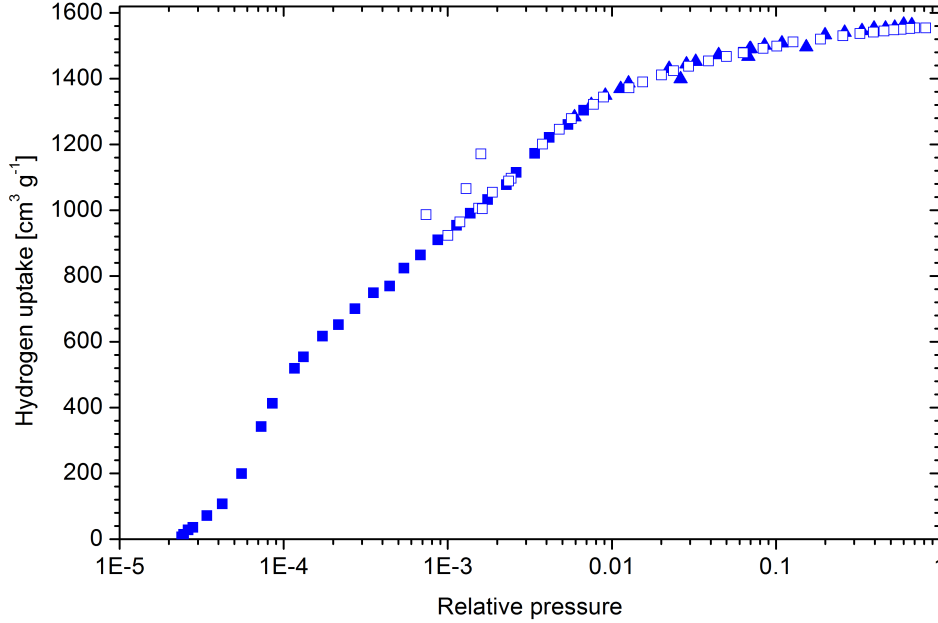


Figure 3.34: Hydrogen adsorption (filled symbols) and desorption (open symbols) of MOF-177 at 19.5 K.

figure 3.35 which exhibits a clear two-step behavior. In contrast to the supermicroporous materials, for which the steps, if observed, occur at very low pressure, the steps are at higher pressure for the mesoporous material. The elbow of the first step is at $p = 3 \times 10^{-4}$ and the second step is starting slowly afterwards. The elbow of the second step is reached at $p = 0.4$, where the maximum uptake of $1200 \text{ cm}^3 \text{ g}^{-1}$ is observed. The desorption isotherm shows no hysteresis compared to the adsorption isotherm down to $p = 3 \times 10^{-4}$ and both steps are well reproduced.

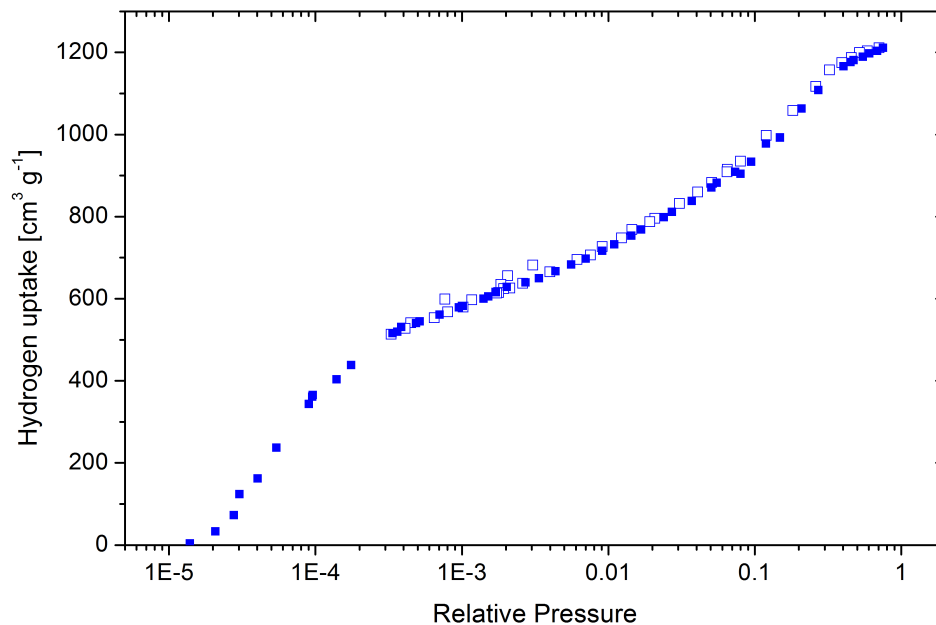


Figure 3.35: Hydrogen adsorption (filled symbols) and desorption (open symbols) of MIL-101 at 19.5 K.

IUPAC classification	Material	Saturation H ₂ uptake at 19.5 K	SSA	SPV
super-microporous	MFU-4L	1040 cm ³ g ⁻¹ (8.4 wt%)	3143 m ² g ⁻¹	1.20 cm ³ g ⁻¹
	MOF-5	1070 cm ³ g ⁻¹ (8.6 wt%)	3511 m ² g ⁻¹	1.33 cm ³ g ⁻¹
	DUT-4o	300 cm ³ g ⁻¹ (2.6 wt%)	702 m ² g ⁻¹	0.37 cm ³ g ⁻¹
	DUT-5o	550 cm ³ g ⁻¹ (4.6 wt%)	2023 m ² g ⁻¹	0.74 cm ³ g ⁻¹
	Cu-BTC	790 cm ³ g ⁻¹ (6.5 wt%)	2570 m ² g ⁻¹	0.93 cm ³ g ⁻¹
	MOF-177	1550 cm ³ g ⁻¹ (12 wt%)	4558 m ² g ⁻¹	1.77 cm ³ g ⁻¹
mesoporous	MIL-101	1210 cm ³ g ⁻¹ (9.6 wt%)	3007 m ² g ⁻¹	1.50 cm ³ g ⁻¹

Table 3.4: Hydrogen uptake, specific surface area, and specific pore volume of metal-organic frameworks determined by hydrogen adsorption at 19.5 K.

Temperature dependent pressure change

For detailed understanding of the storage properties it is important to investigate the influence of temperature change of the hydrogen storage system. Therefore the activated material in the sample holder is loaded with 0.107 MPa hydrogen at room temperature and the connection valve is closed so that the volume available for the gas remains constant. Then the sample holder is cooled to approximately 11 K where hydrogen is liquid. The pressure is monitored while the sample is heated to different temperatures which are kept constant for approximately 2 min and the pressure is recorded.

Mesoporous materials

For the mesoporous MIL-101 the measured pressure in the dependence of the temperature is presented in figure 3.36 in red and the pressure of the empty sample in black. In the empty sample holder, below 20 K the pressure is almost 0 mmHg as the hydrogen

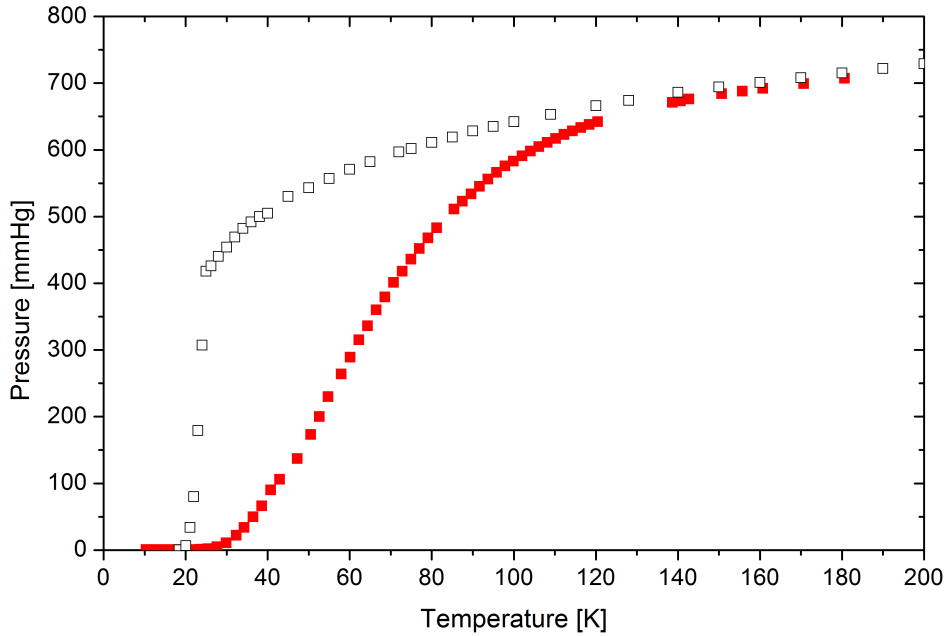


Figure 3.36: Pressure in the sample holder in dependence of the temperature for the empty sample holder (□) and when containing MIL-101 (■).

in the sample holder is liquid. Slightly above 20 K the phase transition to gaseous is observed by a sudden strong increase of the pressure in the sample holder. Then the slope is becoming smaller with increasing temperature as the hydrogen remains in the gaseous phase and the pressure is only increasing due to thermal expansion. The deviation from linear increase of pressure with temperature is included in the correction factor Z for real gases in the ideal gas equation (equation 4.1). With adsorbing material in the sample holder the pressure develops differently. The pressure remains at very low level up to approximately 40 K. Then a s-shaped increase in the pressure is observed until

3 Experimentals, Results and Discussion

the pressure of the empty sample holder at approximately 120 K is reached. Afterwards, the pressure correlates linearly with the temperature. The pressure difference between the two measurements depends on the amount of hydrogen adsorbed on the material. The amount of gas adsorbed on the material is given for any temperature by

$$n_{ads}(T) = n_{ini} - n_{gas}(T) \quad (3.10)$$

where n_{ini} represents the total amount of gas present in the sample holder which can be calculated from the loading pressure P_{ini} , room temperature at loading T_{RT} , and the volume of the sample holder V_{sh} .

$$n_{ini} = \frac{P_{ini} \cdot V_{sh}}{R \cdot T_{RT}}. \quad (3.11)$$

The amount of gas in the gas phase $n_{gas}(T)$ of the sample holder filled with adsorbing material at the temperature T can be calculated from the pressure $P_{(T)}$ using

$$n_{gas}(T) = \frac{P_{(T)} \cdot V_{(T)}}{Z_{(P_{(T)})} \cdot R \cdot T} \quad (3.12)$$

where $Z_{(P_{(T)})}$ is the correction factor for the ideal gas equation (equation 4.1) and $V_{(T)}$ is an imaginary volume that contains the amount of gas n_{ini} at the temperature T . This is not equal to the sample holder volume, as the sample holder volume is only partly cooled and exposed to a strong temperature gradient up to room temperature. This imaginary volume can be calculated from the measurement of the empty sample holder

$$V_{(T)} = \frac{n_{ini} \cdot R \cdot T \cdot Z_{(P_{empty}(T))}}{P_{empty}(T)}. \quad (3.13)$$

From equations 3.10-3.13 the amount of gas adsorbed on the material can be derived as

$$n_{ads}(T) = \frac{P_{ini} \cdot V_{sh}}{R \cdot T_{RT}} \cdot \left(1 - \frac{Z_{(P_{empty}(T))} \cdot P_{(T)}}{Z_{(P_{(T)})} \cdot P_{empty}(T)} \right) \quad (3.14)$$

For MIL-101, the resulting hydrogen uptake (blue squares) and the pressure (red squares) is reported in figure 3.37 in dependence of the temperature. Below 30 K, MIL-101 adsorbs all hydrogen present in the sample holder which corresponds to an uptake of 4.2 wt%. At higher temperatures it starts to desorb hydrogen which results in increasing hydrogen pressure in the sample holder. At approximately 140 K the hydrogen uptake is below 0.1 wt% and the pressure is increasing only by expansion of the gas caused by the temperature increase. Additionally to this measurement, results from the high pressure PCT are shown in figure 3.37. These are accomplished by interpolation of the measured hydrogen adsorption isotherm at 77 K, 87 K, 97 K, 112 K, and 127 K.

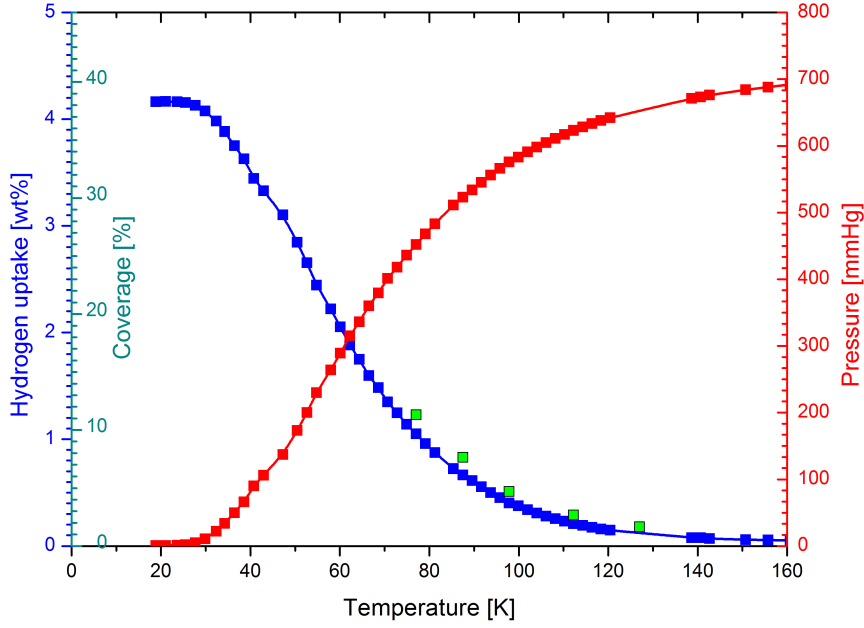


Figure 3.37: Hydrogen adsorbed on MIL-101 (■) in dependence of the temperature and pressure (■). Additionally the hydrogen uptake measured with the high pressure PCT is shown (■), which are extracted from figure 3.14.

Supermicroporous materials

In figure 3.38 and figure 3.39 the amount of adsorbed hydrogen in dependence of the temperature and pressure is shown for the two supermicroporous materials, MOF-177 and MOF-5. The desorption behavior is similar to MIL-101, with a small plateau in the temperature region where all hydrogen is adsorbed, followed by decreasing hydrogen uptake while pressure is increasing, and above approximately 140 K the hydrogen uptake is below 0.1 wt% and the pressure rises slowly due to thermal expansion. For MOF-177 two measurements are performed with different mass of 39.8 mg and 20.8 mg. At low temperature all hydrogen present in the sample holder is adsorbed on the material. As the amount of hydrogen present is the same for both measurements with different sample mass, the same amount of hydrogen is adsorbed at these temperatures. For the measurement with the smaller sample mass this results in a higher weight specific hydrogen uptake compared to the measurement with the higher sample mass. Therefore in the measurement with the small sample mass the surface coverage is higher and adsorption sites with lower interaction energy are occupied. These weak adsorption sites start to desorb hydrogen at lower temperature than the stronger sites and therefore the pressure in the measurement with the small sample mass increases at lower temperatures compared to the measurement with the higher sample mass.

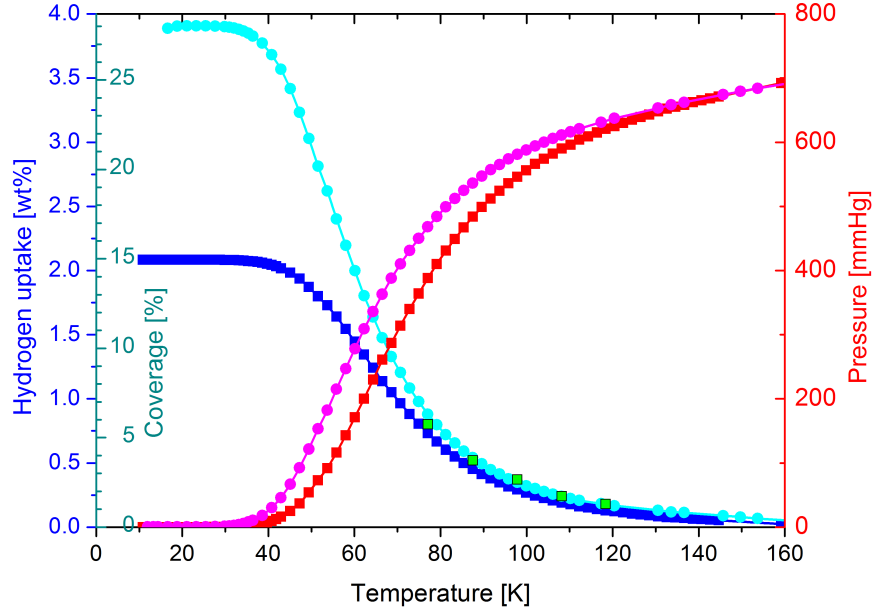


Figure 3.38: Hydrogen adsorbed on MOF-177 (blue and cyan) in dependence of the temperature and pressure (red and pink) for material mass of 39.8 mg (squares) and 20.8 mg (circles). Additionally the hydrogen uptake measured with the high pressure PCT, which are extracted from figure 3.13, is shown for the 39.8 mg sample (■).

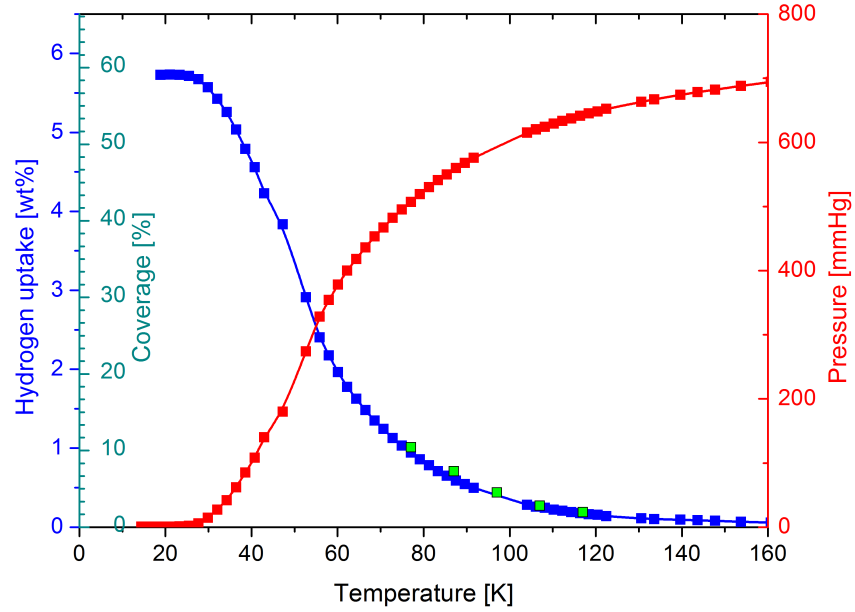


Figure 3.39: Hydrogen adsorbed on MOF-5 (■) in dependence of the temperature and pressure (■). Additionally the hydrogen uptake measured with the high pressure PCT, which are extracted from figure 3.9, is shown (■).

Ultramicroporous materials

In figure 3.40 and 3.41 the hydrogen uptake and pressure in dependence of the temperature are shown for the two ultramicroporous materials, Mg-formate and MFU-4, respectively. In contrast to the meso- and supermicroporous materials, immediately above the boiling point of hydrogen the pressure rises quickly for both ultramicroporous materials, indicating that not all hydrogen available was absorbed. For Mg-formate

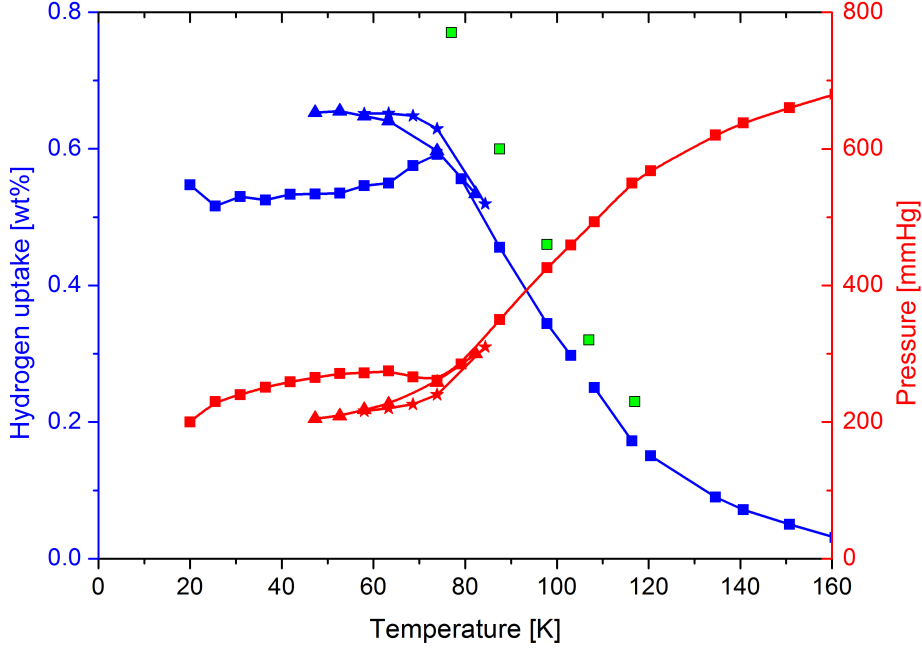


Figure 3.40: Hydrogen uptake (blue) and pressure (red) of Mg-formate in dependence of the temperature for the first heating (squares), first cooling (triangles), and second heating (stars) cycle. Additionally the hydrogen uptake measured with the high pressure PCT, which are extracted from figure 3.7, is shown (■).

(figure 3.40) the pressure rises quickly at very low temperature, as only 0.5 wt% are adsorbed on the material and the rest of the hydrogen is in the liquid phase. Up to a temperature of approximately 60 K the pressure rises slowly and the hydrogen uptake remains approximately constant. At higher temperature the pressure drops slightly and the adsorbed amount increases to 0.6 wt%. Starting from approximately 75 K the pressure increases with temperature and the hydrogen uptake decreases as observed for the supermicroporous and mesoporous materials. After heating, the sample was cooled to different temperatures indicated in figure 3.40 by the triangles. The hydrogen uptake increased up to 80 K as observed by heating. At lower temperature down to 50 K the hydrogen uptake increases above the uptake observed by heating and the pressure decreases. In a second heating cycle, which is indicated in figure 3.40 by the stars, the hydrogen uptake from 50 K remains constant at 0.65 wt% up to 70 K where it starts to decrease and above 80 K yield the same results as in the first cycle.

For MFU-4 a similar behavior as for Mg-formate is observed (figure 3.41). Below 20 K

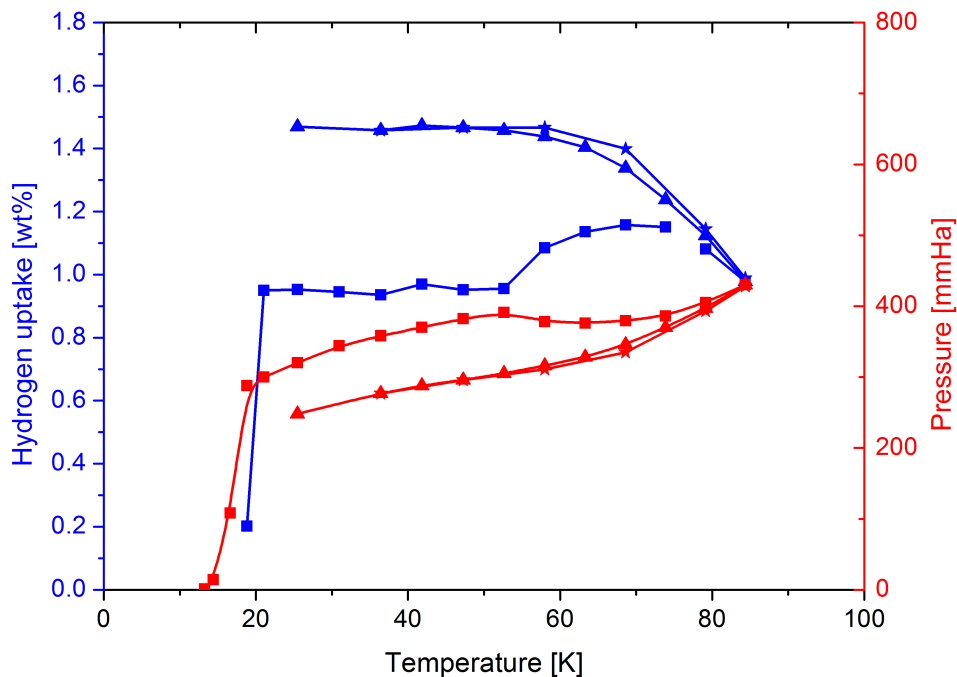


Figure 3.41: Hydrogen uptake (blue) and pressure (red) of MFU-4 in dependence of the temperature for the first heating (squares), first cooling (triangles), and second heating (stars) cycle.

the hydrogen content and the pressure increases strongly owing to the phase transition of non-adsorbed gas from liquid to gaseous. The hydrogen uptake remains afterwards constant at 0.95 wt% up to 50 K where the pressure is slightly decreasing and the uptake increases. At approximately 70 K a maximum uptake of 1.2 wt% at 350 mmHg is reached. At higher temperature the pressure increases and the hydrogen uptake decreases with increasing temperature. For the cooling and second heating cycle similar observations are made as for Mg-formate. With decreasing temperature the uptake increases till approximately 50 K where 1.5 wt% are adsorbed, which remains constant at lower temperature. By heating, the uptake remained constant up to 60 K and then starts to decrease. Above 80 K it is identical to the first cycle.

To get a deeper insight in this unexpected sorption behavior the kinetics of the measurement were recorded. As for the meso- and supermicroporous materials for each temperature approximately 2 min were taken to reach equilibrium. But for these ultramicroporous materials the kinetics depend strongly on the temperature as shown for MFU-4 in figure 3.42. At low temperature up to 50 K, the pressure remains constant over 15 min, which means that equilibrium was already established or the kinetics are too slow to be observed within these 15 min. At 60 K the pressure is slowly decreasing with time at a rate of 0.65 mmHg min⁻¹. For 70 K the pressure is dropping exponentially and faster than for 60 K. At 80 K the pressure remains almost constant over 16 min and

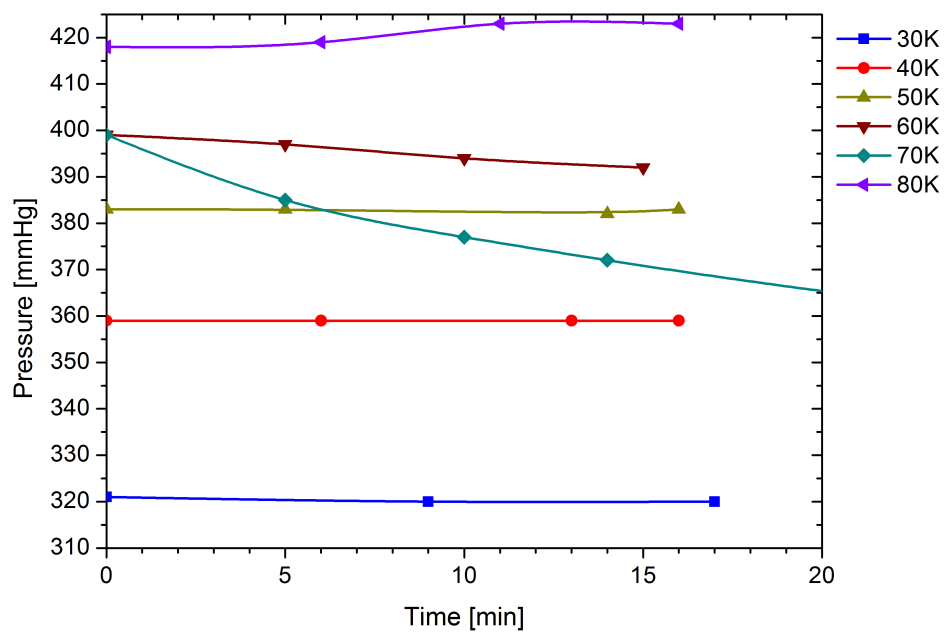


Figure 3.42: Kinetics of the pressure in MFU-4 for different temperatures.

the pressure change can be assigned to temperature fluctuations which with 3 K were high compared to less than 1 K for the other temperatures.

3.2.4 Discussion

Specific Surface Areas and Pore Volumes

The specific surface areas of the supermicroporous and mesoporous materials are calculated from the hydrogen adsorption isotherms at 19.5 K according to the BET-model. As for nitrogen adsorption at 77 K (section 2.2), the pressure range used for the determination of the SSA is chosen according to the criteria suggested by Rouquerol et al. [37]. The SPV is calculated according to Gurvich's rule (section 2.1.4). The SSAs and SPVs from hydrogen adsorption at 19.5 K are given in table 3.4 and are presented in figure 3.43. The dashed line indicates the correlation between SPV and SSA if adsorption occurred in a monolayer without formation of a second layer. As observed in section

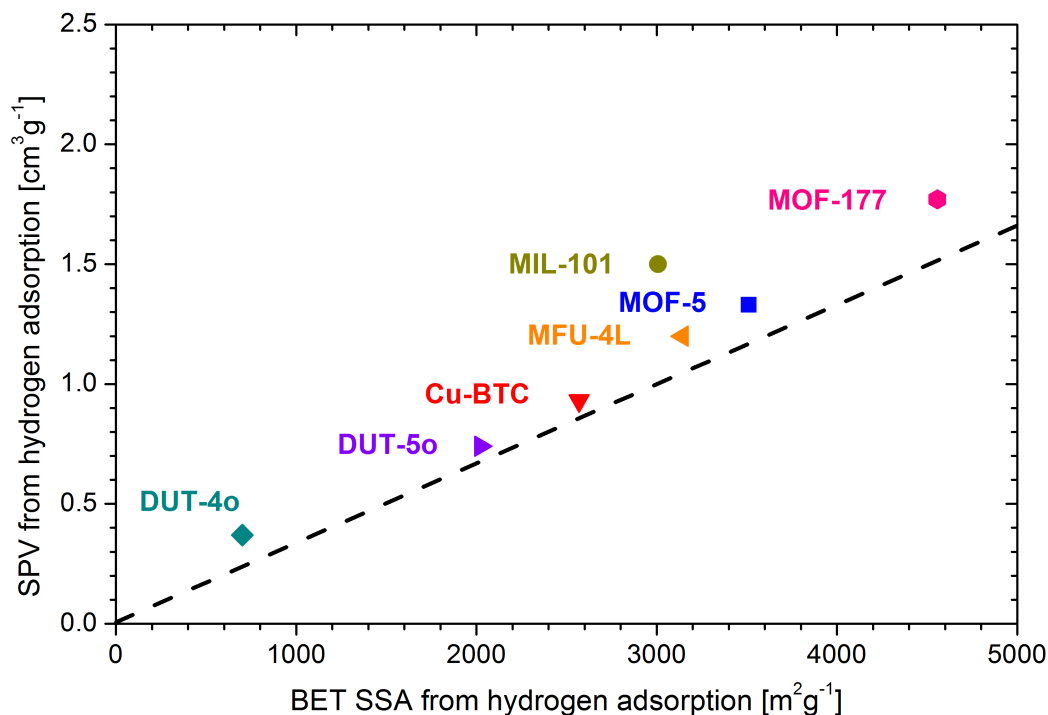


Figure 3.43: The specific pore volume in dependence of the specific surface area determined by hydrogen adsorption at 19.5 K. The dashed line represents pure monolayer adsorption.

3.1.4 for nitrogen at 77 K, the materials investigated have SPVs which are only slightly larger than the volume calculated for pure monolayer adsorption. This indicates that only a few hydrogen molecules are adsorbed in a second or higher layer. The MOFs investigated have pores with a maximum size that correspond to the kinetic diameter of a few hydrogen molecules. The strongest multilayer adsorption is observed for the mesoporous MIL-101 which has the largest pores and the supermicroporous MOF-177 which has large ellipsoidal pores with a short axis of 11 Å and a long axis of 19 Å. The absolute hydrogen uptake at 77 K and 2 MPa is shown in figure 3.44 in dependence

of the SSA. At 77 K hydrogen adsorbs on a monolayer on the surface as the temperature is well above the critical temperature of hydrogen which is 33 K. The density of the adsorbate at full coverage of the surface should be close to the density of liquid hydrogen. Therefore in figure 3.44 the amount of hydrogen contained in a monolayer

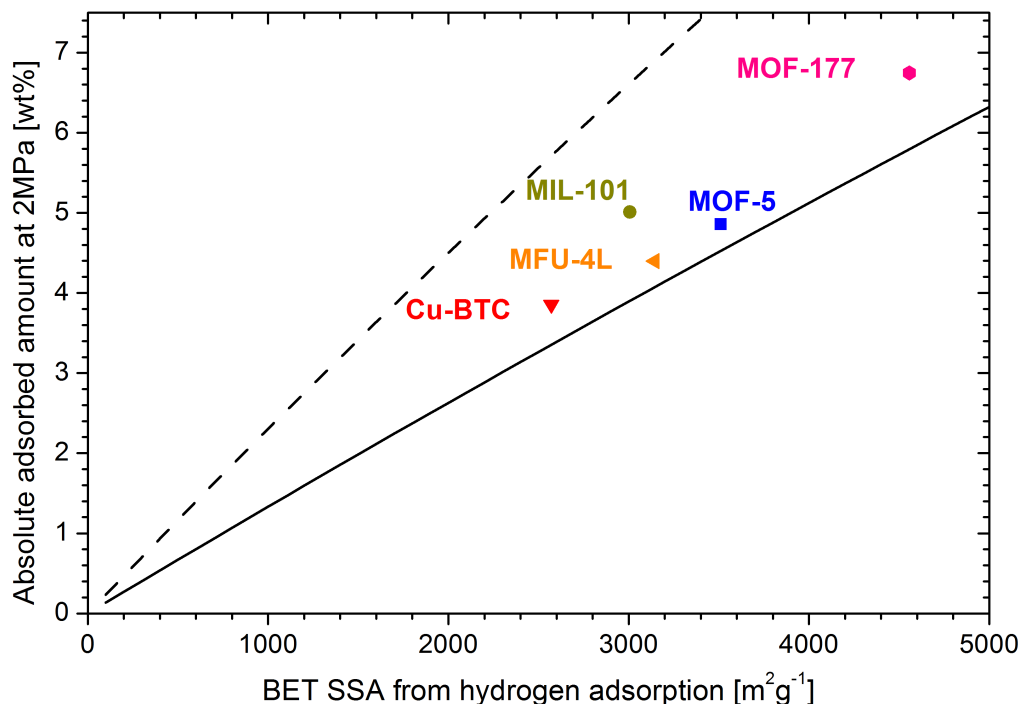


Figure 3.44: Absolute hydrogen uptake at 77 K and 2 MPa in dependence of the SSA determined by hydrogen adsorption at 19.5 K. The dashed and solid lines correspond to the hydrogen content in a liquid monolayer on the same area at the boiling point and the critical point, respectively.

with the density of liquid hydrogen on the surface is indicated. The dashed line corresponds to the density of hydrogen at the boiling point at 20 K and 0.1 MPa which is $3.5 \times 10^{-2} \text{ mol cm}^{-3}$ [71] and the solid line to hydrogen at the critical point at 33 K and 1.3 MPa which is $1.5 \times 10^{-2} \text{ mol cm}^{-3}$ [71].

All materials, show hydrogen uptakes that are between these two lines. As the adsorption isotherms have not reached saturation at 77 K and 2 MPa, which would correspond to a full coverage of the surface area, the density of the adsorbed hydrogen is higher than for hydrogen at the critical point.

The maximum amount of adsorbed hydrogen at 77 K is determined by the SSA and the adsorbed hydrogen has a density which is higher than for liquid hydrogen at the critical point.

Specific and Accessible Surface area

The accessible surface area (ASA) is calculated geometrically from crystal data assuming a sphere rolled over the surface with the same diameter as the probe molecule. The ASA therefore reflects the surface area available for the probe molecule within a perfect single crystal. Owing to the quality of the sample this can be significantly different from the experimental SSAs. In figure 3.45 the ASAs (dashed) and SSAs (solid) of the investigated supermicroporous and mesoporous materials are shown for nitrogen, argon and hydrogen. For most materials the ASA increases from nitrogen to argon and hydrogen, which is

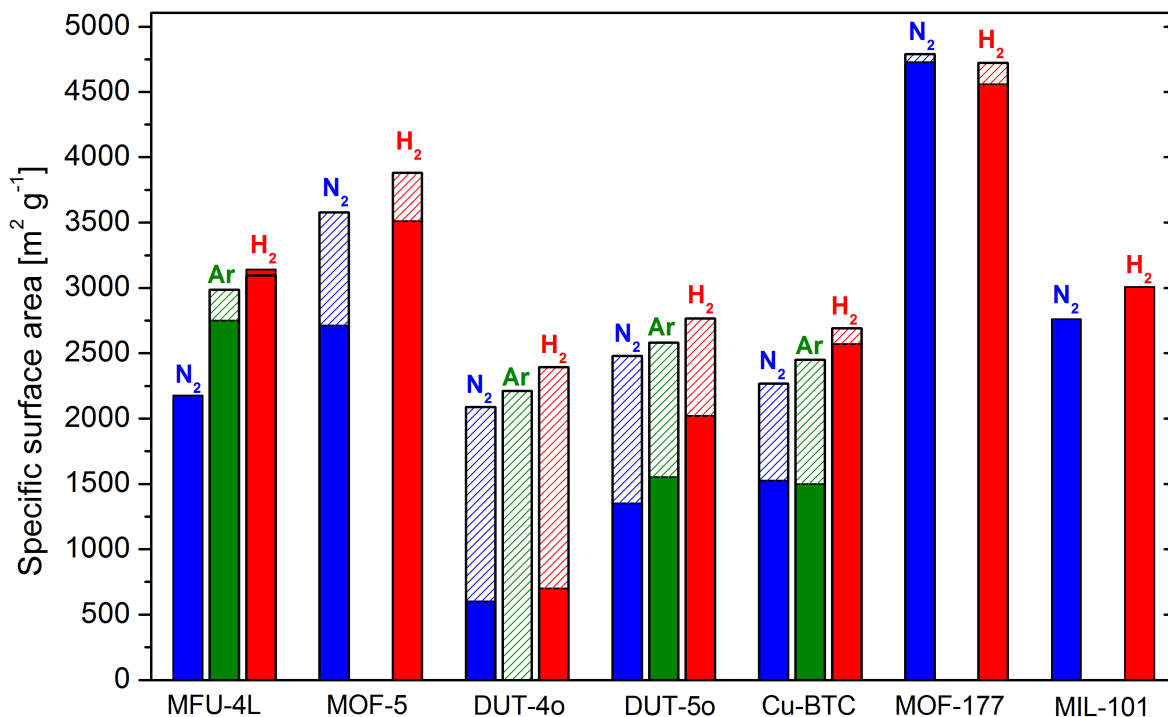


Figure 3.45: Specific (solid) and accessible (dashed) surface areas of MOFs determined by nitrogen, argon, and hydrogen.

also observed in the experimentally determined SSAs. Only for MOF-177 the ASA and SSA for nitrogen are larger than for the smaller hydrogen molecule. Therefore the SSA determined by nitrogen adsorption does not represent the surface area that is available to hydrogen molecules.

The difference of the SSA to the ASA is a measure of the quality of the investigated materials. MFU-4L and MOF-177 exhibit almost the SSA as expected from the ASA calculations. This indicates that their framework structure is well defined, all solvent molecules are removed and the framework is completely accessible to the gas molecules.

For MOF-5 the SSAs are 25 % and 12 % smaller than the ASA for nitrogen and hydrogen, respectively. This might be caused by the exposure of MOF-5 to air, which seems to influence the sample quality as reported by Kaye et al. [72]. For Cu-BTC the material quality seems to be very high according to the SSA from hydrogen adsorption, but nitrogen and argon yield a remarkable difference in the SSA from the ASA. DUT-4o and DUT-5o were partly decomposed at the time of the SSA measurements.

Overall these results indicate that the SSAs determined according to BET theory in the pressure range suggested by Rouquerol et al. [37] represent well the surface available to the gas molecules. This was reported before by Düren et al. [73] where the ASA was compared to the SSAs from experimental and simulated (GCMC) adsorption isotherms. The SSAs from simulated adsorption isotherms agreed with the ASA directly calculated from the framework structure, while the SSAs from experimental isotherms were for some materials remarkably smaller owing to the quality of the material.

Hydrogen storage materials are most often characterized by their SSA from nitrogen adsorption. As shown in figure 3.45, this does not correspond to the surface area which is available for the hydrogen molecules. Therefore it would be more adequate to determine the surface area by hydrogen adsorption at 20 K than by nitrogen adsorption at 77 K, but owing to the experimental complexity it is a convenient approximation to determine the SSA accessible for hydrogen by nitrogen adsorption.

Adsorption Sites

In figure 3.46 a Langmuir adsorption isotherm is shown with color indicating the different regions of the isotherm. At very low pressure first the linear Henry region is observed which is indicated in orange. With increasing pressure there is a strong derivation from linearity (blue and green triangles). In the pressure region indicated in green, the last available adsorption sites become occupied and the monolayer is completed. At higher pressure the amount adsorbed remains constant (red squares) as in the Langmuir model no multilayer adsorption is included. When increasing the value of b (equation 2.10), which corresponds to and increase in the interaction strength of the gas molecules with the surface, the elbow of the isotherm is more pronounced (gray triangles up). In contrast a lower interaction strength leads to a less pronounced curvature (gray triangles down). To get more information about the low pressure region, isotherms are plotted in a logarithmic pressure scale. The Langmuir isotherms of figure 3.46 are shown in figure 3.47 in a logarithmic pressure scale. In this representation the linear Henry region at very low pressure and its linear fit (red line) are emphasized. The blue region where the uptake does not correlate linear to the pressure anymore, appears as linear region in the semi-logarithmic representation. Like in the linear representation, the elbow of the isotherm (green) exhibits a stronger curvature in the semilogarithmic presentation. Saturation is observed in the semi-logarithmic scale, but occupies only a small fraction of the width of the graph. Increasing and decreasing the interaction strength does not change the shape of the isotherm in this representation, but shifts the isotherm to lower and higher pressure, respectively.

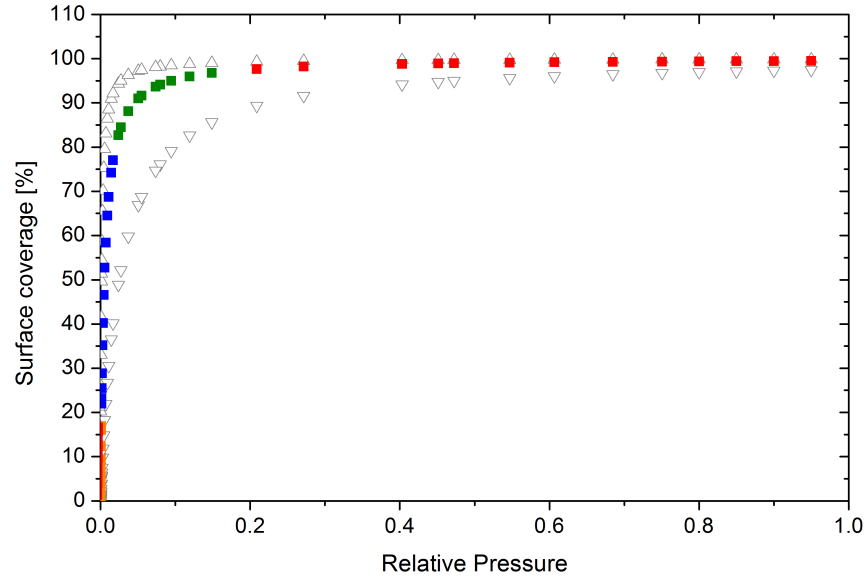


Figure 3.46: Langmuir adsorption isotherms. The linear Henry region is indicated in orange, the elbow in green and the saturation in red. Triangles up and down indicate adsorption isotherms with increased and decreased interaction strength, respectively.

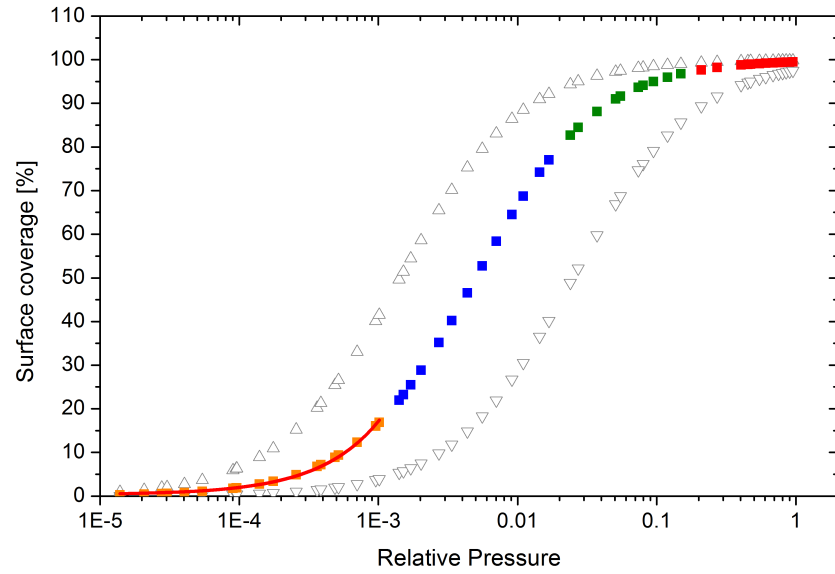


Figure 3.47: Langmuir adsorption isotherms in a logarithmic scale. The linear Henry region is indicated in orange, the elbow in green and the saturation in red. Triangles up and down indicate adsorption isotherms with increased and decreased interaction strength, respectively.

Assuming that an adsorbent has two distinct adsorption sites with different adsorp-

tion potential which are filled successively, the adsorption isotherm would be a sum of two adsorption isotherms. The height of the isotherm is determined by the number of available adsorption sites, while the position in the semi-logarithmic scale is determined by the interaction strength. If the two sites have a big difference in the interaction potential a step like behavior of the adsorption isotherm should evolve.

Experimentally this was observed for different gases before e.g. in Cu-BTC for argon at 87 K by Vishnyakov et al. [28] and for nitrogen at 77 K by Krawiec et al. [27]. The two steps in the adsorption isotherm were assigned to first filling of the small 5 Å pore followed by adsorption in the larger 9 Å pore. Step-like behavior is also observed for the hydrogen adsorption isotherms at 19.5 K reported in figure 3.29-3.35.

MFU-4L

The adsorption isotherm of MFU-4L exhibits three steps, the first one is small and has a hydrogen uptake of $70 \text{ cm}^3 \text{ g}^{-1}$ and is followed by two steps of comparable height with approximately $500 \text{ cm}^3 \text{ g}^{-1}$. The structure of MFU-4L (figure 2.11) offers a variety adsorption sites. The strongest adsorption sites are expected to be located close to the metal cluster in the large pore and the exposed chlorine atoms in the small pore. In general the adsorption strength in the small pore is higher than in the large pore. Owing to the crystal structure the small and large pores have similar volume, the sphere which determines the diameter is smaller due to the chromium atoms sticking into the pore. Consequently, there are three energetically different adsorption sites in the framework, the metal clusters, the small and the large pore. The three steps observed in the adsorption isotherm might be correlated to these sites. The metal centers offer strong adsorption sites but typically these sites are saturated by a few molecules per metal cluster. The small step at low hydrogen uptake is saturated at $70 \text{ cm}^3 \text{ g}^{-1}$ which corresponds to 4 hydrogen molecules per metal cluster. Therefore one hydrogen molecule could be located close to each chlorine atom which are the corners of the small pore or in the corners of the larger pore where the attraction from the three neighboring chlorine atoms overlap. The hydrogen uptake assigned to the metal centers is indicated in figure 3.48 in light blue. The next two steps in the adsorption isotherm are of similar height which indicates two adsorption energies with approximately the same number of adsorption sites available. Analogue to the observations made by Vishnyakov et al. [28] and Krawiec et al. [27] in Cu-BTC, these adsorption potentials are assigned to the small and large pore. In figure 3.48 this is indicated by orange and yellow according to the small and large pore.

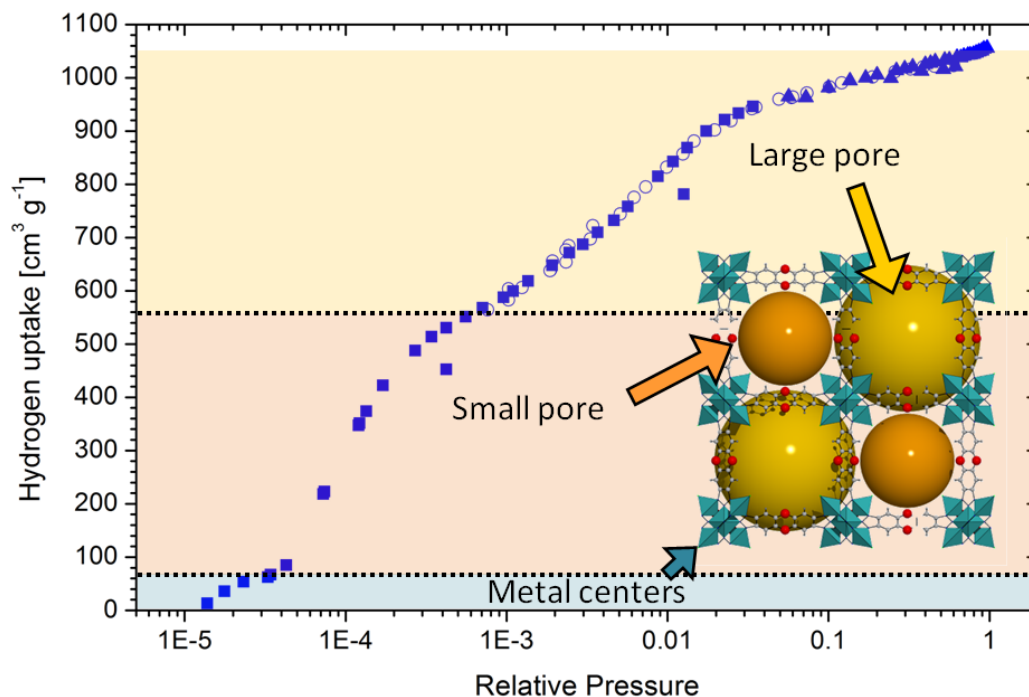


Figure 3.48: Steps in the hydrogen adsorption isotherm of MFU-4L at 19.5 K are correlated to the framework topology.

MOF-5

For MOF-5 (figure 3.2.3) at 19.5 K four steps are observed, which indicates at least four different adsorption sites. Yildirim and Hartman [54] investigated the adsorption sites in MOF-5 on different deuterium loadings by neutron powder diffraction along with first principle calculations. They identified nine different adsorption sites that are shown in figure 3.49. The strongest adsorption site **1** is between the three zinc-tetrahedra, which is located in the corner of the large pore. This is followed by adsorption site **2** which is on top of the zinc-tetrahedra and therefore in the corner of the small pore. Both adsorption sites can be loaded with four hydrogen molecules per metal cluster. The next two adsorption sites are filled simultaneously with 18 hydrogen molecules. One site is located in the corner of the windows **3** and the other **4** on top of the aromatic ring which is basically the edge of the window shifted into the larger pore. These adsorption sites identified by Yildirim and Hartman by neutron powder diffraction were also determined by ab initio calculations by Mulder et al. [74]. According to Yildirim and Hartman, the next eight hydrogen molecules are adsorbed in site **5** and **6** that are in the plane of the aromatic ring within the small pore. When increasing the hydrogen loading up to 46 hydrogen molecules per metal center, site **5** and **6** saturate and site **7-9** start to adsorb hydrogen, which are located in the large pore. Yildirim and Hartman

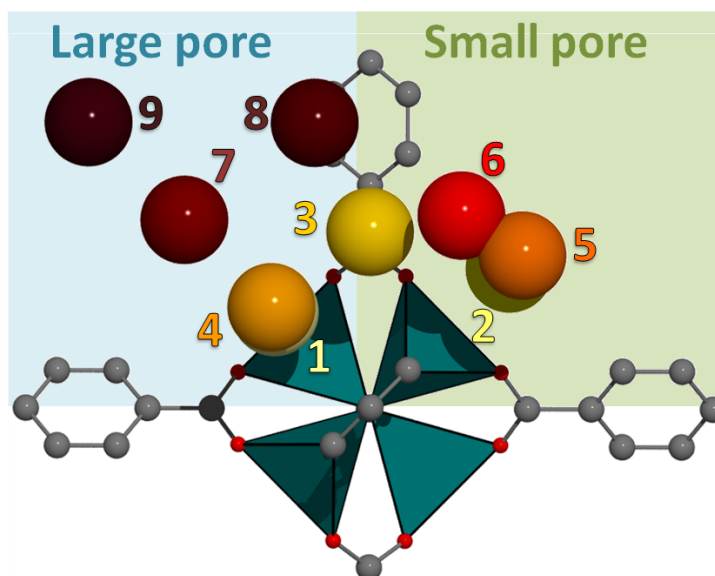


Figure 3.49: Adsorption sites in MOF-5 according to Yildirim and Hartman [54].

observed a maximum hydrogen uptake of MOF-5 of 11 wt% which is approximately 25 % higher than the uptake reported in figure 3.2.3. Therefore to compare the adsorptions sites occupied to the hydrogen adsorption isotherm measured at 19.5 K the uptake is normalized to the maximum hydrogen uptake observed for the investigated MOF-5. In figure 3.50 the hydrogen adsorption isotherm measured at 19.5 K is correlated to the adsorption sites identified by Yildirim and Hartman. The strongest sites (**1** and **2**) each adsorb 9 % of the maximum hydrogen uptake which corresponds to $96 \text{ cm}^3 \text{ g}^{-1}$. In the hydrogen adsorption measurement the first step is observed at a hydrogen uptake of approximately $200 \text{ cm}^3 \text{ g}^{-1}$. This corresponds to saturation of both adsorption sites close to the metal center (**1** and **2**). Saturation of site **1** cannot be resolved from site **2**. Sites **3** and **4** which are located in the windows are filled simultaneously according to Yildirim and Hartman and get saturated at an uptake of 26 hydrogen molecules per metal center which corresponds to $622 \text{ cm}^3 \text{ g}^{-1}$. This is observed in the adsorption measurement by the second step, which is saturated at approximately that uptake. Up to a loading of 34 molecules per metal center, which correspond to $813 \text{ cm}^3 \text{ g}^{-1}$, hydrogen is adsorbed in the small pore (site **5** and **6**) and at higher pressure in the large pore (site **7**, **8**, and **9**). The small pore can therefore be assigned to the first small step and the large pore to the final step.

For comparison of the 19.5 K adsorption isotherm to isotherms at higher temperature, the uptake is shown in dependence of the relative pressure in a logarithmic scale (figure 3.2.3). The relative pressure is used as this presents a relative density of molecules which is the density normalized to the density of the liquid. In this representation, at 25.5 K the isotherm is identical to the adsorption isotherm at 19.5 K up to an uptake of approx-

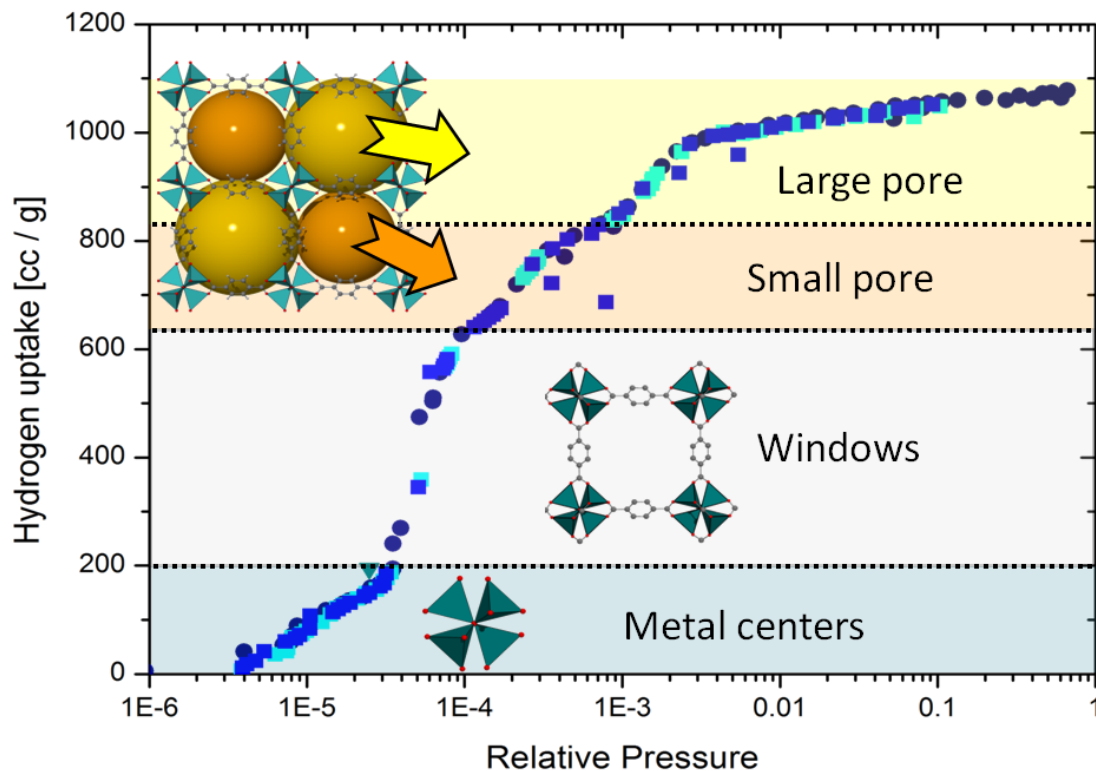


Figure 3.50: Steps in the hydrogen adsorption isotherm of MOF-5 correlated to the adsorption sites identified by Yildirim and Hartman [54] from neutron powder diffraction.

imately $600 \text{ cm}^3 \text{ g}^{-1}$ which includes the region of adsorption close to the metal centers and in the windows. At higher pressure, corresponding to adsorption in the pores, the isotherm is shifted to higher relative pressure. At 31.0 K the isotherm is identical only up to approximately $200 \text{ cm}^3 \text{ g}^{-1}$, which corresponds to adsorption at the metal centers, and then shifts to higher pressure. For simplification, we assume that the MOF offers three major adsorption sites, the metal centers, the windows, and the pores. The observation made in this measurement indicates that for molecules adsorbed at the two stronger sites there is no difference between 19.5 K and 25.5 K. Whereas for the weakest adsorption site the pressure needed to reach a certain uptake is increasing. This can be explained using figure 3.51 which schematically shows the three major adsorption sites. At 25.5 K the thermal energy of the hydrogen molecules is higher than the adsorption potential of the weak adsorption site but lower than for the intermediate site. Therefore molecules adsorbed in the strong sites are adsorbed as for 19.5 K independent of the pressure, while higher pressure is needed to yield the same uptake in the weak adsorption site. When increasing temperature to 31.0 K the thermal energy of the molecules is big enough to overcome the intermediate adsorption potential. Therefore adsorption in this site is also shifted to higher pressure, but the adsorption at the metal center remains the same.

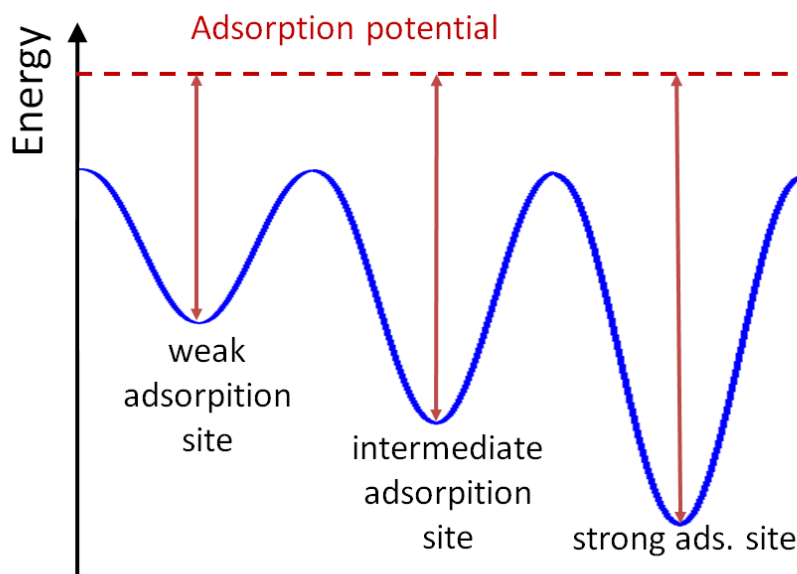


Figure 3.51: Sketch of the adsorption potential of the three major adsorption sites in MOF-5.

DUT-4o and DUT-5o

For DUT-4o the hydrogen adsorption isotherm at 19.5 K (figure 3.31) shows a typical type I behavior as shown in figure 3.47 where saturation is reached at a relative pressure of 3×10^{-4} , afterwards the uptake increases slowly by $50 \text{ cm}^3 \text{ g}^{-1}$. This indicates that there is only one adsorption site. For DUT-5o two steps in the semi-logarithmic representation are observed (figure 3.32). The maximum hydrogen uptake of DUT-5o is with $550 \text{ cm}^3 \text{ g}^{-1}$ almost double the uptake of DUT-4o. In figure 3.52 adsorption of DUT-4o and DUT-5o is normalized to the uptake of the stronger adsorption site. In this representation, the adsorption of both materials is identical up to the saturation of the stronger adsorption site at a relative pressure of 3×10^{-4} . This indicates that the adsorption potential of the strongest adsorption sites is the same for DUT-4o and DUT-5o. At higher pressure DUT-5o exhibits a second step, whereas DUT-4o is just slowly increasing. Therefore, DUT-5 seems to have a second less strong adsorption site. The strong adsorption site which has the same adsorption enthalpy in both compounds might be located in the corners of the channels. DUT-5o which has a longer linker might have a second adsorption site at the linker. This filling of the second adsorption site in DUT-5o is observed in figure 3.52 by the additional step compared to DUT-4o.

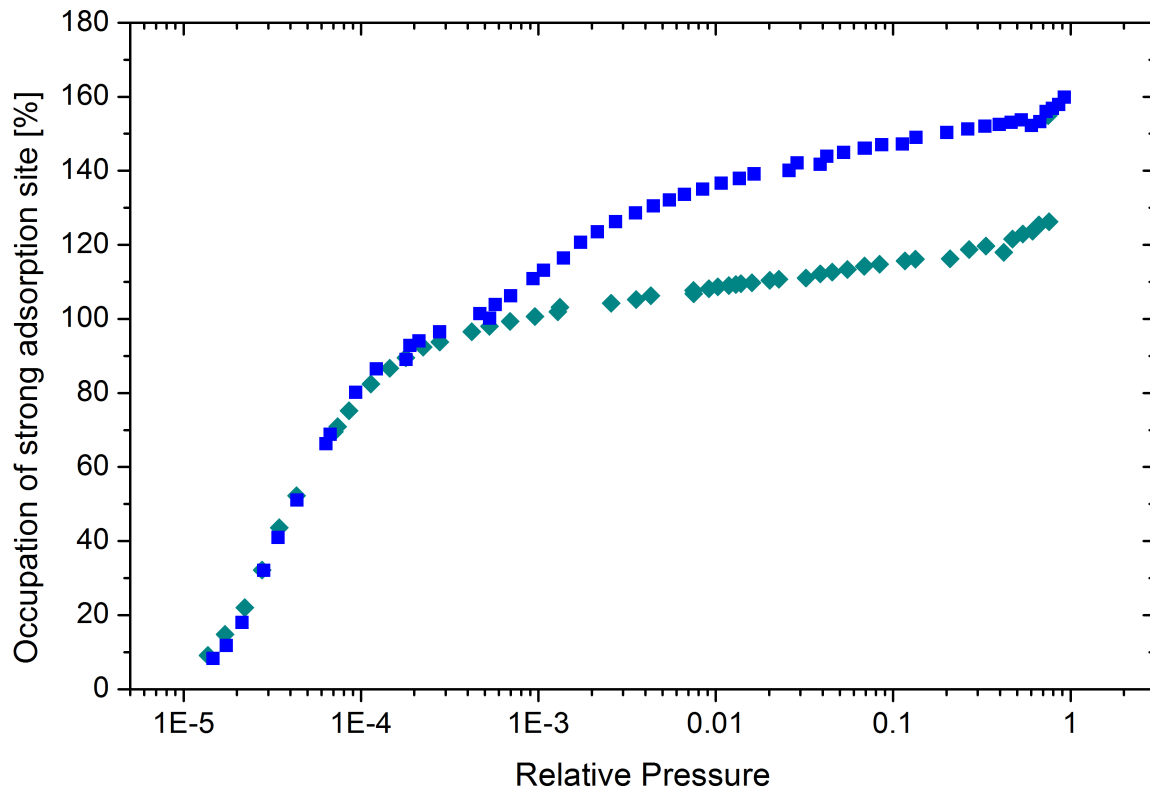


Figure 3.52: The hydrogen adsorption isotherms of DUT-4 (squares) and DUT-5 (diamonds) at 19.5 K normalized to the hydrogen uptake of the strongest adsorption site.

Cu-BTC

For Cu-BTC Vishnyakov et al. [28] observed steps in the low pressure adsorption isotherm of argon at 87 K as later Krawiec et al [27] for nitrogen at 77 K. These steps were assigned to adsorption in the small pore, followed by adsorption in the large pore. For hydrogen at 19.5 K only a small second step above a relative pressure of 0.1 is observed. As the interaction strength for hydrogen is different from the interaction strength of argon or nitrogen, the two adsorption steps for the small and the large pore might overlap in contrast to the observations made by Vishnyakov et al. [28] and Krawiec et al [27] for nitrogen. By neutron powder diffraction Peterson et al. [58] identified adsorption sites for hydrogen in Cu-BTC at 5 K and different loadings. The strongest adsorption site is offered by the unsaturated metal cluster and is filled first. The next strong adsorption site is the small side pocket. Below a hydrogen uptake of one hydrogen molecule per copper atom, which corresponds to $111 \text{ cm}^3 \text{ g}^{-1}$ only these sites are occupied. With increasing loading these sites get further occupied and a third adsorption site starts to adsorb which is within the window of the small side pocket. These three sites are saturated at a loading of two hydrogen molecule per copper atom. This is the first saturation that is within the measured range of hydrogen uptake at 19.5 K (figure 3.53

where the sites are number according to decreasing adsorption strength). In the adsorption isotherm a small step is observed at that uptake. With increasing pressure the three other adsorption sites, two in the large pore and one in the small pore, start to adsorb. The highest hydrogen uptake investigated by Peterson et al. corresponds to $460 \text{ cm}^3 \text{ g}^{-1}$

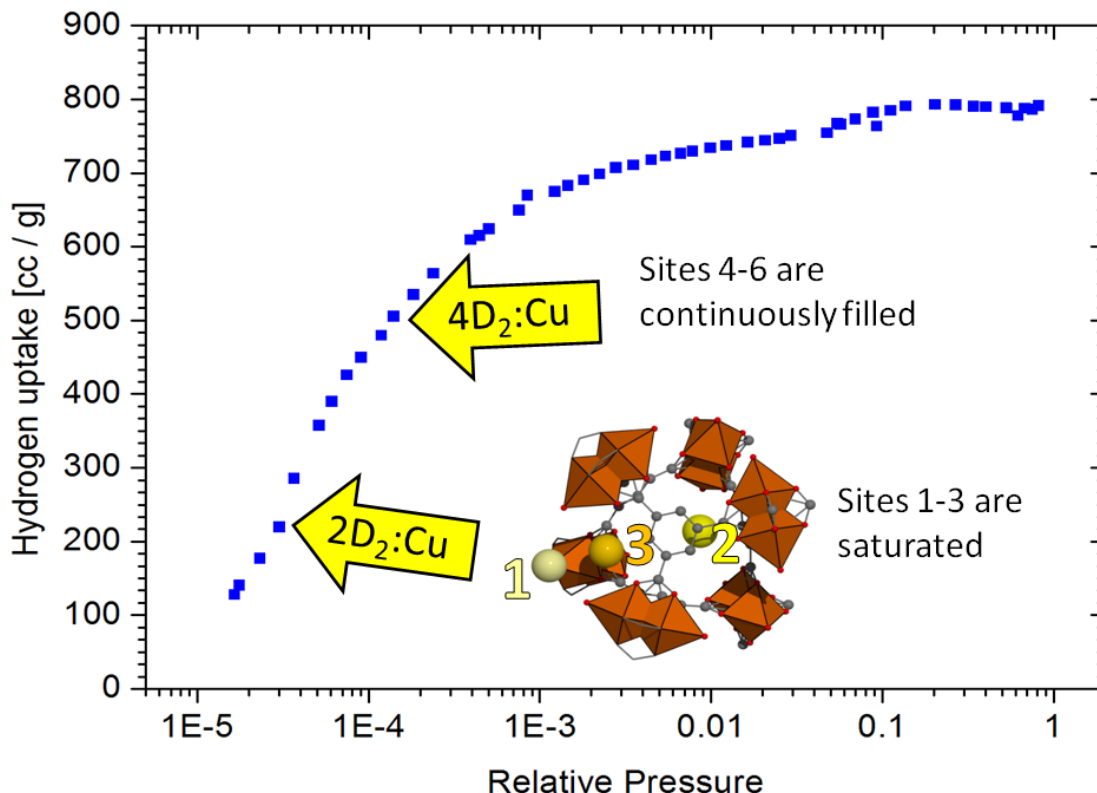


Figure 3.53: Hydrogen adsorption isotherm of Cu-BTC at 19.5 K and indication of the adsorption sites identified by Peterson et al. [58].

(3.9 wt%). At this uptake all three weak adsorption sites (4-6) are occupied, but not saturated yet. In a later publication Peterson et al. [75] identified three further adsorption sites and determined their population up to a loading of 6.5 molecules per copper atom (5.7 wt%). Interestingly three adsorption sites are only intermediate sites that are depopulated when reaching higher uptake. The hydrogen uptake of the small pore and larger pore overlap. For the adsorption isotherm this overlap is also observed, as no step can be resolved between $230 \text{ cm}^3 \text{ g}^{-1}$ and $747 \text{ cm}^3 \text{ g}^{-1}$. In the adsorption isotherm a small step at relative pressure of 0.1 is observed. The hydrogen uptake before this step agrees with the maximum hydrogen uptake measured by Peterson et al. [75] of 5.7 wt% which corresponds to $747 \text{ cm}^3 \text{ g}^{-1}$. The high pressure at which the step occurs is typical for adsorption in mesopores. Concerning the framework structure there should not be any large pores present in the framework, but taking a look at the SEM image (image 2.17) indicates that there are large mesopores in the framework. The filling of these

pores results in the high pressure step of the adsorption isotherm.

MOF-177

MOF-177 consist of the same metal cluster as MOF-5, which is Zn_4O . Therefore the adsorption sites offered by the metal center should be identical for both compounds. As calculated by Yildirim and Hartman [54] the metal cluster adsorbs eight hydrogen molecules. As one formular unit of MOF-177 is heavier than for MOF-5 this corresponds to a weight specific hydrogen uptake of the framework of $160\text{ cm}^3\text{ g}^{-1}$. By inelastic neutron scattering on MOF-177 loaded with different quantities of hydrogen, Rowsell et al. [76] also identified two adsorption sites close to the metal center which get saturated at an hydrogen uptake of 8 molecules per formula unit. At higher hydrogen uptake they observed at least two more overlapping adsorption sites at the linker which are not saturated up to the maximum hydrogen uptake investigated which was 48 hydrogen molecules per formula unit. Owing to the great complexity in the structure of MOF-177 many different adsorption sites are expected that might overlap strongly. In the hydrogen adsorption isotherm there is indication for two strong adsorption sites adsorption site.

MIL-101

MIL-101 has a trimodal pore size distribution of 7 Å, 29 Å, and 34 Å, which should lead to at least three major adsorption sites with different adsorption enthalpy. In the adsorption isotherm two distinct steps are observed. The volume and surface area of the side pockets to the 29 Å-pore to the 34 Å-pore are approximately 1:8:7 and 2:4:3, respectively. Therefore assuming monolayer adsorption, the maximum hydrogen content expected in the small pore is 22% of the total uptake and when regarding pore filling, which is more appropriate below the critical temperature, it is even only 6%. Therefore, adsorption in these small side pockets, which is supposed to occur first, will be observed below a hydrogen uptake of $75\text{ cm}^3\text{ g}^{-1}$ or $267\text{ cm}^3\text{ g}^{-1}$ considering the volume or surface fraction, respectively. The scatter in this low pressure region is too strong to clearly resolve a step. The adsorption in the side pockets overlaps with the adsorption in the pore, which continues up to relative pressure of about 10^{-2} . At higher pressure the adsorption increases again stronger due to the filling of the larger 34 Å pore. The ratio of the amount of hydrogen adsorbed in the side pockets and the 29 Å pore to the 34 Å pore is determined to approximately 8:5, which is close to both their volumetric ratio (9:7) and their surface area ratio (2:1). A successive filling of adsorption sites in MIL-101 was predicted by simulation of CO_2 and CH_4 at 303 K by Chen et al. [77]. At a pressure below 10 kPa CO_2 and CH_4 adsorb only in the small side pockets but when increasing the pressure these adsorption sites are getting saturated and molecules are adsorbed in the larger pores which is analogue to the observed adsorption steps. In figure 3.54 the adsorption isotherm of MIL-101 at 19.5 K is shown and the region of uptake for the different adsorption sites are indicated according to their volumetric ratio.

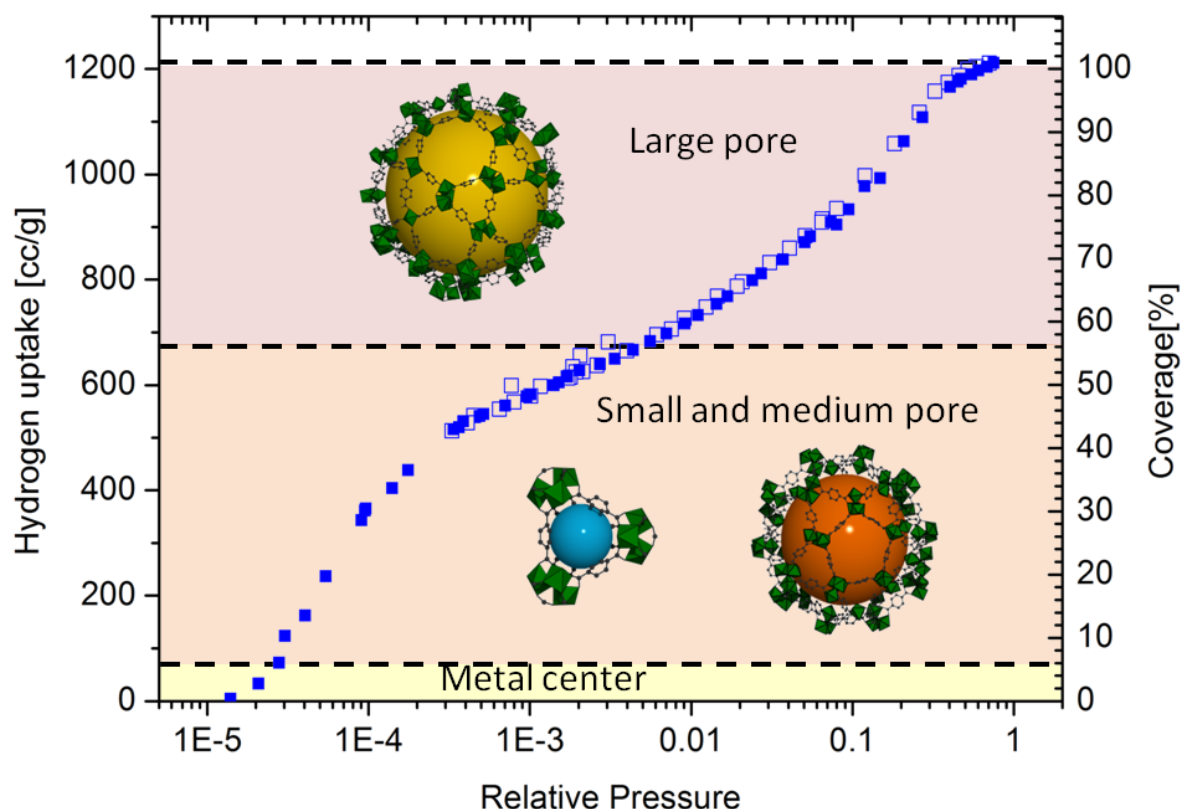


Figure 3.54: Adsorption sites in MIL-101 correlated to the adsorption isotherm at 19.5 K according to their volumetric ratios. Adsorption is indicated by the filled symbols, desorption by open symbols.

Gating effects

The ultramicroporous frameworks Mg-formate and MFU-4 have pores with a diameter similar to the kinetic diameter of a hydrogen molecule. In Mg-formate channels with a diameter of 3.4–4.6 Å are observed and MFU-4 has alternating pores of 3.88 Å and 12 Å. As discussed in section 3.1.4 the kinetics and enthalpy of adsorption of MFU-4 are governed by the small pores. Owing to the small pore size nitrogen at 77 K cannot penetrate into both ultramicroporous frameworks and therefore the SSA cannot be determined. At 77 K the smaller hydrogen molecules can penetrate both frameworks which is observed by hydrogen uptakes of 1.17 wt% and 2.58 wt% for Mg-formate and MFU-4, respectively. At 19.5 K Mg-formate and MFU-4 adsorb only 0.05 wt% and 0.14 wt%, respectively, which is within the experimental uncertainty of 0.4 cm³.

In figure 3.42 a kinetic measurement of hydrogen adsorption of MFU-4 is shown. The sample holder was loaded at room temperature with 800 mmHg (0.11 MPa) and then cooled to 30 K within a few minutes. When the sample holder reached 30 K and the

temperature remained constant within ± 2 K the pressure in the sample holder was 320 mmHg. Pressure changes due to the temperature dependence of the density of the gas were finished before the kinetic measurement started. The pressure was monitored over 15 min and remained constant within ± 2 mmHg. Similar observations were made for heating to 40 K and 50 K where the pressure remained constant over 15 min at 358 mmHg and 383 mmHg. At 60 K the pressure was decreasing slowly from 399 mmHg to 391 mmHg within the 15 min observed. At 70 K the pressure was also 399 mmHg when the kinetic measurement started and decreased to 365 mmHg after 20 min observation time. This indicates that hydrogen is slowly adsorbed at 60 K and 70 K and that the equilibrium is not reached within 15 min. At 80 K the pressure is 418 mmHg and increases by 5 mmHg within the observation time which is caused by temperature fluctuations of ± 3 K in the sample holder. These measurements indicate that there are three different temperature regions for hydrogen adsorption on MFU-4: Below 50 K, between 60 K and 70 K, and above 80 K.

In figure 3.41 the pressure in the sample holder and the hydrogen uptake is shown in dependence of the temperature for MFU-4. In this measurement the same regions are identified as in the kinetic measurement. Below 50 K the hydrogen uptake remains constant, up to 70 K the uptake is increasing with increasing temperature and above 70 K it is decreasing with temperature. In contrast the supermicro- and mesoporous materials (figure 3.37-3.39) show a temperature and pressure dependence which was expected for hydrogen adsorption. For these materials at low temperature the hydrogen uptake remains constant with increasing temperature as all hydrogen present in the sample holder is adsorbed. With increasing temperature the material starts to desorb hydrogen and the pressure is increasing. For MFU-4 the measurement of hydrogen uptake and pressure in dependence of the temperature shows a completely different adsorption behavior. The amount of hydrogen adsorbed below 50 K remains constant but then an increase in hydrogen uptake is observed at the same temperature as the pressure starts to decrease in the kinetic measurement. Therefore below 50 K the constant pressure in the kinetic measurement indicates that hydrogen cannot penetrate into the framework and the amount adsorbed which is observed in the pressure dependent measurement corresponds to hydrogen that was adsorbed during cooling from room temperature to 50 K. This is also observed in the isothermal measurement at 19.5 K where MFU-4 adsorbs only 0.14 wt%, which is below the experimental uncertainty. At 60 K hydrogen is able to diffuse slowly into the framework, therefore the pressure in the kinetic measurement is decreasing slowly and the uptake is higher than at 50 K. At 70 K the diffusion is faster and therefore the adsorbed amount is higher than at 60 K. At 80 K the hydrogen uptake is decreasing with temperature as observed for the supermicro- and mesoporous materials. Therefore the constant pressure in the kinetic measurement indicates that adsorption equilibrium was reached before the temperature settled and the kinetic measurement was started. This is also observed in the isothermal measurement at 77 K where a remarkable hydrogen uptake of up to 2.58 wt% at 2 MPa is observed for MFU-4. Furthermore the hydrogen uptake and pressure was measured for slow cooling starting from 84 K (figure 3.41). The hydrogen uptake increases with decreasing temperature from 84 K to 50 K. At lower temperature it remains constant. This supports the inter-

pretation that the diffusion of hydrogen is hindered at low temperature and therefore it remains constant. If the sorption properties of MFU-4 was due to structural changes in the framework, the hydrogen uptake observed in the first heating cycle would be reversible. In a second heating cycle the hydrogen uptake remains constant up to 55 K and then decreases slowly with temperature as observed for the super- and mesoporous materials.

For the other ultramicroporous MOF, Mg-formate, the hydrogen uptake and pressure in dependence of the temperature is shown in figure 3.40. The sorption behavior is very similar to the observations made for MFU-4.

The untypical sorption behavior of the ultramicroporous Mg-formate and MFU-4 at cryogenic conditions therefore originates clearly from a kinetic hindrance of the hydrogen molecules to enter the frameworks at temperatures below 50 K.

Similar observations were made for nitrogen within Mn-formate by Kim et al. [78]. By a slightly different synthesis they composed a Mg-formate that was able to adsorb nitrogen and showed the expected decrease in nitrogen uptake with increasing temperature. Even though from the crystallographic data Mn-formate was expected to have larger channels than Mg-formate, it did not adsorb any nitrogen at 77 K. With increasing temperature it started to adsorb remarkable amounts of nitrogen with a maximum at approximately $T_{max\ uptake} = 143$ K. At higher temperature the nitrogen uptake decreases with increasing temperature. Similar behavior was observed for argon uptake in Mn-formate. Kim et al. showed by single crystal X-ray analysis that there is no transition in the framework structure, owing to the temperature, including cell parameters and pore size. Therefore the untypical sorption properties are not based on a phase transition of the framework. They assume that the observed gate opening for adsorption is due to large amplitude lattice vibrations and/or to kinetic hindering as the thermal energy is not large enough to overcome diffusion barriers within the framework. Analogue observations and conclusions were recently made by Lin et al. [79] for nitrogen in a manganese framework and Lee et al. [80] for the aromatic compound trimethylbenzene in MIL-96.

From the measurements it cannot be distinguished if diffusion barriers, framework vibrations, or both cause this diffusion problem as pointed out by Kim et al. [78].

3.3 MOFs in hydrogen storage applications

Hydrogen is a promising energy carrier for the future [1, 2], whereas physisorption of hydrogen on MOFs is one of the favored possibilities to store hydrogen for mobile application [3, 4]. In a hydrogen storage system the total amount of hydrogen which is present in the system is of interest and not the amount of hydrogen which is there owing to physisorption. The total hydrogen uptake is calculated from the excess hydrogen uptake plus the amount which is present in the gas phase according to section 2.1.2, using the SPV determined in section 3.2.3. The uptake of the investigated materials for which the SPV was determined, is shown in figure 3.55 in mg hydrogen per g material. As the density of the gas phase is continuously increasing, no saturation is observed and

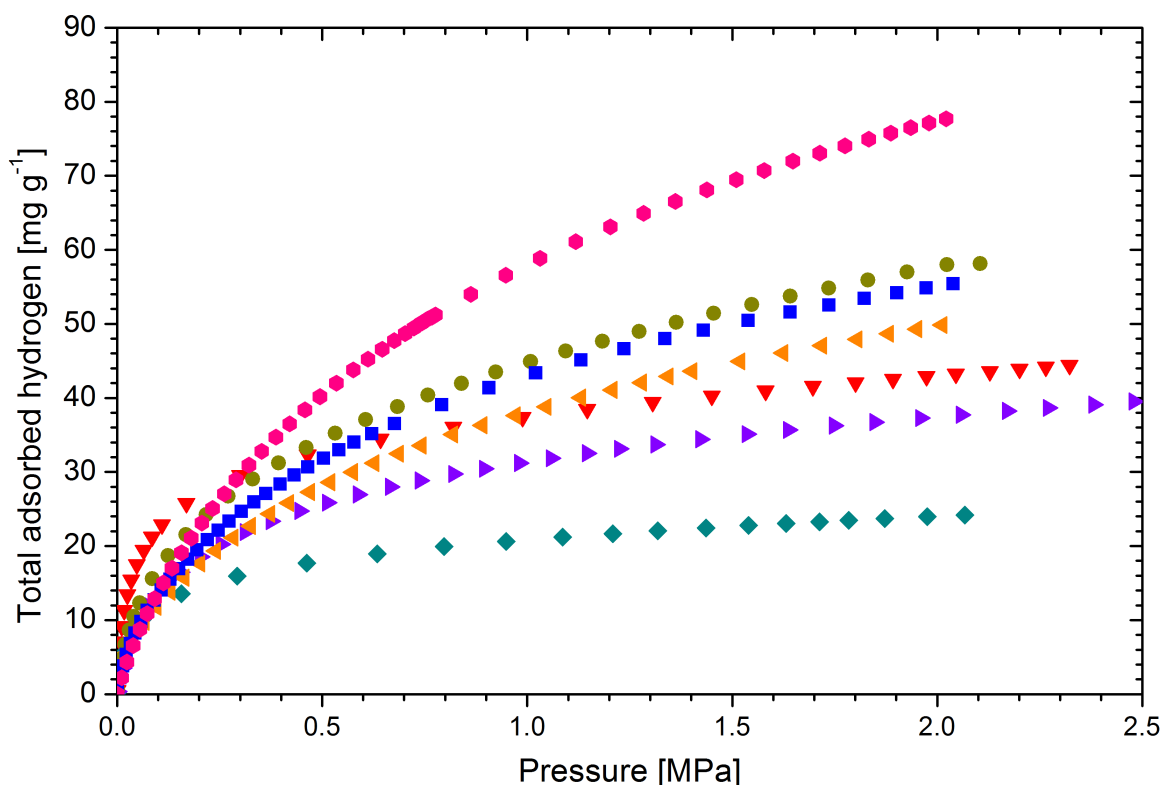


Figure 3.55: Total hydrogen adsorbed at 77 K in dependence of the pressure for \square MOF-5, \circ MIL-101, ∇ Cu-BTC, \diamond DUT-4, \triangleright DUT-5, \circ MOF-177, and \triangleleft MFU4L.

the isotherms increase linearly with pressure above approximately 1 MPa. The materials with the largest SPVs, which are MOF-177, MIL-101, MOF-5, and MFU-4L, show the highest total hydrogen uptake on gravimetric basis. For DUT-4 and DUT-5 the difference in excess and total uptake is very small which reflects the small SPV due to partial framework decomposition. For a storage system it is furthermore important how much hydrogen can be stored per volume. In figure 3.56 the total amount of hydro-

gen stored at 77 K and 2 MPa on volumetric basis is therefore correlated to the amount stored on gravimetric basis. The volumetric hydrogen uptake is calculated using the

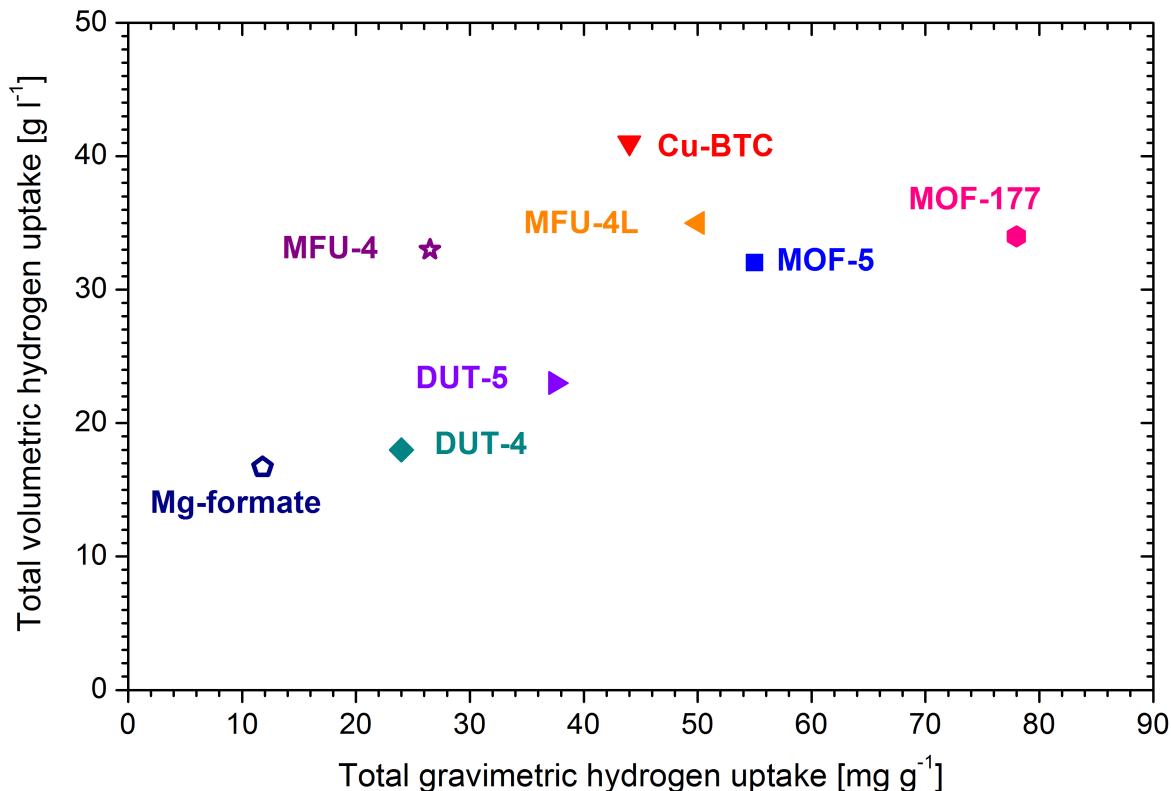


Figure 3.56: Total volumetric and gravimetric hydrogen uptake at 2 MPa and 77 K. For MFU-4 and Mg-formate excess hydrogen uptake under these conditions is shown.

density of a single crystal calculated from the crystallographic structure. For MFU-4 and Mg-formate the excess values are shown, as the SPV can not be determined by hydrogen adsorption at 19.5 K and therefore the total uptake is not reported. Concerning volumetric hydrogen uptake, MFU-4 has a hydrogen uptake comparable to MOF-177 even though the gravimetric hydrogen uptake is only one forth. The volumetric density of hydrogen gas at 77 K and 2 MPa is 6 g l⁻¹ and the density of liquid hydrogen at the boiling point is 71 g l⁻¹. The use of MOFs increases the amount of hydrogen stored in the tank system to more than half the volumetric uptake of liquid hydrogen even though the temperature is remarkable higher with 77 K for adsorption instead of 20 K for the liquid.

For application it is not only important how much hydrogen can be stored in a tank, but how much hydrogen is released. In general the kinetics of hydrogen physisorption are very favorable for use in mobile applications as equilibrium is reached within seconds when the pressure is changed. Additionally up on loading and unloading the amount of

heat which is released or needed is very low.

For application in combination with a fuel cell, a certain back pressure is needed to drive the fuel cell and therefore the empty tank system will have a certain pressure, e.g. 0.1 MPa.

Therefore it is important to take a close look at the adsorption isotherms as not the total uptake is of interest but the difference between the total uptake at maximum loading pressure, determined by the tank design, and minimum back pressure. This results in a usable capacity [3] which represents the amount of hydrogen that can be used for application. In figure 3.57 the total adsorbed hydrogen in MOF-177 is shown in dependence of the pressure for different temperatures. The dashed lines indicate the

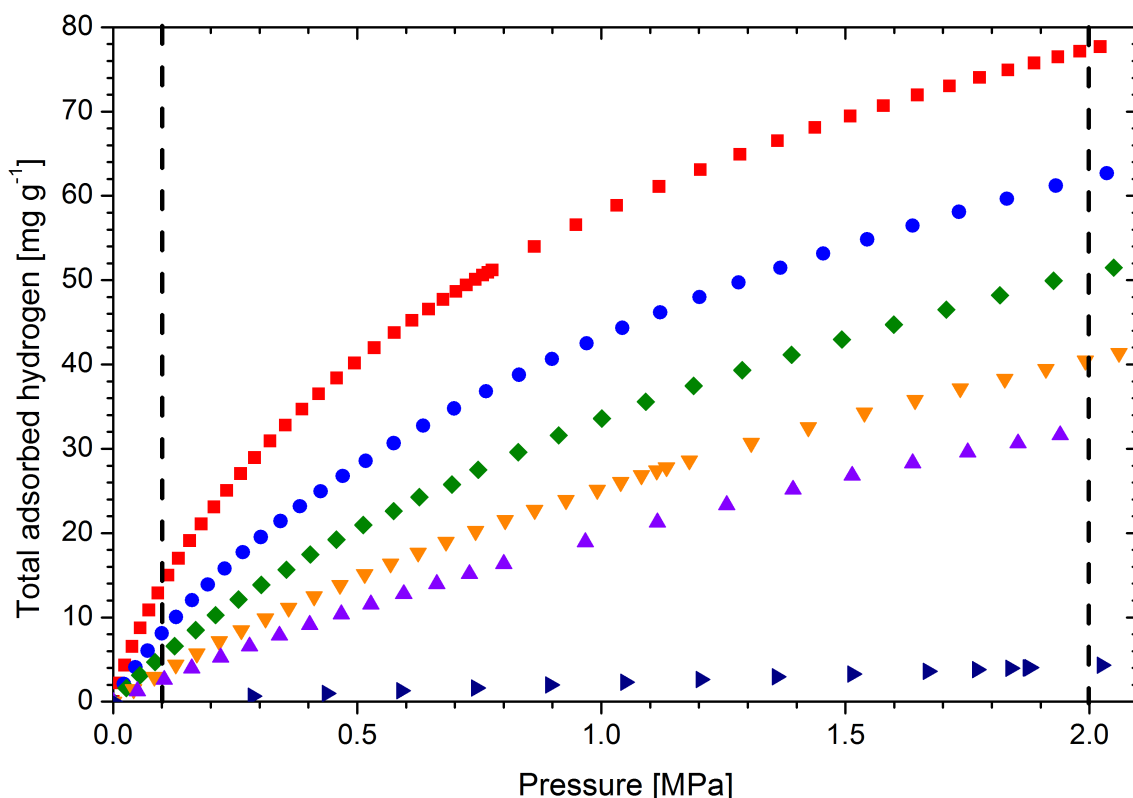


Figure 3.57: Total hydrogen adsorption isotherms of MOF-177 at \square 77 K (liquid N_2), \circ 87 K (liquid Ar), \diamond 97 K, ∇ 107 K, \triangle 117 K, and \triangleright 298 K. The dashed lines indicate the maximum loading pressure of 2 MPa and the minimum required back pressure of 0.1 MPa.

minimum back pressure and the maximum loading pressure which are assumed to be 0.1 MPa and 2 MPa, respectively. The usable capacity is determined by the difference between maximum uptake and minimum uptake. The maximum uptake depends on the specific surface area and the pore volume. In MOF-177 the high specific surface area and high specific pore volume lead to a high uptake of 78 mg g^{-1} at 77 K. The minimum hydrogen uptake at low pressure is determined by the enthalpy of adsorption. At low

pressure, a low enthalpy results in low uptake whereas a higher enthalpy results in a higher uptake. MOF-177 has a low adsorption enthalpy and therefore at 0.1 MPa and 77 K only 13 mg g⁻¹ are adsorbed. Therefore the usable capacity of MOF-177 at 77 K is 65 mg g⁻¹, which is under these conditions the highest useable capacity of all materials investigated.

Furthermore, the operating temperature of the storage system has a strong influence on the performance of the system. Increasing the temperature during unloading the tank yields a lower amount of hydrogen adsorbed at 0.1 MPa which results in a higher usable capacity. For example a rise in temperature of 40 K between loading at 77 K and complete discharging at 117 K increases the usable capacity for MOF-177 by 10 mg g⁻¹ to 75 mg g⁻¹.

Which material exhibits the highest usable capacity depends therefore strongly on temperature and pressure boundary conditions given by the application. A comparison of the hydrogen storage properties for two high surface area materials, MOF-177 and an activated carbon AX-21, was recently reported by Schlichtenmayer et al. [30]. Under the assumed conditions of loading at 77 K and 2 MPa, a minimum back pressure of 0.1 MPa, and a temperature increase of the tank of 40 K while unloading, MOF-177 has with 75 mg g⁻¹ the highest usable capacity of all materials investigated.

One of the drawbacks of storage of liquid hydrogen is that the tank needs to be an open-system to avoid dangerous over-pressurization. Even with strong isolation a small amount of heat is always transferred into the tank and therefore some of the liquid hydrogen evaporates and the pressure in the system increases. Therefore at some pressure a security valve is needed which is open to ambient to keep the pressure below a dangerous limit. The loss of hydrogen owing to this boil-off is approximately 0.3 – 1 % per day. The pressure change with increasing temperature is very strong when phase transition occurs from liquid to gaseous. This is observed in figure 3.36 for the black squares indicating the pressure in the empty sample holder. The volume of the system was kept constant and the temperature was increased. The pressure of the system increased by 400 mmHg owing to a temperature difference of only 1 K. In contrast for the sample holder containing some mesoporous or supermicroporous MOF material the pressure change with increasing temperature is much lower as observed in figure 3.37-3.39. If the amount of MOF present in the sample holder is able to adsorb all hydrogen in the gas phase, the increases in pressure can be even shifted to higher temperature by approximately 10 K. Therefore a tank system based on adsorption of gas in MOFs will have a much lower boil-off compared to a liquid hydrogen tank. Another possibility would be to combine MOFs with a liquid hydrogen tank. The MOFs would be cooled by liquid hydrogen and could adsorb the evaporated hydrogen and therefore lower the boil-off.

MOFs are very promising materials for hydrogen storage applications. The best MOF material for an application depends on the technical requirements. The correlation of framework structure to adsorption properties therefore enables the tailored synthesis of MOFs for different tank systems.

4 Summary

Hydrogen adsorption and desorption were measured on ten different materials from the new class of metal-organic frameworks (MOFs) with different chemical composition, surface areas up to $5000 \text{ m}^2 \text{ g}^{-1}$ and pore diameters between 3.4 \AA and 34 \AA . The materials are classified by their pore diameter as ultramicroporous (pore diameter less than 7 \AA), supermicroporous (pore diameter $7 - 20 \text{ \AA}$) and mesoporous (pore diameter greater than 20 \AA).

These materials were investigated in two fully automated Sieverts-type apparatus, one at high pressure up to 2 MPa and temperatures between 77 K and room temperature and the other at low pressure up to 0.1 MPa and temperatures around 20 K .

In the high pressure device the adsorption isotherms were measured at different temperatures which enables a very precise determination of the isosteric enthalpy of adsorption for hydrogen in the MOFs.

In the low pressure device hydrogen adsorption and desorption were measured for the first time at 19.5 K for MOF materials. Additionally the temperature dependence of hydrogen uptake and pressure was measured.

- The maximum hydrogen uptake of the investigated materials at 77 K and 2 MPa linearly correlates with the BET specific surface area of the materials determined by nitrogen adsorption. The maximum hydrogen uptake is independent of the chemical composition of the framework.
- The specific pore volume and the specific surface area, both determined by nitrogen adsorption at 77 K , correlate almost linearly. This indicates that nitrogen is only adsorbed in a monolayer on the surface as the space in the pore is too small to enable multilayer adsorption and that the measured surface area originates almost entirely from inner surface area of the material.
- The isosteric enthalpies of adsorption were correlated to the pore diameters. A clear trend to higher isosteric enthalpies of adsorption for materials with smaller pores is observed, which indicates that the enthalpy of adsorption is determined by the pore diameter. The highest enthalpies with up to 7 kJ mol^{-1} were observed for the ultramicroporous materials (pore diameter smaller than 7 \AA), between 5.4 kJ mol^{-1} and 3.5 kJ mol^{-1} for the supermicroporous (pore diameter: $7 - 20 \text{ \AA}$) and less than 3.6 kJ mol^{-1} for the mesoporous materials (pore diameter larger than 20 \AA).
- At 19.5 K the supermicro- and mesoporous materials showed hydrogen uptakes up to $1550 \text{ cm}^3 \text{ g}^{-1}$ (14 wt\%). From these adsorption isotherms BET specific surface

areas and pore volumes were determined for the first time by hydrogen adsorption isotherms in MOFs.

- The specific pore volume correlates almost linearly with the BET specific surface area with small deviation from the correlation for pure monolayer adsorption. Therefore, hydrogen in MOFs at 19.5 K mainly adsorbs in a monolayer as the pores are too small to enable multilayer adsorption. Additionally, this indicates that the specific surface area measured by hydrogen adsorption at 19.5 K is entirely provided by the inner surface area.
- A correlation of the hydrogen uptake at 77 K and 2 MPa to the specific surface areas from hydrogen adsorption yields that the density of adsorbed hydrogen at 77 K is higher than the density of hydrogen at the critical point but lower than for hydrogen at the boiling point.
- The specific surface areas of a material depend on the molecule used as probe. A comparison of the specific surface areas determined by nitrogen, argon and hydrogen adsorption with theoretical calculations shows that the BET theory, if applied carefully enables determination of the real surface area and that the difference between theory and experiment is a measure for the quality of the material. Furthermore the specific surface area available for hydrogen differs for some MOFs strongly from the surface area determined by nitrogen or argon adsorption.
- The hydrogen adsorption isotherms at 19.5 K show in a semilogarithmic plot a clear step-like behavior. These steps were assigned to the different adsorption sites for hydrogen in the framework using literature data from neutron scattering and theoretical calculations. The MOF was subsequently filled from the metal sites to the small and then the large pores. This is the first direct observation of adsorption sites for hydrogen from adsorption isotherms.
- Ultramicroporous materials show no hydrogen uptake at 20 K, whereas a significant hydrogen uptake is observed at 77 K. This gating effect can be assigned to kinetic hindrance of hydrogen below 60 K to enter the framework.
- Finally the requirements for MOFs as hydrogen storage material in a tank for mobile application were discussed. Therefore the total amount of gas present in the system and the volumetric storage density were calculated. The usable capacity was introduced, which is the amount of hydrogen that can be used in application if a certain back-pressure is needed for the empty tank. It was shown that an increase in temperature while discharging the tank significantly increases the usable capacity. For application in a tank the technical boundary conditions need to be regarded to determine the best MOF for this application which depends on the surface area, pore volume and pore size. Under the assumed conditions of loading at 77 K and 2 MPa, a minimum back pressure of 0.1 MPa, and a temperature increase of the tank of 40 K while unloading, with 75 mg g^{-1} MOF-177 has the highest usable capacity of all materials investigated.

The correlation of hydrogen storage properties to fundamental framework properties in this work enables synthesis of MOFs with tailored properties for hydrogen storage systems in mobile applications.

Appendix

Constants

For hydrogen *p* stands for parahydrogen, *o* for orthohydrogen, and *n* for (normal) hydrogen in the equilibrium composition at room temperature which is 25% parahydrogen and 75% orthohydrogen.

Avogadro constant	N_A	$6.023 \times 10^{23} \text{ mol}^{-1}$
Boiling temperature of hydrogen	$T_{boil \text{ } p-H_2}$	20.28 K [71]
	$T_{boil \text{ } n-H_2}$	20.38 K [71]
Boiling temperature of nitrogen	$T_{boil \text{ } N_2}$	77.35 K [71]
Cross-sectional area of hydrogen	$A_m \text{ } H_2$	$14.2 \times 10^{-20} \text{ m}^2$
Cross-sectional area of nitrogen	$A_m \text{ } N_2$	$16.2 \times 10^{-20} \text{ m}^2$
Density of liquid hydrogen (at 20 K at saturation)	$\rho_{n-H_{lq}}$	71.49 kg m^{-3}
		$28.20 \text{ cc mol}^{-1}$ [71]
	$\rho_{p-H_{lq}}$	$28.35 \text{ cc mol}^{-1}$ [71]
Density of liquid nitrogen (at 77.35 K and 1.013 bar)	ρ_{lqN}	$1.239 \text{ dm}^3 \text{ kg}^{-1}$ [71]
		$34.70 \text{ cc mol}^{-1}$ calculated from [71]
Gas constant	R	$8.314 \times 10^{-5} \text{ m}^3 \text{ bar K}^{-1} \text{ mol}^{-1}$
		$83.14 \text{ cc bar K}^{-1} \text{ mol}^{-1}$
Molecular weight of hydrogen	$m_M \text{ } H$	$2.016 \times 10^{-3} \text{ kg mol}^{-1}$
Molecular weight of nitrogen	$m_M \text{ } N$	$28.0134 \times 10^{-3} \text{ kg mol}^{-1}$
Standard Temperature	T_N	298 K
Standard Pressure	P_N	1 bar

Abbreviations

A_c	Cross-sectional area of one molecule
C	BET C constant, see section 2.1.3
k_H	Henry constant
m_{ads}	mass of the adsorbed layer
m_M	Molecular weight of the adsorptive
m_S	Mass of the sample
n	Amount of gas or liquid in mol
n_{ads}	Absolute amount adsorbed
n_{exc}	Excess amount adsorbed
n_{gas}	Amount of gas present due to the external pressure
n_{iC}	Gas content in the imaginary warm zone
n_{ini}	Initial gas content at the start of the experiment
n_{iW}	Gas content in the imaginary warm zone
n_m	Amount of gas contained in a monolayer
P	Pressure
p	Relative pressure, which is the pressure normalized to the pressure of liquefaction
P_{iC}	Pressure in the imaginary cold zone
P_{ini}	Initial pressure at the start of the experiment
P_{iW}	Pressure in the imaginary warm zone
ϱ_{lq}	Density of a liquid
s	Slope
SPV	Specific pore volume
SSA	Specific surface area
SSA_{BET}	Specific surface area calculated with the BET-model
SSA_{LM}	Specific surface area calculated with the Langmuir-model
T_C	Temperature in the cryostat at the sample site
T_R	Room temperature
V_{ads}	Volume of the adsorbed layer
V_{iC}	Imaginary cold volume
V_{iW}	Imaginary warm volume
V_{tot}	Total volume of the sample holder
Vol	Volume adsorbed (STP)
Vol_n	Volume adsorbed (STP) normalized to the sample mass
Z	Compression factor for correction of ideal gas law (see Eq. 4.1)

Compression factor Z for corrected ideal gas equation ($n = \frac{P \cdot V}{Z \cdot R \cdot T}$) [81]:

$$Z = (1.000547 - (6.07 \cdot 10^{-7}) \cdot T) + (0.000912 - (1.0653 \cdot 10^{-6}) \cdot T) \cdot P + ((7.373407 - 0.0901 \cdot T) \cdot 10^{-7}) \cdot P^2 \quad (4.1)$$

where P is given in atm (1 atm = 101.325 Pa = 1.013 25 bar).

Bibliography

- [1] K. Hirose, “Materials towards carbon-free, emission-free and oil-free mobility: hydrogen fuel-cell vehicles-now and in the future,” *Philosophical Transactions of the Royal Society A - Mathematical, Physical and Engineering Sciences*, vol. 368, no. 1923, pp. 3365–3377, 2010.
- [2] A. Züttel, A. Remhof, A. Borgschulte, and O. Friedrichs, “Hydrogen: the future energy carrier,” *Philosophical Transactions of the Royal Society A - Mathematical, Physical and Engineering Sciences*, vol. 368, no. 1923, pp. 3329–3342, 2010.
- [3] J. Yang, A. Sudik, C. Wolverton, and D. J. Siegel, “High capacity hydrogen storage materials: attributes for automotive applications and techniques for materials discovery,” *Chemical Society Reviews*, vol. 39, no. 2, pp. 656–675, 2010.
- [4] U. Eberle, M. Felderhoff, and F. Schüth, “Chemical and physical solutions for hydrogen storage,” *Angewandte Chemie International Edition*, no. DOI: 10.1002/anie.200806293, 2009.
- [5] A. Züttel, “Hydrogen storage methods,” *Naturwissenschaften*, vol. 91, no. 4, pp. 157–172, 2004.
- [6] I. Langmuir, “The adsorption of gases on plane surfaces of glass, mica and platinum,” *Journal of the American Chemical Society*, vol. 40, no. 9, pp. 1361–1403, 1918.
- [7] S. Brunauer, P. H. Emmett, and E. Teller, “Adsorption of gases in multimolecular layers,” *Journal of the American Chemical Society*, vol. 60, no. 2, pp. 309–319, 1938.
- [8] T. Düren, F. Millange, G. Férey, K. S. Walton, and R. Q. Snurr, “Calculating geometric surface areas as a characterization tool for metal-organic frameworks,” *Journal of Physical Chemistry C*, vol. 111, no. 42, pp. 15350–15356, 2007.
- [9] L. Gurvich *J. Phys. Chem. Soc. Russ.*, vol. 47, p. 805, 1915.
- [10] K. S. Sing, D. H. Everett, R. A. W. Haul, L. Moscou, R. A. Pierotti, J. Rouquerol, and T. Siemieniewska, “Reporting physisorption data for gas/solid systems with special reference to the determination of surface area and porosity,” *Pure and Applied Chemistry*, vol. 57, no. 4, pp. 603–619, 1985.
- [11] B. Schmitz, I. Krkljus, E. Leung, H. W. Höffken, U. Müller, and M. Hirscher, “A high heat of adsorption for hydrogen in magnesium formate,” *ChemSusChem*, vol. 3, no. 6, pp. 758–761, 2010.

- [12] S. Biswas, M. Grzywa, H. P. Nayek, S. Dehnen, I. Senkovska, S. Kaskel, and D. Volkmer, "A cubic coordination framework constructed from benzobistriazolate ligands and zinc ions having selective gas sorption properties," *Dalton Transactions*, no. 33, pp. 6487–6495, 2009.
- [13] D. Denysenko, M. Grzywa, M. Tonigold, B. Schmitz, I. Krkljus, M. Hirscher, E. Mugnaioli, U. Kolb, J. Hanss, and D. Volkmer, "Elucidating gating effects for hydrogen sorption in mfu-4 type triazolate-based mofs featuring different pore sizes," *Chemistry, a European Journal*, 2010.
- [14] H. Li, M. Eddaoudi, M. O’Keeffe, and O. M. Yaghi, "Design and synthesis of an exceptionally stable and highly porous metal-organic framework," *Nature*, vol. 402, no. 6759, pp. 276–279, 1999.
- [15] I. Senkovska, F. Hoffmann, M. Fröba, J. Getzschmann, W. Boehlmann, and S. Kaskel, "New highly porous aluminium based metal-organic frameworks: Al(OH)(ndc) (ndc=2,6-naphthalene dicarboxylate) and Al(OH)(bpdc) (bpdc=4,4’-biphenyl dicarboxylate)," *Microporous and Mesoporous Materials*, vol. 122, no. 1-3, pp. 93–98, 2009.
- [16] B. Schmitz, U. Müller, N. Trukhan, M. Schubert, G. Férey, and M. Hirscher, "Heat of adsorption for hydrogen in microporous high-surface-area materials," *ChemPhysChem*, vol. 9, no. 15, pp. 2181–2184, 2008.
- [17] U. Müller, H. Pütter, M. Hesse, H. Wessel, M. Schubert, J. Huff, and M. Guzmán, "Method for electrochemical production of a crystalline porous metal organic skeleton material." Patent WO/2005/049892, 2005. BASF Aktiengesellschaft.
- [18] H. K. Chae, D. Y. Siberio-Perez, J. Kim, Y. Go, M. Eddaoudi, A. J. Matzger, M. O’Keeffe, and O. M. Yaghi, "A route to high surface area, porosity and inclusion of large molecules in crystals," *Nature*, vol. 427, no. 6974, pp. 523–527, 2004.
- [19] G. Férey, C. Serre, C. Mellot-Draznieks, S. Surblé, J. Dutour, and I. Margiolaki, "A hybrid solid with giant pores prepared by a combination of targeted chemistry, simulation, and powder diffraction," *Angewandte Chemie - International Edition*, vol. 43, no. 46, pp. 6296–6301, 2004.
- [20] G. Férey, C. Mellot-Draznieks, C. Serre, F. Millange, J. Dutour, S. Surblé, and I. Margiolaki, "A chromium terephthalate-based solid with unusually large pore volumes and surface area," *Science*, vol. 309, no. 5743, pp. 2040–2042, 2005.
- [21] D. Dybtsev, C. Serre, B. Schmitz, B. Panella, M. Hirscher, M. Latroche, P. L. Llewellyn, S. Cordier, Y. Molard, M. Haouas, F. Taulelle, and G. Férey, "Influence of [Mo₆Br₈F₆]²⁻ cluster unit inclusion within the mesoporous solid mil-101 on hydrogen storage performance," *Langmuir*, vol. 26, no. 13, pp. 11283–11290, 2010.

- [22] C. Zlotea, P. Moretto, and T. Steriotis, "A round robin characterisation of the hydrogen sorption properties of a carbon based material," *International Journal of Hydrogen Energy*, vol. 34, no. 7, pp. 3044 – 3057, 2009.
- [23] B. Panella, M. Hirscher, H. Pütter, and U. Müller, "Hydrogen adsorption in metal-organic frameworks: Cu-mofs and zn-mofs compared," *Advanced Functional Materials*, vol. 16, no. 4, pp. 520–524, 2006.
- [24] A. G. Wong-Foy, A. J. Matzger, and O. M. Yaghi, "Exceptional h-2 saturation uptake in microporous metal-organic frameworks," *Journal of the American Chemical Society*, vol. 128, no. 11, pp. 3494–3495, 2006.
- [25] H. Frost, T. Düren, and R. Q. Snurr, "Effects of surface area, free volume, and heat of adsorption on hydrogen uptake in metal-organic frameworks," *Journal of Physical Chemistry B*, vol. 110, no. 19, pp. 9565–9570, 2006.
- [26] M. Dinca and J. R. Long, "Hydrogen storage in microporous metal-organic frameworks with exposed metal sites," *Angewandte Chemie International Edition*, vol. 47, no. 36, pp. 6766–6779, 2008.
- [27] P. Krawiec, M. Kramer, M. Sabo, R. Kunschke, H. Fröde, and S. Kaskel, "Improved hydrogen storage in the metal-organic framework $\text{Cu}_3(\text{btc})_2$," *Advanced Engineering Materials*, vol. 8, no. 4, pp. 293–296, 2006.
- [28] A. Vishnyakov, P. I. Ravikovitch, A. V. Neimark, M. Bulow, and Q. M. Wang, "Nanopore structure and sorption properties of cu-btc metal-organic framework," *Nano Letters*, vol. 3, no. 6, pp. 713–718, 2003.
- [29] D. Fairen Institute for Materials and Processes School of Engineering; the University of Edinburgh; UK. Unpublished results.
- [30] M. Schlichtenmayer, B. Streppel, and M. Hirscher, "Hydrogen physisorption in high ssa microporous materials - a comparison between ax-21 33 and mof-177 at cryogenic conditions," *International Journal of Hydrogen Energy*, 2010. In Press, Corrected Proof DOI: 10.1016/j.ijhydene.2010.09.057.
- [31] F. Rouquerol, J. Rouquerol, and K. Sing, *Adsorption by Powders and Porous Solids*. Academic Press, 1999.
- [32] G. Férey, M. Latroche, C. Serre, F. Millange, T. Loiseau, and A. Percheron-Guegan, "Hydrogen adsorption in the nanoporous metal-benzenedicarboxylate $\text{M}(\text{OH})(\text{O}_2\text{C}-\text{C}_6\text{H}_4-\text{CO}_2)$ ($\text{M} = \text{Al}^{3+}$, Cr^{3+}), MIL-53," *Chemical Communications*, no. 24, pp. 2976–2977, 2003.
- [33] T. Loiseau, L. Lecroq, C. Volkringer, J. Marrot, G. Férey, M. Haouas, F. Taulelle, S. Bourrelly, P. L. Llewellyn, and M. Latroche, "MIL-96, a porous aluminum trimesate 3D structure constructed from a hexagonal network of 18-membered rings and

- mu(3)-oxo-centered trinuclear units,” *Journal of the American Chemical Society*, vol. 128, no. 31, pp. 10223–10230, 2006.
- [34] M. Dinca and J. R. Long, “Strong h_2 binding and selective gas adsorption within the microporous coordination solid $\text{mg}_3(\text{o}_2\text{c-c}_1\text{0h}_6\text{-co}_2)_3$,” *Journal of the American Chemical Society*, vol. 127, no. 26, pp. 9376–9377, 2005.
- [35] J. A. Rood, B. C. Noll, and K. W. Henderson, “Synthesis, structural characterization, gas sorption and guest-exchange studies of the lightweight, porous metal-organic framework α - $[\text{mg}_3(\text{o}_2\text{ch})_6]$,” *Inorganic Chemistry*, vol. 45, no. 14, pp. 5521–5528, 2006.
- [36] A. U. Czaja, N. Trukhan, and U. Mueller, “Industrial applications of metal-organic frameworks,” *Chemical Society Reviews*, vol. 38, no. 5, pp. 1284–1293, 2009.
- [37] J. Rouquerol, P. Llewellyn, and F. Rouquerol, “Is the bet equation applicable to microporous adsorbents?,” in *Characterization of Porous Solids VII - Proceedings of the 7th International Symposium on the Characterization of Porous Solids (COPS-VII), Aix-en-Provence, France, 26-28 May 2005* (J. R. P.L. Llewellyn, F. Rodriguez-Reinoso and N. Seaton, eds.), vol. 160 of *Studies in Surface Science and Catalysis*, pp. 49 – 56, Elsevier, 2007.
- [38] K. S. Walton and R. Q. Snurr, “Applicability of the BET method for determining surface areas of microporous metal-organic frameworks,” *Journal of the American Chemical Society*, vol. 129, no. 27, pp. 8552–8556, 2007.
- [39] D. Denysenko Univeristy of Ulm. Unpublished results.
- [40] H. Furukawa, N. Ko, Y. B. Go, N. Aratani, S. B. Choi, E. Choi, A. O. Yazaydin, R. Snurr, M. O’Keeffe, J. Kim, and O. M. Yaghi, “Ultrahigh porosity in metal-organic frameworks,” *Science*, vol. 329, no. 5990, pp. 424–428, 2010.
- [41] K. M. L. Taylor-Pashow, J. D. Rocca, Z. Xie, S. Tran, and W. Lin, “Postsynthetic modifications of iron-carboxylate nanoscale metal-organic frameworks for imaging and drug delivery,” *Journal of the American Chemical Society*, vol. 131, no. 40, pp. 14261–14263, 2009.
- [42] E. Poirier and A. Dailly, “Thermodynamics of hydrogen adsorption in mof-177 at low temperatures: measurements and modelling,” *Nanotechnology*, vol. 20, no. 20, p. 204006, 2009.
- [43] H. Furukawa, M. A. Miller, and O. M. Yaghi, “Independent verification of the saturation hydrogen uptake in mof-177 and establishment of a benchmark for hydrogen adsorption in metal-organic frameworks,” *Journal of Materials Chemistry*, vol. 17, no. 30, pp. 3197–3204, 2007.

- [44] J. L. C. Rowsell, A. R. Millward, K. S. Park, and O. M. Yaghi, "Hydrogen sorption in functionalized metal-organic frameworks," *Journal of the American Chemical Society*, vol. 126, no. 18, pp. 5666–5667, 2004.
- [45] M. Schlichtenmayer Unpublished results.
- [46] B. Panella, K. Hönes, U. Müller, N. Trukhan, M. Schubert, H. Pütter, and M. Hirscher, "Desorption studies of hydrogen in metal-organic frameworks," *Angewandte Chemie, International Edition*, vol. 47, no. 11, pp. 2138–2142, 2008.
- [47] L. J. Murray, M. Dinca, and J. R. Long, "Hydrogen storage in metal-organic frameworks," *Chemical Society Reviews*, vol. 38, no. 5, pp. 1294–1314, 2009.
- [48] R. Chahine and T. K. Bose, "Low-pressure adsorption storage of hydrogen," *International Journal of Hydrogen Energy*, vol. 19, no. 2, pp. 161–164, 1994.
- [49] B. Panella, M. Hirscher, and S. Roth, "Hydrogen adsorption in different carbon nanostructures," *Carbon*, vol. 43, no. 10, pp. 2209–2214, 2005.
- [50] H. W. Langmi, D. Book, A. Walton, S. R. Johnson, M. M. Al-Mamouri, J. D. Speight, P. P. Edwards, I. R. Harris, and P. A. Anderson, "Hydrogen storage in ion-exchanged zeolites," *Journal of Alloys and Compounds*, vol. 404-406, pp. 637–642, 2005.
- [51] S. S. Kaye and J. R. Long, "The role of vacancies in the hydrogen storage properties of Prussian blue analogues," *Catalysis Today*, vol. 120, no. 3-4, pp. 311–316, 2007.
- [52] R. Chahine and T. K. Bose, "Characterization and optimization of adsorbents for hydrogen storage," in *Hydrogen Energy Progress XI*, pp. 1259–1263, 1996.
- [53] E. C. Spencer, J. A. K. Howard, G. J. McIntyre, J. L. C. Rowsell, and O. M. Yaghi, "Determination of the hydrogen absorption sites in $\text{Zn}_4\text{O}(1,4\text{-benzenedicarboxylate})$ by single crystal neutron diffraction," *Chemical Communications*, no. 3, pp. 278–280, 2006.
- [54] T. Yildirim and M. Hartman, "Direct observation of hydrogen adsorption sites and nanocage formation in metal-organic frameworks," *Physical Review Letters*, vol. 95, no. 21, pp. 215504/1–4, 2005.
- [55] S. Bordiga, J. G. Vitillo, G. Ricchiardi, L. Regli, A. Cocina, D. Zecchina, B. Arstad, M. Bjorgen, J. Hafizovic, and K. P. Lillerud, "Interaction of hydrogen with MOF-5," *Journal of Physical Chemistry B*, vol. 109, no. 39, pp. 18237–18242, 2005.
- [56] E. Klontzas, A. Mavrandonakis, G. E. Froudakis, Y. Carissan, and W. Kopper, "Molecular hydrogen interaction with irmo-1: A multiscale theoretical study," *Journal of Physical Chemistry C*, vol. 111, no. 36, pp. 13635–13640, 2007.

- [57] K. Sillar, A. Hofmann, and J. Sauer, “Ab initio study of hydrogen adsorption in MOF-5,” *Journal of the American Chemical Society*, vol. 131, pp. 4143–4150, MAR 25 2009.
- [58] V. K. Peterson, Y. Liu, C. M. Brown, and C. J. Kepert, “Neutron powder diffraction study of d-2 sorption in cu-3(1,3,5-benzenetricarboxylate)(2),” *Journal of the American Chemical Society*, vol. 128, no. 49, pp. 15578–15579, 2006.
- [59] M. R. Hartman, V. Peterson, and Y. Liu, “Neutron diffraction and neutron vibrational spectroscopy studies of hydrogen adsorption in the prussian blue analogue $\text{Cu}_3[\text{Co}(\text{CN})_6]_2$,” *Chemistry Materials*, vol. 18, no. 14, pp. 3221–3224, 2006.
- [60] M. Dinca, W. S. Han, Y. Liu, A. Dailly, C. M. Brown, and J. R. Long, “Observation of Cu^{2+} - H_2 interactions in a fully desolvated sodalite-type metal-organic framework,” *Angewandte Chemie-International Edition*, vol. 46, no. 9, pp. 1419–1422, 2007.
- [61] M. Dinca, A. Dailly, Y. Liu, C. M. Brown, D. A. Neumann, and J. R. Long, “Hydrogen storage in a microporous metal-organic framework with exposed Mn^{2+} coordination sites,” *Journal of the American Chemical Society*, vol. 128, no. 51, pp. 16876–16883, 2006.
- [62] P. Forster, J. Eckert, B. D. Heiken, J. B. Parise, J. W. Yoon, S. H. Jhung, J.-S. Chang, and A. K. Cheetham, “Adsorption of molecular hydrogen on coordinatively unsaturated $\text{Ni}(\text{II})$ sites in a nanoporous hybrid material,” *Journal of the American Chemical Society*, vol. 128, no. 51, pp. 16846–16850, 2006.
- [63] P. D. C. Dietzel, P. A. Georgiev, J. Eckert, R. Blom, T. Straessle, and T. Unruh, “Interaction of hydrogen with accessible metal sites in the metal-organic frameworks M-2(dhtp) (CPO-27-M; M = Ni, Co, Mg),” *Chemical Communications*, vol. 46, no. 27, pp. 4962–4964, 2010.
- [64] J. L. C. Rowsell and O. M. Yaghi, “Effects of functionalization, catenation, and variation of the metal oxide and organic linking units on the low-pressure hydrogen adsorption properties of metal-organic frameworks,” *Journal of the American Chemical Society*, vol. 128, pp. 1304–1315, 2006.
- [65] Y. Liu, H. Kabbour, C. M. Brown, D. A. Neumann, and C. C. Ahn, “Increasing the density of adsorbed hydrogen with coordinatively unsaturated metal centers in metal-organic frameworks,” *Langmuir*, vol. 24, no. 9, pp. 4772–4777, 2008.
- [66] J. G. Vitillo, L. Regli, S. Chavan, G. Ricchiardi, G. Spoto, P. D. C. Dietzel, S. Bordiga, and A. Zecchina, “Role of exposed metal sites in hydrogen storage in MOFs,” *Journal of the American Chemical Society*, vol. 130, no. 26, pp. 8386–8396, 2008.
- [67] H. Frost and R. Q. Snurr, “Design requirements for metal-organic frameworks as hydrogen storage materials,” *Journal of Physical Chemistry C*, vol. 111, no. 50, pp. 18794–18803, 2007.

- [68] A. Kuc, T. Heine, G. Seifert, and H. A. Duarte, "On the nature of the interaction between h-2 and metal-organic frameworks," *Theoretical Chemistry Accounts*, vol. 120, no. 4-6, pp. 543–550, 2008.
- [69] A. Kuc, T. Heine, G. Seifert, and H. A. Duarte, "H₂ adsorption in metal-organic frameworks: Dispersion or electrostatic interaction?," *Chemistry A European Journal*, vol. 14, no. 22, pp. 6597–6600, 2008.
- [70] G. Ricchiardi, J. G. Vitillo, D. Cocina, E. N. Gribov, and A. Zecchina, "Direct observation and modelling of ordered hydrogen adsorption and catalyzed ortho-para conversion on ets-10 titanosilicate material.," *Physical Chemistry Chemical Physics*, vol. 9, no. 21, pp. 2753–2760, 2007.
- [71] N. B. Vargaftik, Y. K. Vinogradov, and V. S. Yargin, *Handbook of Physical Properties of Liquids and Gases - Pure Substances and Mixtures*. begell house, inc., 1996.
- [72] S. S. Kaye, A. Dailly, O. M. Yaghi, and J. R. Long, "Impact of preparation and handling on the hydrogen storage properties of Zn₄O(1,4-benzenedicarboxylate)₃ (mof-5)," *Journal of the American Chemical Society*, vol. 129, no. 46, pp. 14176–14177, 2007.
- [73] T. Düren, Y.-S. Bae, and R. Q. Snurr, "Using molecular simulation to characterise metal-organic frameworks for adsorption applications," *Chemical Society Reviews*, vol. 38, pp. 1237–1247, 2009.
- [74] F. M. Mulder, T. J. Dingemans, M. Wagemaker, and G. J. Kearley, "Modelling of hydrogen adsorption in the metal organic framework mof-5," *Chemical Physics*, vol. 317, pp. 113–118, 2005.
- [75] V. K. Peterson, Y. Liu, C. M. Brown, and C. J. Kepert, "Structural characterization of D-2 in Cu-3(1,3,5-benzenetricarboxylate)(2) using neutron powder diffraction," in *PRICM 6: Sixth Pacific RIM International Conference on Advanced Materials and Processing, pts 1-3* (Chang, YW and Kim, NJ and Lee, CS, ed.), vol. 561-565 of *Materials Science Forum*, pp. 1601–1604, 2007. 6th Pacific Rim International Conference on Advanced Materials and Processing, Cheju Isl, SOUTH KOREA, NOV 05-09, 2007.
- [76] J. Rowsell, J. Eckert, and O. Yaghi, "Characterization of h-2 binding sites in prototypical metal-organic frameworks by inelastic neutron scattering," *Journal of the American Chemical Society*, vol. 127, no. 42, pp. 14904–14910, 2005.
- [77] Y. F. Chen, R. Babarao, S. I. Sandler, and J. W. Jiang, "Metal-organic framework mil-101 for adsorption and effect of terminal water molecules: From quantum mechanics to molecular simulation," *Langmuir*, vol. 26, no. 11, pp. 8743–8750, 2010.

- [78] H. Kim, S. D. G., M. Yoon, J. W. Yoon, Y. K. Hwang, J.-S. Chang, and K. Kim, "Temperature-triggered gate opening for gas adsorption in microporous manganese formate," *ChemComm*, pp. 4697–4699, 2008.
- [79] J.-B. Lin, J.-P. Zhang, W.-X. Zhang, W. Xue, D.-X. Xue, and X.-M. Chen, "Porous Manganese(II) 3-(2-Pyridyl)-5-(4-Pyridyl)-1,2,4-Triazolate Frameworks: Rational Self-Assembly, Supramolecular Isomerism, Solid-State Transformation, and Sorption Properties," *Inorganic Chemistry*, vol. 48, no. 14, pp. 6652–6660, 2009.
- [80] J. S. Lee and S. H. Jhung, "Vapor-phase adsorption of alkylaromatics on aluminum-trimesate MIL-96: An unusual increase of adsorption capacity with temperature," *MICROPOROUS AND MESOPOROUS MATERIALS*, vol. 129, no. 1-2, pp. 274–277, 2010.
- [81] Y. Ye, "Interaction of hydrogen with novel carbon materials." PhD thesis.

Danksagung

Zum Schluss möchte ich allen danken die diese Arbeit ermöglicht und unterstützt haben:

Insbesondere möchte ich Dr. Michael Hirscher für die intensive Betreuung danken. Er hat mir in den letzten Jahren viel ermöglicht und ich konnte dabei viele wertvolle Erfahrungen sammeln.

Frau Prof. G. Schütz möchte ich danken, dass sie mir ermöglicht hat diese Arbeit in ihrer Abteilung anzufertigen und den Hauptbericht übernommen hat.

Herrn Prof. J. Wrachtrup und Herrn Prof. E. Roduner danke ich für die Übernahme des Mitberichts.

Bei der Tieftemperatur-Abteilung bedanke ich mich sehr für die Hilfe bei der Planung und dem Bau des Kryostaten für die 20 K Messungen.

Frau A. Fuchs danke ich sehr für die unermüdliche Messung der Stickstoffadsorption verschiedenster MOFs.

Ulrike Eigenthaler danke ich für die schönen REM Bilder.

Herzlich bedanken möchte ich mich auch bei den Gruppen, die die MOFs synthetisiert haben: den Gruppen von Dr. U. Müller (BASF SE), Prof. G. Férey (Université de Versailles, France), Prof. S. Kaskel (TU Dresden) und Prof. D. Volkmer (Universität Ulm und Augsburg).

Bedanken möchte ich mich auch bei allen Kollegen, die meine Arbeit unterstützt haben. Vor allem bei Maurice Schlichtenmayer für seinen rheinischen Frohsinn.

Ganz herzlich bedanken möchte ich mich auch bei Herrn Dr. W. Philipp, der den Stein ins Rollen brachte und Lena und Birte die dafür sorgten dass er nicht zwischendurch liegen blieb.

Und schließlich bedanke ich mich ganz herzlich bei meiner Familie und meinem Mann Olli, die mit viel Liebe und Verständnis mich immer wieder motiviert und unterstützt haben.